QUANTUM DECOHERENCE BY CHAOTIC ENVIRONMENTS: THEORY AND APPLICATIONS

by

Murat Çetinbaş

M.Sc., Yıldız Technical University, 2001

B.Sc., Yıldız Technical University, 1999

A THESIS SUBMITTED IN PARTIAL FULFILLMENT

OF THE REQUIREMENTS FOR THE DEGREE OF

DOCTOR OF PHILOSOPHY

in the Department

of

Chemistry

SIMON FRASER UNIVERSITY

Spring 2009

APPROVAL

Name: Murat Cetinbas

Degree: Doctor of Philosophy

Title of Thesis: Quantum Decoherence by Chaotic Environments: Theory and Applications

Examining Committee:

Chair — Dr. Zuo-Guang Ye
Associate Professor, Department of Chemistry

Dr. Gary W. Leach
Senior Supervisor
Professor, Department of Chemistry

Dr. Paul W. Percival
Supervisor
Professor, Department of Chemistry

Dr. George Kirczenow
Supervisor
Professor, Physics Department

Dr. Michael H. Eikerling
Internal Examiner
Assistant Professor, Department of Chemistry

Dr. Moshe Shapiro
External Examiner
Professor, Department of Chemistry
University of British Columbia

Date Defended/Approved: January 15, 2009

Abstract

Condensed and solid phase environments offer a wide range of controllable interactions for new quantum technologies. Understanding the dynamics of open quantum systems interacting with such complex environments is important for correct modeling of many chemical and physical phenomena and for development of new quantum technologies. The central theme of this thesis is the open system dynamics of a small quantum system coupled to self-interacting chaotic environments.

This thesis consists of three related parts. In the first part, a theory predicting open dynamics of a quantum system interacting with chaotic environments is reported. The theory is of a Kraus decomposition form, which is exact for chaotic environments of thermodynamic dimension. Extension of the theory to time-dependent system Hamiltonians is also presented so that it may have practical applications for studies of new quantum technologies. In the second part, extensive numerical calculations are performed to obtain the exact quantum dynamics for two realistic models of self-interacting environments. Both models represent a statistically flawed isolated quantum computer (QC) core. In the first model, the open dynamics of a quantum-control NOT (CNOT) gate in the presence of static internal imperfections are investigated and internal error sources are identified for a large number of QC configurations. The results indicate that the strong two-body imperfections suppress the internal decoherence and enhance the performance of the CNOT gate. Moreover, the largest source of error is found to be unitary due to coherent shifting rather than

decoherence. The second model represents a single-qubit detector set-up designed to probe the internal bath dynamics. Small low temperature isolated QCs with static internal flaws can be considered as prototypical examples of self-interacting – and possibly chaotic – environments of two level systems for which the exact quantum dynamics can be numerically tractable on a classical computer. In the third part, the theory of chaotic environments is tested against the exact numerical results of the above models and very good agreements are obtained.

To my father

Acknowledgments

I would like to thank the Department of Chemistry, the Dean of Graduate Studies and Dr. Joshua Wilkie for financial support provided throughout my doctoral study. I gratefully acknowledge the high performance computing resources provided by WestGrid and the Simon Fraser University Bugaboo cluster.

I would like to express my gratitude to several individuals for their intellectual support: Dr. Gary Leach, my senior supervisor, for his encouragement, critical insights, and his excellent mentorship; Dr. George Kirichenov and Dr. Paul Percival, my supervisors, for their criticisms and advice; Dr. Joshua Wilkie for his collaboration in a number of projects and for carefully reading several manuscripts; Dr. Michael Eikerling and Dr. Moshe Shapiro for their valuable suggestions and fruitful comments.

I would like to thank friends and colleagues in the Department of Chemistry for their encouragement and support and Dr. Claire McCague for proofreading the thesis. Special thanks go to Dr. Oktay Sinanoğlu whose passion for science has been an ongoing source of desire for me to continue my studies. I would also like to thank Dr. Martin Siegert for his technical support on WestGrid and the Simon Fraser University Bugaboo cluster.

Last but not least, I would like to extend my special thanks to my wife and daughter for their patience and support, and to my parents for their unlimited encouragement.

Contents

List of Tables

List of Figures

Chapter 1

Introduction

The dynamics of a closed quantum system evolves from the Schrödinger equation [1]. The interaction of a quantum system with its surrounding environment, however, induces quantum processes for which the Schrödinger's dynamics no longer holds. This is usually described by stating that the system is not closed and undergoes open system dynamics [2, 3]. In general, open system dynamics consists of decoherence, dissipation, and coherent shift processes. Decoherence is a process in which the quantum correlations (i.e. coherent superposition) of the state of the system are destroyed due to interactions with its environment. Dissipation is a means of energy transfer process from the system to its environment. The effects of decoherence and dissipation on the system are not unitary, and thus irreversible in practice. On the other hand, the coherent shift process is a unitary contribution of an environment on the open system dynamics, which perturbs the free system Hamiltonian (i.e. the Hamiltonian of the closed quantum system) with a Hermitian perturbation. Consequently, the system evolves under an effective system Hamiltonian, which comprises a free system Hamiltonian plus a perturbation. Unraveling the effects induced by the different components of system-environment interactions, and thus determining the degree of deviation from the Schrödinger dynamics is of particular importance to the understanding

of many chemical and physical phenomena and in the development of new quantum technologies such as molecular motors and electronics [4], laser control scenarios for chemical reactions [5], and quantum computing [6-8]

Traditional theories of open system dynamics represent an environment's degree of freedom either phenomenologically [9] or as a collection of non-interacting oscillators [10, 11] or spins [12]. These non-interacting environment models are only valid in special instances. For example, in modeling atom-radiation interactions, the vacuum radiation field is represented by uncoupled oscillators. However, the validity of non-interacting environment models is questionable in general. This is because the non-interacting environment models do not take into account the internal dynamics of an environment, which may play an important role in a decoherence process and thus may strongly influence the open system dynamics. Consider as an example the quantum control [5, 13] of a chemical reaction in a large molecule which requires coherent manipulation of the reaction coordinate (i.e. the subsystem) while simultaneously interacting with the rest of the molecule(s) (i.e. the microscopic environment) as well as with the hosting media e.g. gas phases, solutions, surfaces, or solids (i.e. the macroscopic environment). Molecules are strongly self-interacting anharmonic microscopic environments and hence are not well represented by independent harmonic oscillators or spins. Likewise, the hosting media are strongly self-interacting and anharmonic in general. Thus, the coherent quantum control in condensed phase media, by and large, consists of a coherently manipulated quantum subsystem coupled to strongly self-interacting and possibly chaotic environments. These considerations suggest that more general approaches beyond the standard scenarios of decoherence are warranted for correct modeling of open system dynamics in condensed phase environments. This can be accomplished by general environment models in which self-interactions among environmental modes are fully included and therefore such environment models are more appropriate to represent complex environments with non-trivial internal dynamics.

The work reported in this thesis is devoted to the understanding of the open dynamics of a small quantum system coupled to self-interacting chaotic environments. This work consists of three related parts. The first part is concerned with development of a theory of open system dynamics induced by chaotic environments [14]. The theory is of an explicit Kraus decomposition form, which becomes exact for chaotic environments of thermodynamic dimension (i.e. very large). Generalization of the theory to time-dependent system Hamiltonians has also been achieved [15] and thus the theory may have important applications for studies of new quantum technologies [4-8]. In the second part, extensive numerical calculations are performed to obtain exact quantum dynamics for two models of self-interacting chaotic environments [16-18]. Both models represent a statistically flawed isolated quantum computer (QC) core. In the first model, the open dynamics of a quantum-controlled NOT (CNOT) gate is investigated and internal error sources are identified [16, 17]. The second model represents a single qubit detector set-up designed to probe the internal environmental dynamics [18]. Small low temperature isolated QCs with static internal flaws can be considered as prototypical examples of self-interacting and possibly chaotic – environments of two level systems for which exact quantum dynamics can be numerically tractable on a classical computer. Therefore, the exact numerical results obtained in these studies serve as benchmarks, against which the developed theories of self-interacting environments can be tested. Hence, in the third part, the theory [14, 15] developed in the first part is tested against the exact benchmark results [16-18] and very good agreement is obtained.

The remainder of this chapter is comprised of three sections, each of which is an introduction to different parts of this thesis.

1.1 Theories of self-interacting environments

Many chemical and physical phenomena occur in complex environments, e.g. condensed and solid state media, which involve an enormously large number of participating components.

While the Schrödinger equation for pure quantum states and the Liouville–von Neumann equation for pure and non-pure quantum states provide the formally exact dynamics of closed quantum systems, in practice, the exact quantum dynamics of such large quantum systems are not computationally tractable. Fortunately, important dynamical changes nsually occur only in a small part of such large systems. For example, a reaction coordinate in a large molecule is the potentially interesting and the most important part of the molecule. Therefore, a subsystem-environment scheme is employed as a starting point to formulate the open dynamics of a small quantum system. In subsystem-environment schemes, the subsystem or simply *the system* thus represents the important part of a larger system and the rest of the whole can be treated or approximated as a reservoir (i.e. heat bath). Typical examples of this approach include electron [19] and proton [20] transfer reactions in large biological molecules, vibrational relaxation of ions in solution [21], proton transfer in organic molecules in solids [20], and migration of defects in solid state media [22].

There has been growing interest recently in the development of new quantum technologies [4-8]. Principles behind the new quantum technologies rely on the existence of special quantum correlations, such as superpositions of states or entangled states. Moreover, it is required that these quantum states can be coherently manipulated by externally induced unitary operations, e.g. manipulations by a laser. Unfortunately, the quantum states are fragile and their maintenance is hard to achieve even at very low temperatures. Deviations from Schrödinger dynamics are inevitable in practice and thus considered as error sources during implementation. In this respect, the destructive effects induced by system-environment interactions constitute a potentially serious problem for the new quantum technologies. The condensed and solid phase environments provide an attractive range of controllable interactions for the quantum technologies. The coherent quantum control of a quantum system in such complex environments requires detailed knowledge of all factors that affect the open system dynamics. However, the factors which encumber or ease the

coherent quantum control in complex environments are not very well known. This is partly due to the fact that the internal environmental dynamics is neglected by traditional theories of decoherence.

Chaotic dynamics [23, 24] is an unavoidable feature of complex environments. Recent experimental [25] and numerical [26] evidence suggests that the condensed phase dynamics is generally chaotic. For example, the dynamics of a colloidal particle in water [25] and vibrational dynamics of a silicon crystal [26, 27] have been shown to be chaotic. Anharmonic corrections are known to be important in the study of phonons and essential for an understanding of heat transport phenomena [28]. Chaotic and regular (i.e. integrable) systems have qualitatively different dynamics and therefore chaotic systems cannot be accurately described by regular systems. Thus, the self-interacting and chaotic environment models provide a better representation of condensed or solid state environments than standard uncoupled oscillator bath models. Moreover, recent evidence shows that the self-interacting environment models [29, 30] can cause much less decoherence than would be predicted by uncoupled bath models. Semiclassical [31, 32] and other [33, 34] arguments have been used to explain this effect. However, the reverse effect has also been reported in numerical simulations at high temperatures [35, 36] and for an environment consisting of a few chaotic degrees of freedom [37, 38]. These considerations strongly suggest that the internal dynamics of an environment is an important factor that should be taken into account in the formulation of open system dynamics.

Theories implicitly allowing the self-interactions among environmental modes have been reported. However, these theories have some disadvantages. For instance, the correlation functions appearing in Redfield theory [39, 40] and its generalizations [41, 42] are often calculated via realistic molecular dynamics simulations where environmental self-interactions can fully be taken into account. However, the Redfield theory is known to possess a few

drawbacks. The Redfield master equation violates the positivity of the reduced density operator. The use of special initial conditions in some cases is shown to prevent the positivity violation [40]. Furthermore, the Redfield master equation predicts an incorrect long time limit [43]. The theory developed by Bulgac *et al* [44] also takes into account the environmental self-interactions, representing the environment as an ensemble of random matrices. However, the master equation of Bulgac *et al* [44] seems only suitable for high temperatures and the random matrix representation of an environment may not be appropriate to explore certain effects intrinsic to a specific environment. Exact solutions for a harmonic oscillator coupled to a general environment model are reported as well [45]. The semi-classical Wigner method predicts quite accurate results [46] at moderately high temperatures. The recently developed mean-field master equation [47-51] is also a promising computational tool for self-interacting environments. The theory reported in this thesis is free of the limitations of the theories summarized above and especially applicable at low temperature limits where new quantum technologies are expected to operate.

There are two commonly used starting points for derivation of a theory of open system dynamics: the Nakajima and Zwanzig Projection Operator technique [52] and the Kraus Operator Sum Representation (OSR) technique [53]. Both techniques lead to formally exact theories for open system dynamics. However, the resulting exact theories are of formal interest only because they do not allow either numerical solutions or explicit forms of dynamical equations to be determined. In this thesis, the Kraus OSR techuique is used to obtain a dynamical equation of motion for a quantum subsystem interacting with a large chaotic environment. The Kraus OSR automatically satisfies all the required conservation laws for the reduced density, i.e. Hermiticity, positivity and norm conservation. The explicit form of Kraus operators for general system-bath models, however, is impossible to obtain in practice. This is partly because the Kraus OSR is not a unique representation like spectral decomposition. Nevertheless, the Kraus OSR provides a good starting point for the

derivation of approximate master equations as well as evolution equations for open system dynamics, see e.g. [54]. In recent investigations [14, 15] it has been shown that a unique form of Kraus decomposition and an explicit form of Kraus operators can easily be obtained for large chaotic environments. In chapter 2 of this thesis, a detailed derivation of the chaotic Kraus decomposition (CKD) is presented.

1.2 Internal errors in flawed quantum computers

Computers process information by by manipulating strings of binary numbers. The memory of a classical computer is made up of bits. A classical bit is a physical system, nothing bnt a switch, with two possible states, i.e. 0 or 1. At a particular instance in time, the switch can be either on or off. A quantum bit is called a qubit. A qubit is a two-level quantum system; such as a spin-half particle or gronnd and excited state of an atom. In addition to two classical–like states, i.e. $\{|0\rangle, |1\rangle\}$, qubits have quantnm states, i.e. $|\psi\rangle = a|0\rangle + b|1\rangle$ with complex a and b such that $|a|^2 + |b|^2 = 1$. If a qubit is considered as a quantum switch, the state of this switch can be on and off in the same time.

A two-bit register, i.e. two switches, can store 1 of 4 different binary numbers, i.e. 00, 01,10 or 11 in its memory. A classical logic operation transforms one of these numbers to another. A two–qubit register, on the other hand, can store 4 different numbers in the same time as a superposition state, $|\psi\rangle = a|00\rangle + b|01\rangle + c|10\rangle + d|11\rangle$ with $a^2 + b^2 + c^2 + d^2 = 1$. Hence, a quantum logic operation on $|\psi\rangle$ is then equivalent to 4 classical–like operations. An N qubit register then can store 2^N numbers and can perform 2^N operations simultaneously. Hence, quantnm computers provide extremely large number of states for computation.

Quantum computation can be achieved by using only one– and two–qubit quantum gates. The quantum gates are elementary quantum logic operations which transform an input qubit state to an output qubit state. A one–qubit gate is an operation performed on a state of a single qubit. Similarly, a two–qubit gate is an operation performed on a state

of two qubits. It has been shown that universal quantum computation can be achieved by one and two–qubit gates [55-57]. This means that any quantum algorithm, whether it is simple or very complex, can be composed as a combination of one and two-qubit gates.

Quantum computation promises superior computing power over classical computation: Shor's algorithm [58] can factorize large numbers into primes exponentially faster than any classical algorithm. Grover's search [59] algorithm can identify an object from a randomly ordered database with a square root increase in speed as compared to its classical analog. Quantum cryptography [60] guarantees secure communication and quantum Fourier transform promises faster quantum chemistry calculations [61]. This great potential for computational power has motivated numerous experimental proposals. Particular experiments with linear ion traps [62] and nuclear spins in solutions [63] have already demonstrated that quantum computation is indeed achievable for few qubit systems. However, it seems that these particular architectures are limited to a small number of qubits, and not easily scalable for larger qubit sizes. However, hundreds of qubits are needed for a quantum computer to compete with its classical analog [64]. In this respect, solid state QCs are becoming the center of attention with their scalable architectures. Proposals for scalable quantum computers include nuclear spins embedded in a solid [65], Fullerene–electron–spin quantum computer [66], electrons in quantum dots [67], Josephson-junction devices [68] based on charge [69, 70] and flux [71] degrees of freedom.

External errors emerging from interactions of a QC with its external surrounding environment are widely believed to be the primary limiting factor in the development of quantum computing technologies [6-8]. However, recent investigations [16-18] show that even when a QC core is completely isolated from its surrounding external environment, the coherent dynamics of qubits within an isolated QC core are not guaranteed. This is because qubits within such an isolated QC are still subject to the destructive effects of internal decoherence, dissipation and coherent shifting caused by possible one– and two–body residual interactions

and imperfections among the qubits.

The issue of internal errors attracted attention recently in the context of quantum chaos. Investigations [72, 73] based on statistical properties of an eigenspectrum of an isolated QC with static internal imperfections show that quantum chaos and a consequent thermalization [74] of the QC core is inevitable in the presence of sufficiently strong residual two–qubit interactions. Ideal computational states of a QC are separable. Quantum chaos destroys these states as a result of incoherent mixing [75]. The mixing process is expected to worsen over time, leading to an effective thermalization of the QC. On the other hand, the dynamical studies [76-78] where the internal imperfections are treated as random perturbations show that chaotic perturbations actually stabilize the QC dynamics [76-78]. These seemingly contradictory conclusions, i.e. destruction and stabilization of QCs with quantum chaos, suggest that establishing the effects of internal imperfections is a complex problem.

Internal errors arising in a QC core may originate from internal decoherence, dissipation and even coherent shifting. The studies presented here and reported in [16-18] show that the relative importance of these effects and their dependence on residual internal couplings can only be determined via fully realistic dynamical simulations of QC operations. The objective of these studies [16-18] was to examine directly the operation of a flawed QC in a specific architecture, to investigate the different types of internal errors that emerge, and to observe how these errors change with varying magnitudes of static internal imperfections between qubits.

In chapters 3–5 of this thesis, detailed discussions of these three studies [16-18] are presented. Specifically, in chapters 3–4, the effects of one– and two–body static flaws in a CNOT gate [69] performed on two qubits of a larger Josephson charge-qubit QC [68] are explored. These two chapters comprise detailed discussions of the results reported in [16, 17]. In chapter 5, a single-qubit subsystem is designed to show how the internal dynamics of an environment can be probed via the observation of environment–induced Rabi oscillations in

the subsystem dynamics. Chapter 5 is based on the Rabi detector study reported in [18].

In chapter 3, a statistically flawed many–qubit isolated QC core is envisaged. A CNOT gate operates on two qubits of the QC. The two qubits performing the CNOT gate interact with neighboring qubits of the QC via residual interactions. As a result, internal errors are generated in the gate. The isolated QC core in this instance is mapped onto a subsystem-environment scheme wherein the active part of the QC, a two-qubit register (the subsystem), performs the CNOT gate while interacting with the neighboring idle qubits (the environment).

The exact dynamics of the QC are obtained for a variety of configurations: eight different initial register states, two different error generators (phase and bit-flip errors) and five different intra-environmental interaction strengths, and the errors are identified by use of two error quantifiers: purity and fidelity. These error measures are used throughout to estimate the quality of computation. In particular, these measures are used to distinguish non-unitary errors (i.e. decoherence and dissipation) from those of the unitary type (i.e. coherent shifting or distortions).

In chapter 4, simulation results are reported. First, the results are presented for average error quantifiers, i.e. average purity and fidelity. These averages were calculated over standard basis states and Bell states, which allowed the compression of the data and the estimation of the overall relative performance of standard basis states versus Bell states for two different types of error generators. Second, the results are reported for individual initial states to determine possible state dependency of errors. A brief summary of the results presented follows. In all cases, it was found that the gate purity reflects a non-negligible amount of decoherence for both bit-flip and phase type non-unitary errors. However, the magnitude of errors detected by the gate fidelity is found to be very large as compared to those detected by gate purity. This unexpected large difference arises from large unitary errors due to the coherent shift process. When the QC is driven into the chaotic regime by

increasing the magnitude of two-body interactions, the non-unitary errors are suppressed to a negligible extent. However, the large unitary errors survive even in the chaotic regime and endanger the quality of computation.

Two important consequences can be deduced from the above results. First, environment-induced coherent shifts can be a serious source of unitary errors for QCs in the presence of static internal imperfections. Second, decoherence recuperating chaotic intra-environmental interactions can be used in correction of non-unitary errors. The results also suggest that environment-induced unitary errors can be a more serious obstacle for QC operations than non-unitary errors. This observation has not been reported previously. Fortunately, since these errors are of unitary type, they may easily be corrected with existing [79] or more specifically designed error correction schemes. Moreover, since the chaotic interactions are very successful in suppression of non-unitary errors, one can in principle manipulate an ideal qubit environment to enhance the performance of active qubits. Hence, deliberately induced chaotic interactions can serve as an error correcting strategy when implementation of such strong qubit-qubit interactions is practical.

In CNOT studies [16, 17], the coherent shift process was identified as a potentially harmful error source for QCs with static internal imperfections. However, in chapter 5, it is shown that the coherent shift could be put to good use. Specifically, it is shown that the coherent shift can be used to probe internal dynamics of an environment and to estimate the two-body intra-environmental interaction strength.

One– and two–qubit gates suffice to perform any quantum algorithm. The gate operations can be accomplished by manipulations of one and two-qubit control parameters. One qubit imperfections may arise due to the variation of one-body control parameters while two-qubit imperfections may emerge as a result of the residual qubit-qubit interactions or interactions of qubits with local impurities. The error induced by one-body imperfections

should readily be correctable as compared to the errors originating from two-body interactions. Information on the strength of two-body interactions may prove very useful in the elimination of their effects. Results reported in [16, 17] and in chapter 4 indicate that the errors induced by coherent shifts are very sensitive to the magnitude of environmental self-interactions. This effect can be nsed to devise a detector setup to acquire useful information about environmental self-interactions.

In chaptcr 5, a single-qubit detector is devised and allowed to interact with the rest of a QC. In this setup, the system degree of freedom consists of a single two-level system and the environment degree of freedom includes a number of two-level systems interacting with each other. In the absence of system-environment interactions, the detector qubit undergoes a phase evolntion only. Once the system-environment interactions are in effect, the populations of the detector display Rabi oscillations due to the coherent shift. The fidelity of the detector qubit also shows a periodic behavior in accord with the Rabi oscillations. It is shown that the strength of the environmental self-interaction can be determined from the period of these oscillations. The basic ideas behind this detector setup should also be applicable in more general contexts. For example, an optical impurity in a solid may serve as a detector to extract knowledge of self-interactions in solids.

1.3 Testing chaotic Kraus decomposition

Isolated QCs with static internal flaws are prototypical examples of self-iuteracting chaotic environments of two level systems that allow exact numerical solution for the relatively low dimension of qubit environments. The exact numerical results obtained in such studies can serve as benchmarks against which theories for chaotic environments can be tested. Hence, in the third part of this thesis the CKD is tested against exact numerical results of the QC models.

In chapter 6, the results of the test calculations are presented for a chaotic regime where

the CKD applies. Specifically, the exact numerical results obtained for the Rabi detector study are used to test the time-independent form of the CKD aud the exact results of the CNOT study are used to test the time-dependent form of the CKD. The accuracy of the CKD is estimated by making use of two error quantifiers, i.e. purity and fidelity. Purity is used to estimate the accuracy of the CKD in the case of non-unitary effects, i.e. decoherence and dissipation, and fidelity is used to estimate the accuracy in the case of unitary effects, i.e. coherent shifting. While the purity and fidelity suffice for an accurate assessment of open system dynamics, these error measures do not provide useful information on which matrix elements of a density operator are affected most in the course of open system dynamics. This knowledge may prove very useful, especially in optimization of a quantum algorithm in the presence of coherent shifting. Therefore, the exact numerical results obtained for matrix elements of reduced density are also compared with those obtained with the CKD to judge whether the CKD is successful in predicting the dynamics of the matrix elements.

One particular assumption used in the derivation of the CKD is that the dimension of the chaotic environment is very large. The CKD becomes exact only when the number of environment modes approaches infinity. However, the exact numerical results used to test the CKD are limited to an environment of ten two-level systems. Therefore, the prediction of the CKD for such a small environment is only approximate. However, qualitatively good agreement was obtained and the results for all test cases were accurate despite the small environmental dimension. In the case of non-unitary effects, the discrepancies between the exact and approximate results are quite small and the accuracy of the CKD is directly proportional to the degree of chaos in the environment. In the strongly chaotic regime, the highest degree of accuracy was obtained in all cases. In the case of unitary effects, very good quantitative agreement was achieved in all cases, irrespective of the degree of chaos in the environment. Overall, the accuracy of the CKD in predicting the exact results is satisfactory and thus the CKD may be a valuable computational tool for low temperature

simulations of new quantum technologies where other applicable theories of self-interacting and chaotic environments are mostly limited to high temperature applications.

1.4 Collaborative versus individual work

The work presented in this thesis is published in five journal articles by Çetinbaş and Wilkie [14-18]. The majority of the published work is based on the ideas of the author of this thesis. These ideas were elaborated in collaboration with Wilkie. In addition, the author of the thesis contributed to the five published articles [14-18] by conceiving and developing the physical models, writing all the computer codes, executing all the calculations, producing all the graphics, writing the first drafts of all the manuscripts, and finally corresponding with the journals.

Chapter 2

Kraus decomposition for chaotic environments

In this chapter [§], a simple formula predictiug the dynamics of a quautum subsystem interacting with large chaotic environments is derived. This formula is of the Kraus Operator Sum Representation (OSR) [53] form, which automatically satisfies all the required conservation laws for the reduced density operator. The chaotic Kraus decomposition (CKD) constitutes a formally exact equation of motion for the reduced density operator in terms of explicit representations of the Kraus operators. Aside from the quantum chaos, the only required property of thc bath Hamiltonian is that it be of thermodynamic dimension (i.e. very large).

The organization of this chapter is as follows. In section 2.1, the Liouville-von Neumann equatiou is introduced and iu section 2.2, the reduced density operator formalism is discussed. In section 2.3, basic ideas behind the Kraus OSR are reviewed by using thc simplest possible case where the subsystem Hamiltonian is time-independent and the system-environment interactiou operator includes only one term. In section 2.4 it is argued

[§]This chapter is based on two studies [14, 15] reported by Çetinbaş and Wilkie.

that off-diagonal matrix elements of the environment interaction operator are negligible for large chaotic environments. Using this property it is shown in section 2.5 that the resulting Kraus decomposition, i.e. the CKD, takes a particularly simple and potentially useful form. In section 2.6, an extension of the CKD to time-dependent system Hamiltonians and more general system-environment interaction operators is provided so that the CKD can be more widely applicable. In section 2.7, a numerical strategy for the CKD is summarized and it is shown that the CKD can be practically used for computational purposes.

2.1 Liouville–von Neumann equation

The dynamics of a closed quantum system, represented by a Hamiltonian, $\hat{H}$, evolve from the Schrödinger equation,

$$i\hbar\frac{d}{dt}|\Psi(t)\rangle = \hat{H}|\Psi(t)\rangle. \tag{2.1}$$

The Schrödinger equation is a first order differential equation in time, the solution of which is of the form,

$$|\Psi(t)\rangle = \hat{U}(t)|\Psi(0)\rangle, \tag{2.2}$$

where the unitary propagator, $\hat{U}^{\dagger}(t) = \hat{U}^{-1}(t)$, takes a simple form,

$$\hat{U}(t) = \exp\{-(i/\hbar)\hat{H}t\}, \tag{2.3}$$

for time-independent Hamiltonians. In the case of time-dependent Hamiltonians, $\hat{H}(t)$, the propagator takes the form

$$\begin{aligned}
\hat{U}(t) &= \hat{\mathcal{T}}\exp\left\{-(i/\hbar)\int_0^t \hat{H}(t')dt'\right\} \\
&= \hat{1} + (-i/\hbar)\int_0^t dt_1\ \hat{H}(t_1) \\
&\quad +(-i/\hbar)^2\int_0^t dt_1\int_0^{t_1} dt_2\ \hat{\mathcal{T}}\hat{H}(t_1)\hat{H}(t_2) \\
&\quad +(-i/\hbar)^3\int_0^t dt_1\int_0^{t_1} dt_2\int_0^{t_2} dt_3\ \hat{\mathcal{T}}\hat{H}(t_1)\hat{H}(t_2)\hat{H}(t_3) \\
&\quad +\cdots
\end{aligned} \tag{2.4}$$

where $\hat{\mathcal{T}}$ is the time ordering operator, which has an important implication when $\hat{H}(t)$ does not commute with itself for different times, i.e. $[\hat{H}(t), \hat{H}(t')] \neq 0$ for $t \neq t'$. The time ordering operator states that the chronological ordering, i.e. $t_1 < t_2 < t_3 \cdots < t$ should be obeyed for all times. However, in cases where $[\hat{H}(t), \hat{H}(t')] = 0$ holds for $t \neq t'$, the time ordering operator can be omitted from equation (2.4).

The Schrödinger equation is restricted to state vectors, which are not the most general states to represent a physical system, however. A general description of a state of a quantum system can readily be achieved by density operators [1]. Density operators, $\hat{\rho}$, should satisfy three mathematical conditions to be allowed as state operators. They should be

(i) normalized, i.e. $\mathrm{Tr}[\hat{\rho}] = 1$,

(ii) Hermitian, i.e. $\hat{\rho} = \hat{\rho}^\dagger$,

(iii) positive definite or non-negative, i.e. $\langle\phi|\hat{\rho}|\phi\rangle \geq 0$ where $|\phi\rangle$ is an arbitrary vector.

State vectors are pure quantum states that can be distinguished from non-pure states (i.e. statistical mixtures) by the condition $\mathrm{Tr}[\hat{\rho}^2] = 1$. Hence, the non-pure states satisfy $\mathrm{Tr}[\hat{\rho}^2] < 1$. There is a one-to-one correspondence between state vectors and pure density operators. This correspondence can readily be established with the following derivation of pure state operators from state vectors, i.e. $\hat{\rho} = |\phi\rangle\langle\phi|$, where $|\phi\rangle$ is an arbitrary normalized vector, i.e. $\langle\phi|\phi\rangle = 1$. The non-pure states can also be obtained from the pure states as follows. Let $\hat{\rho}$ be a non-pure state, i.e. $\mathrm{Tr}[\hat{\rho}^2] < 1$. Since, by definition, $\hat{\rho}$ is Hermitian, a unique spectral decomposition always exists: $\hat{\rho} = \sum_i p_i|i\rangle\langle i|$, where $\hat{\rho}|i\rangle = p_i|i\rangle$ and $\sum_i p_i = 1$.

The dynamics of density operators, whether they are pure or non-pure, evolve from the Liouville–von Neumann equation, which can be obtained from the Schrödinger equation in the following way. Consider an arbitrary density operator of the form, $\hat{\rho}(0) = \sum_i p_i|i\rangle\langle i|$. Since $\mathrm{Tr}\{|i\rangle\langle i|\} = \langle i|i\rangle = 1$, each $|i\rangle$ obeys the the Schrödinger equation. Hence, by use of

equations (2.2) and (2.3), the exact equation of motion for the density operator is obtained:

$$\hat{\rho}(t) = \hat{U}(t)\hat{\rho}(0)\hat{U}^{\dagger}(t) = \sum_{i} p_i \hat{U}(t)|i\rangle\langle i|\hat{U}^{\dagger}(t), \tag{2.5}$$

which is the solution of the Liouville–von Neumann equation,

$$i\frac{d}{dt}\hat{\rho}(t) = \hat{L}\hat{\rho}(t). \tag{2.6}$$

Here, the Liouville operator is defined as $\hat{L} \equiv (1/\hbar)\left[\hat{H}, \cdot\right]$, where $[\cdot\,,\cdot]$ is a commntator.

2.2 Dynamics of a reduced density operator

In principle, the time–evolved density operator of a quantum system, evolving from the Liouville–von Neumann equation (2.6), provides complete probabilistic information for all observable quantities. However, the Liouville–von Neumann equation (2.6) allows neither exact analytical nor numerical solution when the environment degree of freedom is very large. Most of the time a physical system of interest is only a part of a much larger system. For example, a reaction coordinate in a large biological molecule is physically more interesting and important than the rest of the molecule because that is where the dynamical changes occur. Therefore, a subsystem-environment scheme is employed as a starting point to formulate the dynamics of a quantum system of interest. Henceforth, the physically interesting part of a large quantum system will be referred to as the subsystem or simply the system, and the rest of this large quantum system as a bath or an environment.

The reduced density operator of a system is obtained by taking a partial trace over the bath degrees of freedom,

$$\hat{\rho}_S(t) = \mathrm{Tr}_B[\hat{\rho}(t)], \tag{2.7}$$

where $\hat{\rho}(t)$ is the solution of Liouville–von Neumann equation (2.6) for the composite system (i.e. the subsystem plus the environment). The reduced density operator of a subsystem suffices to provide complete probabilistic information for all observable quantities within

the subsystem degree of freedom and the reduced density operator also satisfies three basic mathematical conditions, i.e. $\hat{\rho}_S(t)$ is normalized, Hermitian, and positive definite; see e.g. Ref. [1].

In the next section, the system, environment, interaction operators, and initial conditions are defined and then it is shown how the open system dynamics of a reduced density operator can be expressed in terms of Kraus operators.

2.3 Kraus operator sum representation

Consider the system and environment degrees of freedom as a bipartite closed system, represented by a total Hamiltonian of the form,

$$\hat{H} = \hat{H}_S + \hat{S}\hat{B} + \hat{H}_B, \tag{2.8}$$

where $\hat{H}_S$ is the system Hamiltonian, $\hat{S}$ and $\hat{B}$ are the system and environment interaction operators, respectively, and $\hat{H}_B$ is the bath or the environment Hamiltonian.

Assume that the system and environment degrees of freedoms are uncorrelated initially,

$$\hat{\rho}(0) = \hat{\rho}_S(0) \otimes \hat{\rho}_B(0), \tag{2.9}$$

where $\hat{\rho_S}(0)$ is an arbitrary initial state for the system and $\hat{\rho}_B(0)$ is an initial environment state of canonical form, i.e.

$$\hat{\rho}_B(0) = \sum_m |m\rangle \frac{e^{-\beta E_m}}{Q} \langle m|. \tag{2.10}$$

Here, $Q = \sum_n \exp\{-\beta E_n\}$ is the partition function and $\beta = 1/k_B T$ is the inverse temperature where k_B is the Boltzmann constant. Note that the canonical bath density is constructed by using the exact eigenvalues and eigenvectors of the bath Hamiltonian, $\hat{H}|n\rangle = E_n|n\rangle$, for which the usual completeness relation applies: $\hat{I} = \sum_n |n\rangle\langle n|$ and $\langle n|m\rangle = \delta_{n,m}$.

For Hamiltonian (2.8) and initial condition (2.9), the exact time evolution of the density operator, $\hat{\rho}(t)$, is given by the solution of the Liouville-von Neumann equation (2.6). The

exact subsystem density operator, $\hat{\rho}_S(t)$, is obtained by tracing over the environment degrees of freedom, i.e.

$$\hat{\rho}_S(t) = \mathrm{Tr}_B[\hat{U}(t)\hat{\rho}(0)\hat{U}^\dagger(t)]. \tag{2.11}$$

Since the initial canonical bath density is already diagonal in eigenstates of $\hat{H}_B$, performing the partial trace operation in the same basis, $\{|n\rangle\}$, yields

$$\hat{\rho}_S(t) = \sum_{n,m}\langle n|\hat{U}(t)\left(\hat{\rho}_S(0)\otimes\frac{e^{-\beta E_m}}{Q}|m\rangle\langle m|\right)\hat{U}^\dagger(t)|n\rangle. \tag{2.12}$$

This equation can now be written in a compact form,

$$\hat{\rho}_S(t) = \sum_{n,m}\hat{\mathcal{K}}_{n,m}(t)\hat{\rho}_S(0)\hat{\mathcal{K}}^\dagger_{n,m}(t), \tag{2.13}$$

in terms of the following Kraus operators [53],

$$\hat{\mathcal{K}}_{n,m}(t) = \sqrt{p_m}\langle n|\hat{U}(t)|m\rangle, \tag{2.14}$$

where $p_m = \exp\{-\beta E_m\}/Q$ are the initial populations of the bath density operator. For a Hermitian Hamiltonian it is always true that

$$\sum_{n,m}\hat{\mathcal{K}}_{n,m}(t)\hat{\mathcal{K}}^\dagger_{n,m}(t) = \hat{I}_S. \tag{2.15}$$

This is the normalization condition for the Kraus OSR [53], from which it follows that the open system dynamics are unitary if and only if the Kraus decomposition (2.13) has only one term.

The above form of the Kraus OSR (2.13) is exact and thus satisfies all the required conservation laws on the subsystem density, i.e. the Hermiticity, positivity, and norm conservation. However, the exactness of decomposition is of formal interest only, as it is not practical for computational purposes and the explicit form of the Kraus operators (2.14) are extremely hard to obtain. Moreover, even if the explicit form of the Kraus operators were known, the double summation above would render the Kraus decomposition impractical. Fortunately, for a quantum subsystem interacting with large chaotic environments, the

explicit form of the Kraus operators can easily be obtained and the double summation also reduces to a single summation.

2.4 Chaotic environments

Quantum chaos has a number of important consequences for eigenspectra and matrix elements of Hamiltonians [23, 24]. The most distinguishing and well-known feature of chaotic Hamiltonians is the changes in the statistical properties of their eigenspectra. Eigenspectra of chaotic Hamiltonians display energy level repulsion. On the other hand, Hamiltonians of regular systems (i.e. non-chaotic systems) show a high degree of degeneracy and energy level clustering in their spectra. While the eigen-statistics of a regular system are Poissonian, the chaotic eigen-statistics are given by the Wigner-Dyson distribution.

During the transition from a regular to a chaotic regime, not only the eigenspectra but also the properties of eigenstates dramatically change. As a result, matrix elements of operators in the eigenbasis of chaotic Hamiltonians show quite different features. A particular property that will be used in the derivation of the CKD is that the off-diagonal matrix elements of the bath coupling operator in the eigenbasis of a chaotic environment Hamiltonian become negligibly small or vanish when the dimension of the chaotic environment is very large. This result has been known for two decades in the quantum chaos literature [31, 32], but its consequences for the Kraus OSR have not been recognized.

Using the exact bath eigenvalues and eigenstates, $\hat{H}_B|n\rangle = E_n|n\rangle$, the total Hamiltonian (2.8) can be written in the following alternative form,

$$\hat{H} = \hat{H}_S + \hat{S}\sum_{n,m} B_{n,m}|n\rangle\langle m| + \sum_n E_n|n\rangle\langle n|, \tag{2.16}$$

where $B_{n,m} = \langle n|\hat{B}|m\rangle$ are the matrix elements of the bath coupling operator, $\hat{B}$. Effects induced by system-environment interactions may depend on many factors, such as the properties of matrix elements $B_{n,m}$, and the operators $\hat{S}$ and $|n\rangle\langle m|$. Here, the focus is on the

properties of $B_{n,m}$ because quantum chaos has a number of important consequences for these matrix elements.

At the semi-classical limit [§], the square of the off-diagonal matrix elements of an operator, e.g. $\hat{B}$, scale as $|B_{n,m}|^2 \propto h^N$ where N is the number of environment modes [29, 31, 32]. Since the Planck constant is small, these off-diagonal matrix elements should be negligibly small for sufficiently large N. Alternatively, it has also been shown in [14] that the off-diagonal matrix elements should also be negligible when the number of environment degrees of freedom approach the thermodynamic limit, i.e. $N \to \infty$. Explicit mathematical derivations of the semi-classical [29, 31, 32] and thermodynamic [14] arguments require an advanced mathematical knowledge of the phase space representation of quantum mechanics [80] as well as rules of quantum-classical correspondence [81]. Here, the interest is in the consequence of these arguments for the Kraus OSR rather than derivations of these arguments. Interested readers can find these derivations in [14, 29, 31, 32]. Below, these arguments are shortly reviewed.

Semi-classical limit for chaotic environments

The semi-classical argument presented here is taken from Ref. [29]. More detailed discussions regarding derivations of the formulas given below can be found in [31, 32]. At the semi-classical limit, diagonal matrix elements of an operator, e.g. $\hat{B}$, represented in the basis of a large chaotic Hamitonian, e.g. $\hat{H}_B$, are given by the formula

$$B_{n,n} = \langle n|\hat{B}|n\rangle \simeq \frac{\int d\mathbf{x}\ \delta[E_n - H(\mathbf{x})]B(\mathbf{x})}{\int d\mathbf{x}\ \delta[E_n - H(\mathbf{x})]} = \langle B\rangle \tag{2.17}$$

[§]The semi-classical limit refers to an approximate limit where quantum mechanics embraces classical mechanics as a limiting case. Loosely stated, this limit can be $h \to 0$. That is, the Planck constant is negligibly small as compared to the other relevant dynamical parameters. Or, this limit can be a large quantum number limit where dynamical variables such as angular momentum or energy are very large as compared to the relevant quantum unit chosen. A detailed discussion of quantum-classical correspondence including criticisms of the aforementioned limits can be found, for example, in Ref. [1].

Here $\langle B \rangle$ is a microcanonical average calculated at the energy $E = E_n$, the composite variable $\mathbf{x} = (\mathbf{p}, \mathbf{q})$ represents $6N$ momenta $\mathbf{p}$ and coordinates $\mathbf{q}$ of the bath, $B(\mathbf{x})$ is the Wigner function of $\hat{B}$. The off-diagonal matrix elements of this operator are given by

$$|B_{n,m}|^2 \simeq h^N \frac{\int_{-\infty}^{\infty} dt \, \langle [B(0) - \langle B \rangle][B(t) - \langle B \rangle] \rangle \exp\left[i(\bar{E}_n - \bar{E}_m)t/\hbar\right]}{\int d\mathbf{x} \; \delta[(\bar{E}_n + \bar{E}_m)/2 - \bar{H}(\mathbf{x})]} \tag{2.18}$$

Here $\bar{E}_n = \bar{N}(E_n)$ are the unfolded energies, not the actual eigenenergies and therefore, $\bar{N}(E)$ gives the average number of levels below E_n rather then the eigenenergies themselves. The microcanonical averages are calculated at the unfolded energy $(\bar{E}_n + \bar{E}_m)/2$. It is worthwhile to note that equation (2.18) is only valid when the level spacing between unfolded levels are constant.

The time correlation function appearing in equation (2.18) decays exponentially fast $\exp(\Omega^2 t^2)$ at short times where Ω is the spectral width. It follows then that equation (2.18) simplifies to

$$|B_{n,m}|^2 \propto h^N \exp\left[-(\bar{E}_n - \bar{E}_m)^2/4\Omega^2\hbar^2\right]. \tag{2.19}$$

Hence, since the Planck constant h is small and the number of bath modes N is large, the scaling $|B_{n,m}|^2 \propto h^N$ indicates that the off-diagonal matrix elements should be negligible for sufficiently large environments.

Thermodynamic limit for chaotic environments

The argument presented here is taken from Ref. [14] where it is shown that the square of the off-diagonal matrix elements $|B_{n,m}|^2 \to 0$ become negligibly small when the number of bath modes approaches the thermodynamics limit, i.e. $N \to \infty$.

By combining two exact equations (50) and (119) of Ref. [31] one can obtain the following exact equation for the off-diagonal matrix elements of an arbitrary quantum system

$$|B_{n,m}|^2 = \left(\frac{h}{I_{n,m}}\right)^N \int d\mathbf{x} \; d\mathbf{x}_0 \; B(\mathbf{x})^* B(\mathbf{x}_0) \int d\mathbf{y} \; e^{2\pi i(\mathbf{x}-\mathbf{x}_0)J\mathbf{y}} \; W_n(\mathbf{x} + h\mathbf{y}/2) W_m(\mathbf{x}_0 - h\mathbf{y}/2). \tag{2.20}$$

where $B(\mathbf{x})$ is the Wigner function [80] of the operator $\hat{B}$ and the scaled Wigner function for eigenstate n is given by

$$W_n(\mathbf{x}) = C_n \int d\mathbf{v}\ e^{2\pi\imath \mathbf{p}\mathbf{v}} \langle \mathbf{q} - h\mathbf{v}/2|n\rangle\langle m|\mathbf{q} + h\mathbf{v}/2\rangle \tag{2.21}$$

where $C_n = [\int d\mathbf{x}\ \delta(1 - H_B(\mathbf{x})/E_n)]^{1/2}$ and $I_{n,m} = (C_n C_m)^{1/N}$ and J is a symplectic matrix of dimension $2N \times 2N$. It is shown [81] that $W_n(\mathbf{x})$ has a well–defined classical limit if the classical Hamiltonian $H_B(\mathbf{x})$ is chaotic. Note also that the Wigner function of quantum Hamiltonian $\hat{H}_B$ may differ from the classical Hamiltonian by small corrections which should vanish with Planck's constant.

It is shown in [14] that $\int d\mathbf{x}\ \delta(1 - H_B(\mathbf{x})/E_n) \propto E_n e^{S_n/k_B}$ where S_n is the microcanonical entropy and k_B is the Boltzmann constant. Since entropy is an extensive variable, S_n scales linearly with N for sufficiently large N. As a result, it follows from l'Hôpital's rule that C_n scales exponentially with N, which in turn suggests that $I_{n,m}$ is constant, or at most grows weakly with N since the energies E_n also increase with N.

The Wigner functions $W_n(\mathbf{x})$ and $B(\mathbf{x})$ and the associated integrals in (2.20) have well–defined classical [81] and thus thermodynamic limits. For example, in the classical limit, these terms reduce to $E_n\delta(E_n - E_m)\overline{B^2}$, which increases gradually with N. Here $\overline{B^2}$ is the classical canonical average of the squared classical limit of the Wigner function for $\hat{B}$. Note that $\hat{B} \propto \sqrt{N}$ and so $\overline{B^2}$ would normally scale linearly with N. $E_n\delta(E_n - E_m)$ is only weakly dependent on N. Note also that $\delta(E_n - E_m)$ should be understood as a distribution with a small but nonzero width. Thus, by l'Hôpital's rule, the magnitude of $|B_{n,m}|^2$ in the thermodynamic limit is determined by the factor $(\frac{h}{I_{n,m}})^N$. Consequently, if $h < I_{n,m}$, which should always be true for sufficiently large N, then $|B_{n,m}|^2 \to 0$ exponentially fast as $N \to \infty$. Hence, the off-diagonal matrix elements of $\hat{B}$ should be negligibly small for a chaotic bath of thermodynamic dimension.

The effect of suppression of decoherence by chaotic environments was observed for finite chaotic spin–baths, see e.g. [29, 30]. In the light of these studies [29, 30], it is arguable

that for such small spin-baths neither the semi-classical limit is well-defined nor may thermodynamic limit be attained. Therefore, while the off-diagonal matrix elements for small chaotic spin-baths can be very small, they should not be totally vanishing. Here, by simply assuming that $B_{n,m} = 0$ for $n \neq m$ for sufficiently large chaotic environments, a Kraus decomposition, i.e. the CKD will be derived in the next section. Since this assumption cannot always be valid for small chaotic environments, the question as to whether the assumption $B_{n,m} = 0$ is justifiable for small chaotic environments needs to be examined. The test results reported in [14, 15] and presented in chapter 6 show very good agreement between exact and CKD results, which suggests that $B_{n,m} = 0$ is a reasonable approximation at least for the test models studied in chapter 6. Moreover, in chapter 7 it is further verified that chaotic intra-bath interactions indeed lead to small off-diagonal matrix elements when chaos generating intra-bath interactions and system-environment interactions are of similar kind; nevertheless, inspections of off-diagonals indicate that not every one of these matrix elements are zero, as may be expected.

2.5 Chaotic Kraus decomposition

By using the assumption, $B_{n,m} = 0$ for $n \neq m$, the Hamiltonian (2.16) can be written as

$$\hat{H} = \hat{H}_S + \sum_n (\hat{S}B_{n,n} + E_n)|n\rangle\langle n|. \tag{2.22}$$

For integer powers of $l = 0, .., \infty$, the matrix elements of the total Hamiltonian obey the relation,

$$\langle n|\hat{H}^l|m\rangle = \left(\hat{H}_S + \hat{S}B_{n,n} + E_n\right)^l \delta_{n,m} \tag{2.23}$$

for all n and m. By using this in a Taylor expansion,

$$e^{-\frac{i}{\hbar}\hat{H}l} = \sum_{l=0}^{\infty} \frac{(-i\hat{H}t)^l}{\hbar^l l!}, \tag{2.24}$$

it follows that the Kraus operators (2.14) take a simple form

$$\hat{K}_{n,m}(t) = \sqrt{p_m} e^{-\frac{i}{\hbar}(\hat{H}_S + \hat{S}B_{m,m} + E_m)l} \delta_{n,m}. \tag{2.25}$$

By substituting this back into (2.13), the final form of the CKD is obtained:

$$\hat{\rho}_S(t) = \sum_m \frac{e^{-\beta E_m}}{Q} e^{-\frac{i}{\hbar}(\hat{H}_S + \hat{S}B_{m\,m})t} \hat{\rho}_S(0) e^{\frac{i}{\hbar}(\hat{H}_S + \hat{S}B_{m,m})t}. \tag{2.26}$$

The CKD has a suggestive form. For example, in the case where all diagonal coupling matrix elements are identical, i.e. $B_{m,m} = B$, the CKD reduces to

$$\hat{\rho}_S(t) = e^{-\frac{i}{\hbar}(\hat{H}_S + \hat{S}B)t} \hat{\rho}_S(0) e^{\frac{i}{\hbar}(\hat{H}_S + \hat{S}B)t}, \tag{2.27}$$

which suggests that all non-unitary effects disappear and the only effect induced by the environment is the coherent shifting, i.e. $\hat{H}_S \rightarrow \hat{H}_S + \hat{S}B$.

Similarly, at absolute zero temperature, or provided that the bath state is a pure state, there will be no decoherence or dissipation but only coherent shifting. Hence, a chaotic environment of thermodynamic dimension cannot induce decoherence or dissipation at absolute zero temperature. This is an interesting prediction because there is no such restriction on the regular environments which are known to cause strong decoherence even at absolute zero temperature.

2.6 Time-dependent extension of chaotic Kraus decomposition

In this section, a time-dependent extension of the CKD is derived, which may have wider applications than the version developed in the previous section. The general structure of the argument used here will be similar to that of the previous section. Now, consider a more general Hamiltonian, which is of the form,

$$\hat{H}(t) = \hat{H}_S(t) + \sum_\mu \hat{S}_\mu \hat{B}_\mu + \hat{H}_B, \tag{2.28}$$

where $\hat{H}_S(t) = \hat{H}_S + \hat{\mathcal{E}}(t)$ consists of the time-independent free system Hamiltonian, $\hat{H}_S$, and the time-dependent Hamiltonian representing external driving fields, $\hat{\mathcal{E}}(t)$. Here, $\hat{S}_\mu$

and $\hat{B}_\mu$ are interaction operators in the system and bath degrees of freedom, and $\hat{H}_B$ is a chaotic Hamiltonian for a large environment.

The total Hamiltonian (2.28) can be written in terms of the bath eigenvalues and eigenvectors as follows,

$$\hat{H} = \hat{H}_S(t) + \sum_\mu \hat{S}_\mu \sum_{n,m} B_\mu^{n,m} |n\rangle\langle m| + \sum_n E_n |n\rangle\langle n|, \tag{2.29}$$

where $B_\mu^{n,m} = \langle n|\hat{B}_\mu|m\rangle$ are the matrix elements of the interaction operator in the complete bath eigenbasis. The argument discussed in section 2.4 suggests that the off-diagonal matrix elements of the bath interaction operator vanish, i.e. $B_\mu^{n,m} \to 0$, for large chaotic environments. Using this property the total Hamiltonian (2.29) simplifies to

$$\hat{H} = \hat{H}_S(t) + \sum_m (\sum_\mu \hat{S}_\mu B_\mu^{m,m} + E_m)|m\rangle\langle m|. \tag{2.30}$$

Magnus expansion [82] of (2.14), by using the above Hamiltonian (2.30), then gives

$$\begin{aligned}
\hat{\mathcal{K}}_{n,m}(t) = \sqrt{p_m}\langle n|[1 &+ (-i/\hbar)\int_0^t dt_1\ \hat{H}(t_1) \\
&+(-i/\hbar)^2 \int_0^t dt_1 \int_0^{t_1} dt_2\ \hat{\mathcal{T}}\hat{H}(t_1)\hat{H}(t_2) \\
&+(-i/\hbar)^3 \int_0^t dt_1 \int_0^{t_1} dt_2 \int_0^{t_2} dt_3\ \hat{\mathcal{T}}\hat{H}(t_1)\hat{H}(t_2)\hat{H}(t_3) + \ldots]|m\rangle
\end{aligned} \tag{2.31}$$

which, since $\hat{H}(t)$ is block diagonal in the bath eigenbasis, simplifies to

$$\begin{aligned}
\hat{\mathcal{K}}_{n,m}(t) = \sqrt{p_m}[1 &+ (-i/\hbar)\int_0^t dt_1\ \langle n|\hat{H}(t_1)|n\rangle \\
&+(-i/\hbar)^2 \int_0^t dt_1 \int_0^{t_1} dt_2\ \hat{\mathcal{T}}\langle n|\hat{H}(t_1)|n\rangle\langle n|\hat{H}(t_2)|n\rangle \\
&+(-i/\hbar)^3 \int_0^t dt_1 \int_0^{t_1} dt_2 \int_0^{t_2} dt_3\ \hat{\mathcal{T}}\langle n|\hat{H}(t_1)|n\rangle\langle n|\hat{H}(t_2)|n\rangle\langle n|\hat{H}(t_3)|n\rangle \\
&+ \ldots]\delta_{n,m}.
\end{aligned} \tag{2.32}$$

Now, using the Magnus expansion [82] in reverse gives

$$\hat{\mathcal{K}}_{n,m}(t) = \sqrt{p_m}\ \hat{\mathcal{T}} \exp\left\{-\frac{i}{\hbar}\int_0^t dt'(\hat{H}_S(t') + \sum_\mu \hat{S}_\mu B_\mu^{m,m} + E_m)\right\}\delta_{n,m} \tag{2.33}$$

which in turn can be substituted into (2.13) to obtain the final form of the CKD,

$$\hat{\rho}_S(t) = \sum_m \hat{\mathcal{K}}_{m,m}(t)\hat{\rho}_S(0)\hat{\mathcal{K}}^\dagger_{m,m}(t), \tag{2.34}$$

where the double sum in equation (2.13) becomes a single sum and $\hat{\mathcal{K}}_{m,m}(t)$ are now given by (2.33). Equation (2.34) is the final form of the CKD, which extends equation (2.26) to time-dependent subsystem Hamiltonians and more general system-environment interaction operators.

2.7 Numerical strategy

The CKD (2.34) is exact only for large thermodynamic chaotic environments. The exact numerical results that can be obtained on a computer are limited to small environments. However, the test results reported in [14, 15] and also presented in this thesis suggest that the CKD gives accurate results even for small environments. Hence, the CKD can be used as a practical computational tool. Here it is shown how equation (2.34) can be employed in practice.

Given the initial subsystem state of the form, $\hat{\rho}_S(0) = |\psi(0)\rangle\langle\psi(0)|$, the time evolved states can be defined as

$$|\psi_m(t)\rangle = \hat{\mathcal{T}} \exp\left\{-\frac{i}{\hbar}\int_0^t dt'(\hat{H}_S(t') + \sum_\mu \hat{S}_\mu B^{m,m}_\mu)\right\}|\psi(0)\rangle \tag{2.35}$$

such that the reduced density is of the form,

$$\hat{\rho}_S(t) = \sum_m p_m|\psi_m(t)\rangle\langle\psi_m(t)|, \tag{2.36}$$

where $|\psi_m(t)\rangle$ evolves from the Schrödinger equation,

$$d|\psi_m(t)\rangle/dt = -(i/\hbar)[\hat{H}_S(t) + \sum_\mu \hat{S}_\mu B^{m,m}_\mu]|\psi_m(t)\rangle. \tag{2.37}$$

These equations (2.37) can easily be solved by using standard integration techniques. For non-pure initial conditions, rather than solving the Schrödinger equation, the Liouville-von

Neumann equation can be numerically solved,

$$d\hat{\rho}_S^m(t)/dt = -(i/\hbar)[\hat{H}_S(t) + \sum_\mu \hat{S}_\mu B_\mu^{m,m}, \hat{\rho}_S^m(t)], \tag{2.38}$$

with $\hat{\rho}_S^m(0) = \hat{\rho}_S(0)$, from which the reduced density operator can be constructed with formula, $\hat{\rho}_S(t) = \sum_m p_m \hat{\rho}_S^m(t)$.

At very low temperatures, where new quantum technologies are expected to operate, the number of populated bath states will be quite small and so will be the uumber of Kraus operators in equation (2.34). Hence, the CKD can serve as a practical computational tool for low temperature applications.

Chapter 3

Quantum computers with static internal flaws

Quantum computers (QCs) are subject to internal sources of error in addition to those resulting from external environmental interactions. Internal decoherence, dissipation, and coherent shifting originate from uncontrollable interactions between pairs of qubits. In this chapter[§], to study the relative importance of the internal errors, a QC model is developed which consists of a CNOT gate performed on two qubits of a many-qubit isolated QC with static internal imperfections. The motivations behind this study are discussed in section 3.1. In section 3.2 mathematical details of an isolated QC model are given. The isolated QC core is mapped onto a subsystem-environment scheme wherein the active part of the QC, i.e. a two-qubit register (the subsystem), performs a CNOT gate while interacting with the neighboring qubits (the environment). By defining a variety of configurations, i.e. eight different initial register states, two different error generators (phase and bit-flip errors) and five different intra-enviromental interaction strengths, the exact quantum dynamics of the QC will be obtained. In section 3.3, an exact numerical approach used

[§]This chapter is based on two studies [16, 17] reported by Çetinbaş and Wilkie.

in QC simulations is explained and parameters used in the exact calculations are defined. Finally, in section 3.4 error quantifiers, i.e. purity and fidelity are defined. These error quantifiers are used to measure extent of deviation from the ideal CNOT dynamics and distinguish non-unitary errors (i.e. decoherence and dissipation) from those of unitary type (i.e. coherent distortions).

3.1 Motivations

Decoherence due to an external macroscopic environment [2] is widely believed to be the primary obstacle to the development of quantum computing technologies [6-8]. However, even in the absence of an external environment, the efficient operability of an *isolated* QC is not guaranteed. This is due to the fact that the destructive effects induced by one-body imperfections and two-body residual interactions between qubits can still endanger the performance of a QC.

The origin of one-body qubit imperfections is due to slightly different energy spacings between the two levels of distinct qubits. This type of imperfection is expected especially for manufactured qubits such as quantum dot qubits (artificial atoms) and superconducting qubits. However, one-body imperfections may also arise in qubits which are not genuine but effective two level systems. For example, if the ground and first excited state of an atom form a qubit, a possible excitation of the atom to higher energy levels can lead to a one-body imperfection. In the case that all qubits are identical and thus are of the same energy spacing, one-body imperfections may also be induced by interactions of qubits with local impurities. Two-body residual interactions are interactions between pairs of qubits. Such interactions are expected because qubits of a QC may not be well isolated from one another. Moreover, certain quantum operations can only be performed by inducing a coupling between pairs of qubits by external manipulations. The external manipulations may not be perfect and lead to residual interactions between qubits.

Recent studies on the statistical properties of flawed QCs suggest that chaos emerges in a QC core as a result of strong residual qubit–qubit interactions [72-77]. The chaos leads to a dynamical thermalization [74] and a consequent destruction of the ideal computational states of a QC. However, the studies in which the static internal flaws are modeled by chaotic random matrices show that chaotic perturbations can actually stabilize the QC dynamics [76-78]. These contradictory results, i.e. destruction and stabilization of a QC with chaos, suggest that there is no consensus yet on how internal flaws affect the performance of the various sorts of quantum gates, nor is the precise nature of internal errors identified. Questions as to what operations are most vulnerable to internal errors need to be addressed and the effects of chaos on the internal errors need to be determined. There is also the issue of which initial states are most adversely affected. Thus, there are many open questions about the consequences of internal flaws on the performance of a QC in the presence of imperfections.

Previous studies of flawed QCs do not address the specifics of an operating isolated QC architecture. Nor do these models address what specifically happens to an algorithm in the presence of internal flaws. An ideal gate sequence for one architecture may be quite different from that of another architecture. Hence, it is of an interest to know what parts of an algorithm are affected most (e.g. one- or two-qubit gates), and whether they are irreversibly altered via internal decoherence or dissipation, or merely coherently distorted. A prior knowledge of such information could be important for optimizing performance of a QC architecture and further development of error correction schemes [79]. Hence, there are many questions that cannot be meaningfully investigated in the context of random matrix formulation or other abstract models for the environment. A closer examination of the effects of internal errors in actual QC proposals is thus warranted.

Residual qubit–qubit interactions arising in a QC core mix the ideal computational states (i.e. uncoupled) of qubits [72-74]. While residual qubit-qubit interactions are also

responsible for the onset of chaos in a QC core, the mixing process may occur even below the chaos border [75]. Hence, in the presence of residual qubit-qubit interactions, whether these interactions generate chaos or not, an undesirable correlation or mixing of computational states of qubits is unavoidable. In such a situation, even if the QC core is totally isolated from its surrounding environment, the qubits within the isolated QC core may still experience their own nearby microscopic qubit euvironment and are then subject to internal sources of decoherence, dissipation and coherent shifting. To investigate these internal errors, a subsystem-environment scheme is an appropriate approach. In such a subsystem-environment scheme, the system part consists of one or two active qubits that perform a quantum protocol while the rest of the QC can be considered as inactive or idle, for the sake of simplicity. The active and idle parts interact via residual qubit–qubit interactions, and the generation of errors as well as the dynamical behavior of these errors due to changes in the idle part can be monitored, which is the approach taken in this study.

This study is focused on the dynamics of a two-qubit subsystem interacting with a larger nearby qubit environment. The two-qubit subsystem (i.e. the active part) performs a CNOT gate while the rest of the qubits (i.e. the environment) are idle. That is, they do not perform a predetermined quantum algorithm. The effects of imperfections are simulated by adding one– and two body imperfections to the idle part and then exploring the dynamical changes in the active part.

3.2 Description of isolated QC model

The total Hamiltonian for the isolated QC is of the form,

$$\hat{H}(t) = \hat{H}_S(t) + \hat{S}\hat{B} + \hat{H}_B, \tag{3.1}$$

where $\hat{H}_S(t)$ is the time–dependent control Hamiltonian of a two–qubit register performing a CNOT gate (i.e. the subsystem Hamiltonian), $\hat{S}\hat{B}$ is the interaction operator, $\hat{S}$ acting in

the system and $\hat{B}$ acting in the bath degree of freedom, and $\hat{H}_B$ is the bath Hamiltonian of the idle qubits.

The isolated QC model is parameterized based on a Josephson junction charge qubit (JJCQ) QC proposal [69]. This scalable architecture has a very long external decoherence time, $\sim 10^{-4}$ s, which in principle allows approximately 10^6 single qubit operations. Such a QC architecture with very long coherence time is an ideal system to study internal decoherence dynamics. In the following section, the basic design and operation principle of a JJCQ is presented, and then the explicit forms of different components of $\hat{H}(t)$ are given.

3.2.1 Josephson junction charge qubit device

Josephson junction QC architectures are promising quantum information processor candidates due to their long external decoherence times and scalability, with ease for a large number of qubits [68]. A typical charge qubit in its simplest design form is illustrated in figure 3.1. A JJCQ is a tiny circuit consisting of a Josephson junction capacitively coupled to a gate electrode. The Josephson junction is made up of two superconducting electrodes, one of which is called the island and the other is called the electron reservoir. These two electrodes are connected with an insulating layer, i.e. the tunnel junction. A JJCQ is a device that harnesses the notable Josephson effect of superconductivity, which emerges at very low temperatures, as low as 50 mK or less. At such low temperatures, certain metals become superconductors. In their superconducting state, the interactions between electrons become important, causing the electrons of a metal to pair up. Each such an electron pair is called a Cooper pair, which is responsible for carrying superconducting cnrrent. The Josephson effect occurs due to a coherent quantum mechanical tunneling of Cooper pairs through the insulating layer, i.e. from superconducting electron reservoir to the superconducting island. The coupling energy involved in this process is the Josephson energy E_J, with associated tunnel junction capacitance C_J. The control gate voltage is coupled to the system through

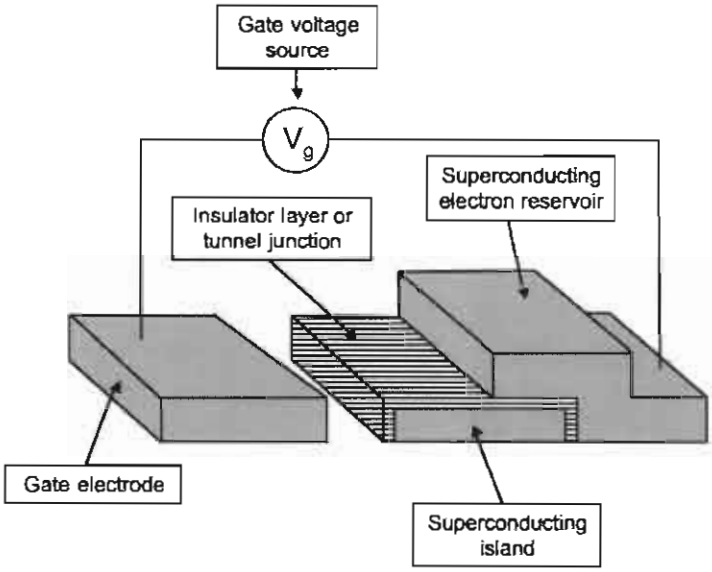

Figure 3.1: Components of a Josephson junction charge qubit in its simplest design form.

a gate capacitor C_g. The current technological advances allow a routine fabrication of very low junction capacitance, as low as femtofarad, and the value of gate capacitance can even be lower [68]. The corresponding single-electron charging energy $E_C \equiv e^2/2(C_J + C_g)$ is abont 1 K or higher. The Josephson energy E_J depends on the tunneling current and is typically on the order of 100 mK.

The following Hamiltonian describes a JJCQ device [68]

$$\hat{\mathcal{H}} = 4E_C(n - n_g)^2 - E_J \cos\Theta \tag{3.2}$$

where n represents a number operator of excess Cooper pairs in the island and Θ represents the phase of the superconducting order parameter of the island. The dimensionless gate charge $n_g \equiv C_g V_g/2e$ is used as a control parameter via externally controlling the gate voltage V_g. When the charging energy is very large as compared to the Josephson energy, i.e. $E_C \gg E_J$, the charge states form a basis and thus the Hamiltonian of equation (3.2) can be written in terms of the number of Cooper pairs n in the island [68]

$$\hat{\mathcal{H}} = \sum_n 4E_C(n - n_g)^2|n\rangle\langle n| - \frac{1}{2}E_J(|n\rangle\langle n+1| + |n+1\rangle\langle n|) \tag{3.3}$$

By tuning the gate voltage V_g to obtain a gate charge n_g of approximately a half-integer [68], only two charge states with $n = 0$ and $n = 1$ can be well-separated from the higher states. In what follows, the Hamiltonian of the JJCQ device simplifies to a qubit Hamiltonian

$$\hat{\mathcal{H}} = -\frac{1}{2}B_z\hat{\sigma}_z - \frac{1}{2}B_x\hat{\sigma}_x \tag{3.4}$$

where $B_z \equiv 4E_C(n-n_g)^2$ and $B_x \equiv E_J$. The charge states $n = 0$ and $n = 1$ now correspond to $|0\rangle$ and $|1\rangle$ basis states in spin-$\frac{1}{2}$ notation.

Here a typical JJCQ set-up is reviewed in its simplest design form. More detailed discussions and more sophisticated designs of JJCQs can be found, for example, in the recent review [68]. The study presented in this chapter is based on a particular JJCQ QC proposal [69]. While a single charge qnbit set-np in this proposal is of a very sophisticated design, the form of a single qubit Hamiltonian is the same as the one given by equation (3.4). An advantage of this particular QC architecture is that any charge qubit in a circuit (which consists of many qubits) can be effectively coupled through a common superconducting inductance [69]. This qubit-qubit coupling is represented by an Ising-type interactions $\hat{\sigma}_x^i\hat{\sigma}_x^j$ for $i \neq j$ where indices i and j label two arbitrary qubits in a circuit.

3.2.2 Two-qubit register and CNOT gate

Qubits, the building blocks of a QC, are two–level quantum systems, customarily represeuted by Pauli spin operators, $\hat{\sigma} = (\hat{\sigma}_x, \hat{\sigma}_y, \hat{\sigma}_z)$. The two eigenstates of $\hat{\sigma}_z$, with the convention chosen here, $|0\rangle \equiv |\uparrow\rangle$ (eigenvalue 1) and $|1\rangle \equiv |\downarrow\rangle$ (eigenvalue -1), constitute the standard basis, i.e. $\{|0\rangle, |1\rangle\}$, by means of which a state of a qubit and gate operations used to manipulate qubit states are defined.

An arbitrary pure state of a qubit can be written as

$$|\psi\rangle = e^{i\varsigma}\left(\cos\frac{\theta}{2}|0\rangle + e^{i\phi}\sin\frac{\theta}{2}|1\rangle\right), \tag{3.5}$$

where the real numbers $0 \leq \theta \leq \pi$ and $0 \leq \phi \leq 2\pi$ define a point on the surface of a unit

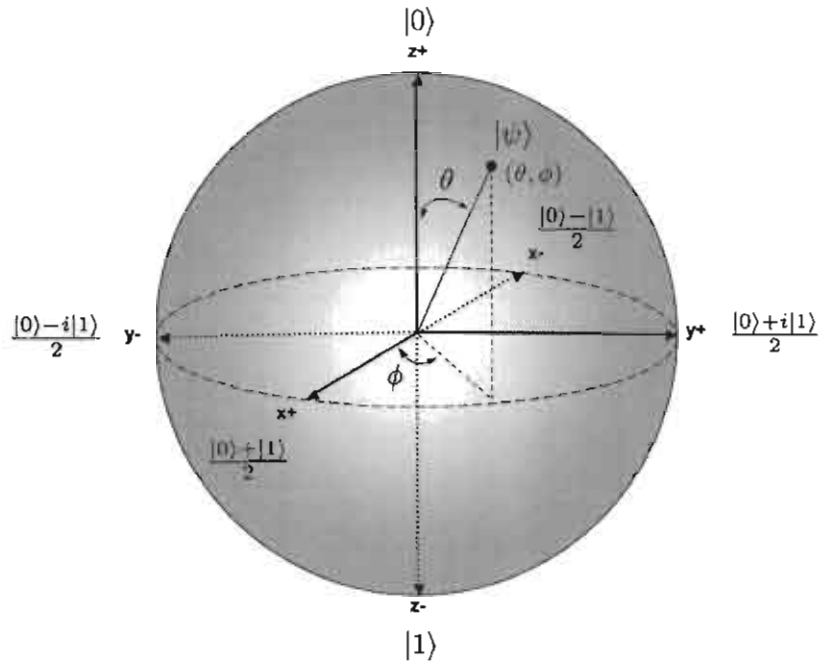

Figure 3.2: Geometric representation of a qubit state $|\psi\rangle$ on the Bloch sphere. An arbitrary pure state on the Bloch sphere is represented by a pair (θ, ϕ) of real numbers. The eigenstates of $\hat{\sigma}_z$, i.e. $|0\rangle$ and $|1\rangle$ with $(0, \phi)$ and (π, ϕ) are located at the north and south poles of the sphere. $(\pi/2, \phi)$ represent the points at equator that denote the states of the form $(|0\rangle + e^{i\phi}|1\rangle)/\sqrt{2}$. The points $(\pi/2, 0)$ and $(\pi/2, \pi)$ correspond to the eigenstates of $\hat{\sigma}_x$, i.e. $(|0\rangle + |1\rangle)/\sqrt{2}$ and $(|0\rangle - |1\rangle)/\sqrt{2}$. The two pairs $(\pi/2, \pi/2)$ and $(\pi/2, 3\pi/2)$ represent the eigenstates of $\hat{\sigma}_y$, i.e. $(|0\rangle + i|1\rangle)/\sqrt{2}$ and $(|0\rangle - i|1\rangle)/\sqrt{2}$.

sphere, i.e. the Bloch sphere. In figure 3.2, the geometrical representation of an arbitrary qubit state $|\psi\rangle$ as a point on the Bloch sphere is presented. The real number ζ appearing in equation (3.5) defines a global phase which has no observable consequence. Thus, qubit states with arbitrary values of ζ have the same representation on the Bloch sphere, which leads to the canonical representation of qubit states with the help of only two real parameters θ and ϕ:

$$|\psi\rangle = \cos\frac{\theta}{2}|0\rangle + e^{i\phi}\sin\frac{\theta}{2}|1\rangle \tag{3.6}$$

Arbitrary logic operations for universal quantum computation can be performed by a combination of one– and two–qubit gates [55-57]. Here, the focus is on one of the important

gates of quantum compntation, namely, the CNOT gate. Barenco *et al.* [57] showed that a set of gates including all one–qubit gates and a CNOT gate is universal, meaning that an arbitrary quantum algorithm can be obtained as a combination of one-qubit gates and a CNOT gate.

The CNOT gate is a two-qubit gate whose action is to flip the second qubit only if the first qubit is in state $|1\rangle$, i.e.

$$\begin{aligned} \hat{U}_{\text{CNOT}} |00\rangle &= |00\rangle \\ \hat{U}_{\text{CNOT}} |01\rangle &= |01\rangle \\ \hat{U}_{\text{CNOT}} |10\rangle &= |11\rangle \\ \hat{U}_{\text{CNOT}} |11\rangle &= |10\rangle. \end{aligned} \tag{3.7}$$

In the standard basis states for two qubits, i.e. $\{|00\rangle, |01\rangle, |10\rangle, |11\rangle\}$, the matrix representation of the CNOT gate is

$$\hat{U}_{\text{CNOT}} = |00\rangle\langle 00| + |01\rangle\langle 01| + |10\rangle\langle 11| + |11\rangle\langle 10|. \tag{3.8}$$

For a particular QC architecture there may not be a unique or one–step implementation of the CNOT gate. However, the CNOT gate can be implemented by a combination of elementary one and two-qubit subgates or rotations. The following protocol is one example to implement the CNOT gate [69],

$$\hat{U}_{\text{CNOT}} = \hat{\mathcal{Y}}^{\dagger}_{(2)}(\pi/2)\hat{\mathcal{H}}^{\dagger}_{(1)}(\pi/\sqrt{2})\hat{\mathcal{H}}^{\dagger}_{(2)}(\pi/\sqrt{2})\hat{U}_{CP}(\pi/4)\hat{\mathcal{H}}_{(1)}(\pi/\sqrt{2})\hat{\mathcal{H}}_{(2)}(\pi/\sqrt{2})\hat{\mathcal{Y}}_{(2)}(\pi/2) \tag{3.9}$$

Here, the subscripts 1- and 2- indicate the qubit on which the subgates operate. $\hat{U}_{CP}$ is a two-qubit gate that operates on two qubits. The subgates comprising the CNOT protocol operate right–to–left. The CNOT protocol is composed of three different subgates which are explained below.

The subgate $\hat{\mathcal{Y}}_{(2)}(\alpha = \pi/2)$, where α is the rotation angle, is a one-qubit $\pi/2$–rotation on the second qubit in the y-direction. This rotation is generated by a combination of x-

and z-rotations, i.e.

$$\hat{\mathcal{Y}}_{(2)}(\pi/2) = \hat{R}^{z\dagger}_{(2)}(\pi/2)\hat{R}^{x}_{(2)}(\pi/2)\hat{R}^{z}_{(2)}(\pi/2), \tag{3.10}$$

where one-qubit rotations in x– and z–directions take the following form for an arbitrary rotation angle α,

$$\hat{R}^{x/z}_{(i)}(\alpha) = \exp\left(\frac{i\alpha}{2}\hat{\sigma}^{(i)}_{x/z}\right). \tag{3.11}$$

Here, x/z means x or z and i is the index labeling the qubit. The z–rotation, when applied on the one-qubit standard basis states, i.e. $\{|0\rangle, |1\rangle\}$, induces a phase change proportional to the angle of rotation, α. For example, the angle $\alpha = \pi/2$ leads to

$$\hat{R}^{z}(\pi/2)|0\rangle = e^{i\frac{\pi}{4}}|0\rangle \quad \text{and} \quad \hat{R}^{z}(\pi/2)|1\rangle = e^{-i\frac{\pi}{4}}|1\rangle. \tag{3.12}$$

The one-qubit x–rotation with the angle $\alpha = \pi/2$ gives

$$\hat{R}^{x}(\pi/2)|0\rangle = \frac{1}{\sqrt{2}}(|0\rangle + i|1\rangle) \quad \text{and} \quad \hat{R}^{x}(\pi/2)|1\rangle = \frac{1}{\sqrt{2}}(|1\rangle + i|0\rangle). \tag{3.13}$$

The actions of z- and x-rotations on an arbitrary quantum state on the Bloch sphere are depicted in figure 3.3.

The Hadamard gates $\hat{\mathcal{H}}_{(i)}(\beta = \pi/\sqrt{2})$ for $i = 1, 2$, where β is the rotation angle, involve the first and the second qubits. A Hadamard gate can be obtained by simultaneously switching one–qubit control parameters in x- and z-directions, i.e.

$$\hat{\mathcal{H}}_{(i)}(\pi/\sqrt{2}) = \exp\left(i\frac{\pi}{\sqrt{2}}\frac{\hat{\sigma}^{(i)}_{x} + \hat{\sigma}^{(i)}_{z}}{2}\right). \tag{3.14}$$

The Hadamard gate transforms the standard basis states as

$$\hat{\mathcal{H}}(\pi/\sqrt{2})|0\rangle = \frac{e^{i\frac{\pi}{2}}}{\sqrt{2}}(|0\rangle + |1\rangle) \quad \text{and} \quad \hat{\mathcal{H}}(\pi/\sqrt{2})|1\rangle = \frac{e^{i\frac{\pi}{2}}}{\sqrt{2}}(|0\rangle - |1\rangle). \tag{3.15}$$

Finally, the two-qubit controlled–phase shift gate $\hat{U}_{CP}(\gamma = \pi/4)$, where γ is the rotation angle, is given by

$$\hat{U}_{CP}(\pi/4) = \exp\left(i\frac{\pi}{4}\left(-\hat{\sigma}^{(1)}_{x} - \hat{\sigma}^{(2)}_{x} + \hat{\sigma}^{(1)}_{x}\hat{\sigma}^{(2)}_{x}\right)\right). \tag{3.16}$$

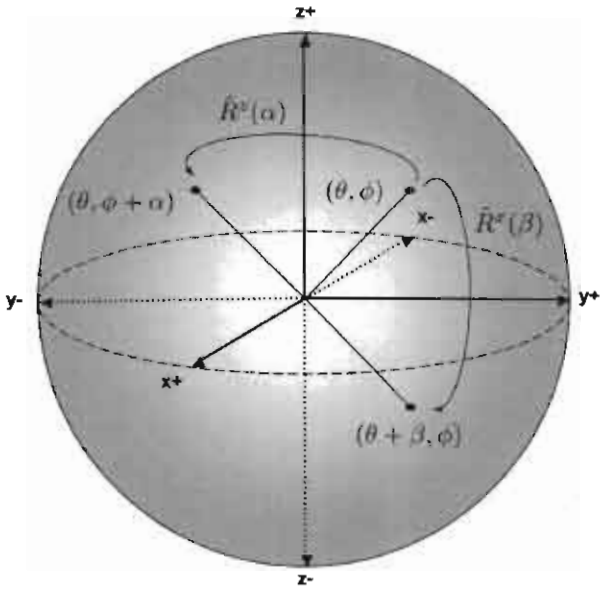

Figure 3.3: The actions of two rotation operators $\hat{R}_z(\alpha)$ and $\hat{R}_x(\beta)$ on an arbitrary state $|\psi\rangle$ are illustrated on the Bloch sphere. The z-rotation $\hat{R}_z(\alpha)$ transforms the state $|\psi\rangle$ with (θ, ϕ) to a new state $|\psi'\rangle$ with $(\theta, \phi + \alpha)$ by rotating it about the z-axis with an angle α. The x-rotation $\hat{R}_x(\beta)$ transforms the same state $|\psi\rangle$ to a new state $|\psi''\rangle$ with $(\theta + \beta, \phi)$ by a rotation about the x-axis with angle β.

The operation of the $\hat{U}_{CP}(\pi/4)$ gate can be better illustrated with the help of the following two-qubit basis states, i.e. $\{|++\rangle, |+-\rangle, |-+\rangle, |--\rangle\}$, where $|+\rangle = (|0\rangle + |1\rangle)/\sqrt{2}$ and $|-\rangle = (|0\rangle - |1\rangle)/\sqrt{2}$,

$$\begin{aligned}
\hat{U}_{CP}(\pi/4)\,|++\rangle &= \quad |++\rangle \\
\hat{U}_{CP}(\pi/4)\,|+-\rangle &= \quad |+-\rangle \\
\hat{U}_{CP}(\pi/4)\,|-+\rangle &= \quad |-+\rangle \\
\hat{U}_{CP}(\pi/4)\,|--\rangle &= -|--\rangle. \qquad (3.17)
\end{aligned}$$

For the time-dependent implementation of the CNOT protocol, the following control Hamiltonian [69] is employed,

$$\hat{H}_S(t) = -\frac{1}{2}\sum_{i=1}^{2}(\mathcal{B}_i^x(t)\hat{\sigma}_x^{(i)} + \mathcal{B}_i^z(t)\hat{\sigma}_z^{(i)}) + \mathcal{J}_x(t)\hat{\sigma}_x^{(1)}\hat{\sigma}_x^{(2)}. \qquad (3.18)$$

Table 3.1: Switching times and active Hamiltonians used to implement the CNOT gate.

Switching Intervals	Active Hamiltonian
$[t_0 = 0, t_1 = \pi/(2\mathcal{B}^z)]$	$-\frac{1}{2}\mathcal{B}^z\hat{\sigma}_z^{(2)}$
$[t_1, t_2 = t_1 + \pi/(2\mathcal{B}^x)]$	$-\frac{1}{2}\mathcal{B}^x\hat{\sigma}_x^{(2)}$
$[t_2, t_3 = t_2 + \pi/(2\mathcal{B}^z)]$	$+\frac{1}{2}\mathcal{B}^z\hat{\sigma}_z^{(2)}$
$[t_3, t_4 = t_3 + \sqrt{2}\pi/(2\mathcal{B}^z)]$	$-\frac{1}{2}\mathcal{B}^z\sum_{i=1}^{2}(\hat{\sigma}_z^{(i)} + \hat{\sigma}_x^{(i)})$
$[t_4, t_5 = t_4 + \pi/(4\mathcal{J}_x)]$	$\mathcal{J}_x(-\hat{\sigma}_x^{(1)} - \hat{\sigma}_x^{(2)} + \hat{\sigma}_x^{(1)}\hat{\sigma}_x^{(2)})$
$[t_5, t_6 = t_5 + \sqrt{2}\pi/(2\mathcal{B}^z)]$	$+\frac{1}{2}\mathcal{B}^z\sum_{i=1}^{2}(\hat{\sigma}_z^{(i)} + \hat{\sigma}_x^{(i)})$
$[t_6, t_7 = t_6 + \pi/(2\mathcal{B}^z)]$	$-\frac{1}{2}\mathcal{B}^z\hat{\sigma}_z^{(2)}$
$[t_7, t_8 = t_7 + \pi/(2\mathcal{B}^x)]$	$+\frac{1}{2}\mathcal{B}^x\hat{\sigma}_x^{(2)}$
$[t_8, t_9 = t_8 + \pi/(2\mathcal{B}^z)]$	$+\frac{1}{2}\mathcal{B}^z\hat{\sigma}_z^{(2)}$

Here, $\mathcal{B}_i^x(t)$, $\mathcal{B}_i^z(t)$ and $\mathcal{J}_x(t)$ are time–dependent control parameters used to generate elementary gate operations. Detailed discussions on how to generate one– and two–qubit gates experimentally from (3.18) by external manipulations of the control parameters can be found in [69]. The Hamiltonian (3.18) is the basis of a Josephson charge-qubit QC proposal [69], which allows a scalable design wherein any two qubits of the QC can be effectively coupled. In addition, the Hamiltonian (3.18) requires only one two-qubit operation to implement a CNOT gate.

The experimental manipulations [69] required to generate the control Hamiltonians (3.18) can induce a potential source of error. A number of simplifying assumptions regarding the implementation of the CNOT gate are needed in order to concentrate on errors that emerge from the system-environment interactions. In particular, full control over the dynamics of the CNOT gate is assumed, i.e. the effects of faulty switching, imperfections

and possible residual interactions induced by noisy fields that can cause fluctuations in control parameters of the two qubit register and so forth are neglected. It is also assumed that the CNOT gate can be propagated by using perfect square pulses [83], which however can only be approximately implemented experimentally. Moreover, a free Hamiltonian evolution is not allowed. Hence, it is assumed that consecutive gates comprising the CNOT protocol can be simultaneously switched on and off. In other words, the field strengths experienced by qubits can be switched on and off instantaneously via

$$\mathcal{B}_i^{x/z}(t) = \mathcal{B}_i^{x/z}[\Theta(t - t_{\rm on}) - \Theta(t - t_{\rm off})] \tag{3.19}$$

for $i = 1, 2$ and similarly,

$$\mathcal{J}_x(t) = \mathcal{J}_x[\Theta(t - t_{\rm on}) - \Theta(t - t_{\rm off})]. \tag{3.20}$$

Here, $\mathcal{B}_i^{x/z}(t)$ and $\mathcal{J}_x(t)$ are constant in the time interval, $[t_{\rm on}, t_{\rm off}]$. It follows that the relation between the actual propagation times and the rotation angles α, β, and γ defined in equations (3.11), (3.14), and (3.16) are given by $\alpha = \mathcal{B}^{x/z}t$ for the y-rotation $\hat{\mathcal{Y}}$, $\beta = \mathcal{B}^{x/z}t$ for the Hadamard gates $\hat{\mathcal{H}}$, and $\gamma = \mathcal{J}_x t$ for the controlled phase-shift gate, $\hat{U}_{CP}$. Since the Hadamard gates on the first and second qubits commute, they are implemented together. Hence, the full implementation of the CNOT gate is achieved in nine steps, which consist of the Schrödinger evolutions in time intervals, $[t_i, t_{i+1}]$ for $i = 0, .., 8$. The switching times for the components of the CNOT gate, and the corresponding active Hamiltonian in each time interval, are summarized in table 3.1. The unitary operator governing the CNOT gate now takes the following time-dependent form

$$\begin{aligned} \hat{U}_{\rm CNOT}(t_9, t_0) &= \hat{U}(t_9, t_8)\hat{U}(t_8, t_7)\hat{U}(t_7, t_6)\hat{U}(t_6, t_5)\hat{U}(t_5, t_4) \\ &\times \hat{U}(t_4, t_3)\hat{U}(t_3, t_2)\hat{U}(t_2, t_1)\hat{U}(t_1, t_0). \end{aligned} \tag{3.21}$$

In the absence of system-environment interactions, the coherent time evolution of two qubits under the action of the CNOT gate is given by

$$\hat{\rho}_S^{ideal}(t) = \hat{U}_{\rm CNOT}(t_9, t_0)\hat{\rho}_S(0)\hat{U}_{\rm CNOT}^{\dagger}(t_9, t_0). \tag{3.22}$$

where $\hat{\rho}_S^{ideal}(t)$ is the time-evolved density operator of two qubits and $\hat{\rho}_S(0)$ is the initial or input state of two qubits.

In figure 3.4, the coherent time evolution of $\hat{\rho}_S^{ideal}(t)$ is shown for the initial standard basis states $\{|00\rangle, |01\rangle, |10\rangle, |11\rangle\}$. Figure 3.4 comprises four subfigures. In each subfigure, one of the diagonal matrix elements of $\hat{\rho}_S^{ideal}(t)$ is plotted as a function of time for four different input states. Specifically, the matrix element $\rho_{00}(t) = \langle 00|\hat{\rho}_S^{ideal}(t)|00\rangle$ is plotted in subfigure 3.4(a), $\rho_{01}(t) = \langle 01|\hat{\rho}_S^{ideal}(t)|01\rangle$ in 3.4(b), $\rho_{10}(t) = \langle 10|\hat{\rho}_S^{ideal}(t)|10\rangle$ in 3.4(c), and $\rho_{11}(t) = \langle 11|\hat{\rho}_S^{ideal}(t)|11\rangle$ in 3.4(d). To distinguish between the input states, each input state is plotted with a different colored line. The input state $|00\rangle$ is plotted with black, $|01\rangle$ with green, $|10\rangle$ with red, and $|11\rangle$ with dashed blue lines.

Consider the transformations on the input state $|00\rangle$ under the CNOT dynamics by following the black dashed lines in figure 3.4. Recall that the first three subgates, i.e. $\hat{U}(t_1, t_0)$, $\hat{U}(t_2, t_1)$, and $\hat{U}(t_3, t_2)$ act on the second qubit. At time $t_0 = 0$, the initial populations are $\rho_{00} = 1$ and $\rho_{01} = \rho_{10} = \rho_{11} = 0$. The first subgate $\hat{U}(t_1, t_0)$ is a $\pi/2$-rotation in the z-direction, the effect of which is a phase change only with no observable consequence on the populations. The second subgate $\hat{U}(t_2, t_1)$ is $\pi/2$-rotation in the x-direction, which changes the populations of the second qubit. As a results, at time t_2 the diagonals take the values $\rho_{00} = \rho_{01} = 0.5$ while the values $\rho_{10} = \rho_{11} = 0$ do not change. These values of the populations indicate an equal probability superposition of $|00\rangle$ and $|01\rangle$. The third subgate $\hat{U}(t_3, t_2)$ is again a z-rotation and results in no observable change in the populations. In the time interval (t_4, t_3), the Hadamard gates are applied on both qubits and give the populations $\rho_{01} = \rho_{11} = 0.5$, $\rho_{00} = \rho_{10} = 0$ at time t_4. These populations indicate an equal probability superposition of $|01\rangle$ and $|11\rangle$. The next gate applied in the interval (t_5, t_4) is the controlled-phase shift gate, which gives an equal probability superposition of $|01\rangle$ and $|10\rangle$ at time t_5 with the value of populations $\rho_{01} = \rho_{10} = 0.5$, $\rho_{00} = \rho_{11} = 0$. In the interval (t_6, t_5), the two Hadamard gates are applied on both qubits. These Hadamard

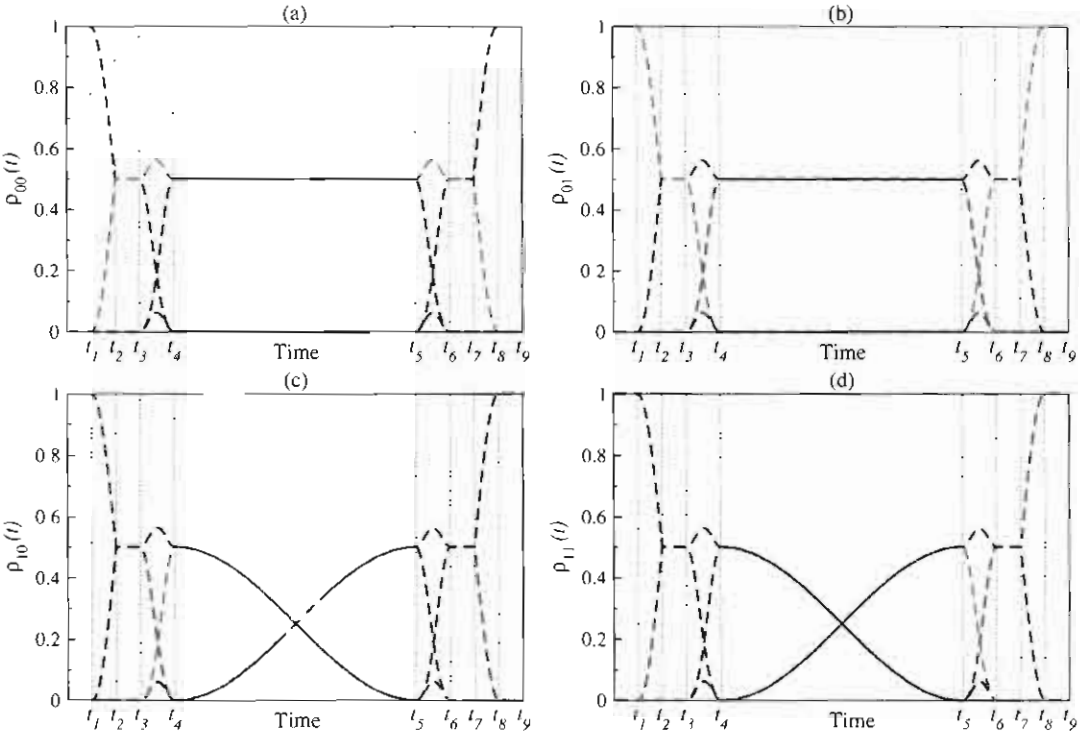

Figure 3.4: The coherent time-resolved dynamics of the CNOT gate is depicted by diagonal matrix elements (i.e. populations) of density operator $\hat{\rho}_S^{ideal}(t)$. The diagonal matrix element $\rho_{00}(t) = \langle 00|\hat{\rho}_S^{ideal}(t)|00\rangle$ is plotted in subfigure (a), $\rho_{01}(t) = \langle 01|\hat{\rho}_S^{ideal}(t)|01\rangle$ in (b), $\rho_{10}(t) = \langle 10|\hat{\rho}_S^{ideal}(t)|10\rangle$ in (c), and $\rho_{11}(t) = \langle 11|\hat{\rho}_S^{ideal}(t)|11\rangle$ in (d). In each subfigure, the input state $|00\rangle$ is plotted with black, $|01\rangle$ with green, $|10\rangle$ with red, and $|11\rangle$ with dashed blue lines. The CNOT dynamics is obtained for the following values of control parameters $\mathcal{B}^{x/z} = 1\ \epsilon$ and $\mathcal{J}^{x/z} = 0.05\ \epsilon$ where ϵ is an arbitrary unit. The time is in units of $\hbar/\epsilon$.

gates are the inverses of the Hadamard gates applied in the interval (t_4, t_3) and give an equal probability superposition of $|00\rangle$ and $|01\rangle$ at time t_6 with populations $\rho_{00} = \rho_{01} = 0.5$, $\rho_{10} = \rho_{11} = 0$. The last three subgates, i.e. $\hat{U}(t_9, t_8)$, $\hat{U}(t_8, t_7)$ and $\hat{U}(t_7, t_6)$ are the inverse transformations of the first three subgates, which restore the populations to their initial values $\rho_{00} = 1$ and $\rho_{01} = \rho_{10} = \rho_{11} = 0$ at $t_9 = 0$. Hence, overall the CNOT gate acts like an identity operator on the input state $|00\rangle$.

The CNOT subgates cause similar transformations as explained above when applied to the other input states, i.e. $|01\rangle$, $|10\rangle$, $|11\rangle$. The overall transformations induced by the

CNOT gate are as follows. For the input state $|01\rangle$, plotted with dashed green lines, the initial populations, i.e. $\rho_{01} = 1$ and $\rho_{00} = \rho_{10} = \rho_{11} = 0$ at time $t_0 = 0$ are the same as the final populations at time t_9. Overall, the CNOT gate acts like an identity operator on the state $|01\rangle$. For the input states $|10\rangle$ and $|11\rangle$ the effect of the CNOT gate is not trivial. For the input state $|10\rangle$, plotted with red dashed lines, the initial populations are $\rho_{10} = 1$ and $\rho_{00} = \rho_{01} = \rho_{11} = 0$, but the final populations are $\rho_{11} = 1$ and $\rho_{00} = \rho_{01} = \rho_{10} = 0$. Hence, the CNOT gate transforms the input state $|10\rangle$ into the output state $|11\rangle$. Similarly, for the input state $|11\rangle$, plotted with blue dashed lines, while the initial populations are $\rho_{11} = 1$ and $\rho_{00} = \rho_{01} = \rho_{10} = 0$, the final populations are $\rho_{10} = 1$ and $\rho_{00} = \rho_{01} = \rho_{11} = 0$. The CNOT gate thus causes the transformation $|11\rangle \rightarrow |10\rangle$.

3.2.3 Residual interactions

In this section, the error generators, i.e. system-environment interaction operators, are defined. Two different types of errors [83] will be investigated; the bit–flip errors are generated by an xx-type coupling operator, i.e.

$$\hat{S}\hat{B} = (\hat{\sigma}_x^{(1)} + \hat{\sigma}_x^{(2)})\hat{\Sigma}_x \quad \text{and} \quad \hat{\Sigma}_x = \sum_{i=3}^{N+2} \lambda_i \hat{\sigma}_x^{(i)}, \tag{3.23}$$

whereas the phase–errors are generated by a zz-type coupling operator, i.e.

$$\hat{S}\hat{B} = (\hat{\sigma}_z^{(1)} + \hat{\sigma}_z^{(2)})\hat{\Sigma}_z \quad \text{and} \quad \hat{\Sigma}_z = \sum_{i=3}^{N+2} \lambda_i \hat{\sigma}_z^{(i)}. \tag{3.24}$$

In both cases, the interaction strength λ is randomly and uniformly sampled within $[-\lambda, \lambda]$ where λ is equal, in magnitude, to $\mathcal{J}_x$ which is the experimentally relevant two-qubit coupling strength.

Although solid and condensed phase QC proposals inherit a variety of physical interactions to couple qubits, and accordingly qubit-qubit residual interactions of xx-, zz-, yy-, or xy-type are all possible error generators, only xx-type residual interactions are expected for the Josephson charge-qubit QC proposal [69] under investigation. This is due to the fact

that two-qubit gates for this design are generated by the xx-type qubit-qubit interactions. However, it is noteworthy that different types of residual interactions may also be possible in the presence of impurities. Nevertheless, consideration of the second type of coupling, i.e. zz-type interactions will help improve the understanding of the open system dynamical effects.

3.2.4 Environment Hamiltonian

It is assumed that the imperfections arising in the QC core can be modeled via a combination of one– and two–qubit interactions [72, 73], although higher order interactions may also be possible [84]. The control Hamiltonian of the two-qubit register, i.e. equation (3.18), suggests that the bath Hamiltonian for N-idle bath qubits should be of the form,

$$\hat{H}_B = -\frac{1}{2}\sum_{i=3}^{N+2}\left(B_i^z\hat{\sigma}_z^{(i)} + B_i^x\hat{\sigma}_x^{(i)}\right) + \sum_{i=3}^{N+1}\sum_{j=i+1}^{N+2} J_x^{i,j}\hat{\sigma}_x^{(i)}\hat{\sigma}_x^{(j)}, \tag{3.25}$$

which can also be considered as an effective Hamiltonian representing the collective dynamics of the rest of the QC. Similar Hamiltonians are also widely used as a generic model of an isolated QC in the presence of static internal imperfections [72-77].

One–body static imperfections in the Hamiltonians of the bath qubits are modeled randomly and uniformly by sampling the coefficients $B_i^{x/z}$ from the interval,

$$B_i^{x/z} \in [B_0^{x/z} - \delta/2,\ B_0^{x/z} + \delta/2]. \tag{3.26}$$

The idle bath qubits should be similar to the active qubits. This is because they all belong to the same QC core. Thus, the average values of the distribution, $B_0^{x/z}$, represent the experimentally relevant qubit dynamics in the absence of imperfections. In other words, the idle bath qubits differ from the active qubits by a static noise characterized by a detuning parameter, δ. In modeling two-body residual interactions, i.e. system-bath and intra-bath interactions, the previous studies are followed [72-77]. These coupling coefficients are sampled randomly and uniformly from $J_x^{i,j} \in [-J_x,\ J_x]$ and $\lambda_i^{x/z} \in [-\lambda,\ \lambda]$. The same

set of λ_i values for both xx- and zz-type coupling is used so that the relative importance of these error generators can be understood. In previous studies [72-77], the QC core is assumed to be a two-dimensional lattice of qubits interacting via nearest-neighbor two-qubit interactions. While the same type of distribution for the qubit-qubit interactions is used here, all possible pairwise qubit interactions in the bath Hamiltonian (3.25) are also allowed. This is because the charge-qubit QC proposal [69] permits all pairwise qubit couplings in principle, and so residual interactions among all qubit pairs are likely to exist. Therefore, the use of all qubit-qubit interactions is expected to mimic short as well as long-range residual interactions. Nevertheless, the type of the distribution and allowed interactions used here should still be considered as an idealization because, for example, possible spatial dependencies of the imperfections due to the location of qubits in the QC are not explicitly taken into account. In an experiment the magnitude as well as type of the imperfection would possibly be intrinsic to the particular experimental condition and physical set-up. Nevertheless, to compensate for the idealization of the model developed here, a large number of parameters will be used in numerical simulations.

3.2.5 Initial states

It is assumed that initial state preparation for the subsystem is achieved before the actual dynamics of the CNOT gate is initiated. Moreover, it is assumed that the rest of the QC, i.e. the bath qubits, is already thermalized. Thus, the initial state of the whole system is given as a product state,

$$\hat{\rho}(0) = \hat{\rho}_S(0) \otimes \hat{\rho}_B(0), \tag{3.27}$$

where $\hat{\rho}_S(0)$ is the subsystem density and $\hat{\rho}_B(0)$ is the canonical bath density operator. At equilibrium the collective state of the thermalized qubits is of the canonical form,

$$\hat{\rho}_B(0) = (1/Q) \exp\left(-\hat{H}_B/kT\right) \tag{3.28}$$

with

$$Q = \mathrm{Tr}_B[\exp(-\hat{H}_B/kT)]. \tag{3.29}$$

These initial conditions are not easily achieved in practice, and thus are somewhat unrealistic since they do not take into account possible residual correlations between the system and bath degrees of freedom. However, inclusion of the effects of imperfect initial conditions would greatly complicate this study. Moreover, the aim is to observe the emergence of dynamical errors from the residual static internal interactions.

In simulations, two different sets of initial states for the two-qubit register will be considered. The first set includes four standard basis states for which the CNOT gate is defined

$$\hat{\rho}_S(0) = |\psi_0\rangle\langle\psi_0| \quad \text{where} \quad |\psi_0\rangle \in \{|00\rangle, |01\rangle, |10\rangle, |11\rangle\}, \tag{3.30}$$

and the second set consists of four Bell states defined as

$$\hat{\rho}_S(0) = |\psi_0\rangle\langle\psi_0| \quad \text{where} \quad |\psi_0\rangle \in \{(|00\rangle \pm |11\rangle)/\sqrt{2}, (|01\rangle \pm |10\rangle)/\sqrt{2}\}. \tag{3.31}$$

3.3 Exact numerical approach

Given the Hamiltonians and the initial conditions, the exact reduced density at some later time, t, can in principle be calculated by the formula,

$$\hat{\rho}_S(t) = \mathrm{Tr}_B[\hat{U}(t)\hat{\rho}(0)\hat{U}^\dagger(t)], \tag{3.32}$$

where

$$\hat{U}(t) = \hat{T}\exp\left\{-(i/\hbar)\int_0^t \hat{H}(t')dt'\right\}. \tag{3.33}$$

Equation (3.32) is valid for all temperatures. In the low temperature limit, the reduced density operator, $\hat{\rho}_S(t)$, is calculated via

$$\hat{\rho}_S(t) = \sum_{n=1}^{n_{eig}} \frac{e^{-E_n/kT}}{Q'} \mathrm{Tr}_B[\hat{U}(t)|\Psi_n(0)\rangle\langle\Psi_n(0)|\hat{U}^\dagger(t)] \tag{3.34}$$

for all initial states of the form, i.e. $|\Psi_n(0)\rangle = |\psi_0\rangle \otimes |\phi_n^B\rangle$. Here, the bath states, $|\phi_n^B\rangle$, are obtained by solving the bath eigenvalue equation for the lowest eigenvalues for N-idle bath qubits,

$$\hat{H}_B|\phi_n^B\rangle = E_n|\phi_n^B\rangle. \tag{3.35}$$

In what follows, by defining $|\Psi_n(t)\rangle = \hat{U}(t)(|\psi_0\rangle \otimes |\phi_n^B\rangle)$ for each bath state, n, the actual dynamics are obtained by solving the Schrödinger equation,

$$d|\Psi_n(t)\rangle/dt = -(i/\hbar)\hat{H}(t)|\Psi_n(t)\rangle. \tag{3.36}$$

Note that in equation (3.34) the thermal bath density (3.28) has been replaced with

$$\hat{\rho}_B(0) \simeq \sum_{n=1}^{n_{eig}} |\phi_n^B\rangle \frac{e^{-E_n/kT}}{Q'} \langle\phi_n^B|, \tag{3.37}$$

where the sum is now over the thermally populated bath states only. Thus, n_{eig} is set so that states $n_{eig}+1$ and higher are unoccupied, and the partition function is then of the form,

$$Q' = \sum_{n=1}^{n_{eig}} \exp\left(-E_n/kT\right). \tag{3.38}$$

3.3.1 Numerics and parameters

The numerical simulations are based on the experimentally realizable control parameters of the charge-qubit QC proposal [69]. For computational convenience, the parameters of the control Hamiltonian are scaled in units of $\epsilon = 200$ mK. The one- and two-qubit control parameters are as follows, $\mathcal{B}^x = \mathcal{B}^z = 1$, and $\mathcal{J}_x = 0.05$, respectively. Heuce, a typical switching time for the one-qubit gate operations is of order $\hbar/2\mathcal{B}^z \sim 0.1$ ns. The two-qubit gate span is however 10 times longer. The total elapsed time for the CNOT gate is then about $t_g = 1.129$ ns. The relevant temperature is 50 mK [68] and thus $kT = 0.25$. While achieving this low temperature, necessary for coherent quantum control, might be an experimental burden, it leads to a significant computational advantage for exact propagations since only

a few bath states will be populated at this low temperature. $n_{eig} = 20$ was sufficient in all the calculations. The other parameters that define the bath qubits are $B_0^x = B_0^z = 1$ and $\delta = 0.4$. A number of J_x values are considered in order to explore the emergence of chaos: $J_x = 0.05,\ 0.25,\ 0.50,\ 1.00,\ 2.00$. The subsystem-bath interaction strength is set equal to the two-qubit control parameter, and thus $\lambda = 0.05$ for both bit-flip and phase errors.

The exact diagonalization of the bath Hamiltonian (3.25) for $n_{eig} = 20$ eigenvalues is done by an implicitly restarted Lanczos algorithm [85] for $N = 10$ idle bath qubits. The Schrödinger equation for a given initial subsystem and bath state involves 2^{13} coupled real linear differential equations. The numerical integrations are performed by a variable-step size Runge–Kutta method [86] of order 8.

3.4 Error quantifiers: purity and fidelity

The quantity of primary interest is the redneed density of the active degrees of freedom, $\hat{\rho}_S(t)$, obtained by tracing out the degrees of freedom of the idle bath qnbits, i.e.

$$\hat{\rho}_S(t) = \mathrm{Tr}_B[\hat{\rho}(t)]. \tag{3.39}$$

The reduced density snpplies all necessary probabilistic information about the open dynamics of the CNOT gate. Hence, once the reduced density is known, the quality of gate implementation can readily be assessed by standard error quantifiers. Two error quantifiers are employed to assess the performance of the CNOT gate: purity and fidelity. Non-unitary internal errors due to decoherence and dissipation are quantified by using purity, since the purity is insensitive to nnitary effects. Fidelity reflects all sources of error. Hence, a large deviation between the purity and fidelity can be used as an indicator of unitary errors due to the coherent shifting process.

Gate purity, also known as linear entropy, is defined by the trace of the square of the

reduced density operator,

$$\mathcal{P}(t) = \mathrm{Tr}_S[\hat{\rho}_S^2(t)], \tag{3.40}$$

and it gives a measure of how close the reduced density stays to a pure state in the course of open system dynamics. The purity for pure states is unity and the purity for mixed states is less than unity.

Gate fidelity can be calculated from the reduced density using

$$\mathcal{F}(t) = \mathrm{Tr}_S[\hat{\rho}_S(t)\hat{\rho}_S^{ideal}(t)], \tag{3.41}$$

where $\hat{\rho}_S^{ideal}(t)$ is the time evolved density obtained in the absence of residual interactions with the idle qubits, given by equation (3.22). The ideal value of the fidelity for pure initial conditions would be unity at all times, i.e. $\mathcal{F}(t) = 1$ in the absence of interaction with the idle bath qubits.

3.4.1 Average error quantifiers

Exact numerical simulations, reported in the next chapter, involve a large number of QC configurations, i.e. initial conditions, system-bath interactions and bath parameters. In order to compress the data, average error quantifiers, i.e. the average purity and fidelity, are employed. For each of these error quantifiers, two averages are computed: over the four initial standard basis states (3.30), and over the four initial Bell states (3.31). The average purity is defined as

$$\bar{\mathcal{P}}(t) = \frac{1}{4}\sum_{|\psi_0\rangle} \mathrm{Tr}_S[\hat{\rho}_S^2(t)] \tag{3.42}$$

and the average fidelity as

$$\bar{\mathcal{F}}(t) = \frac{1}{4}\sum_{|\psi_0\rangle} \mathrm{Tr}_S[\hat{\rho}_S(t)\hat{\rho}_S^{ideal}(t)] \tag{3.43}$$

where the ideal time evolution is given by equation (3.22).

These average error quantifiers will not only allow the determination of the overall magnitude of errors for two sets of initial conditions and two different error generators, but also help estimate the overall performance of the chaotic Kraus decomposition for different QC configurations and also help present the results in a concise form.

Chapter 4

Simulations for the CNOT gate

In this chapter[§] the exact numerical results obtained in the simulations are reported for a large number of quantum computer (QC) configurations, specifically, two sets of total eight different initial system states (i.e. the standard basis states and Bell states), two types of error generators (i.e. bit-flip and phase errors), and five different values of intra-enviromental interactions. In section 4.1 the results are reported for average error quantifiers, i.e. the average purity and fidelity, and an overall performance of the CNOT gate for bit-flip and phase type error generators is estimated. In section 4.2 the time evolution of individual initial states is examined separately for the bit-flip and phase type error generators, and how different operations comprising the CNOT protocol affected by internal imperfections are determined. It is shown that in some cases particular operations are influenced much more strongly than others, and the magnitude of the errors does not neccessarily correlate with the duration of the operation. These results suggest that it may be possible to find a particular implementation of elementary gates that has a better performance than most.

[§]This chapter is based on two studies [16, 17] reported by Çetinbaş and Wilkie.

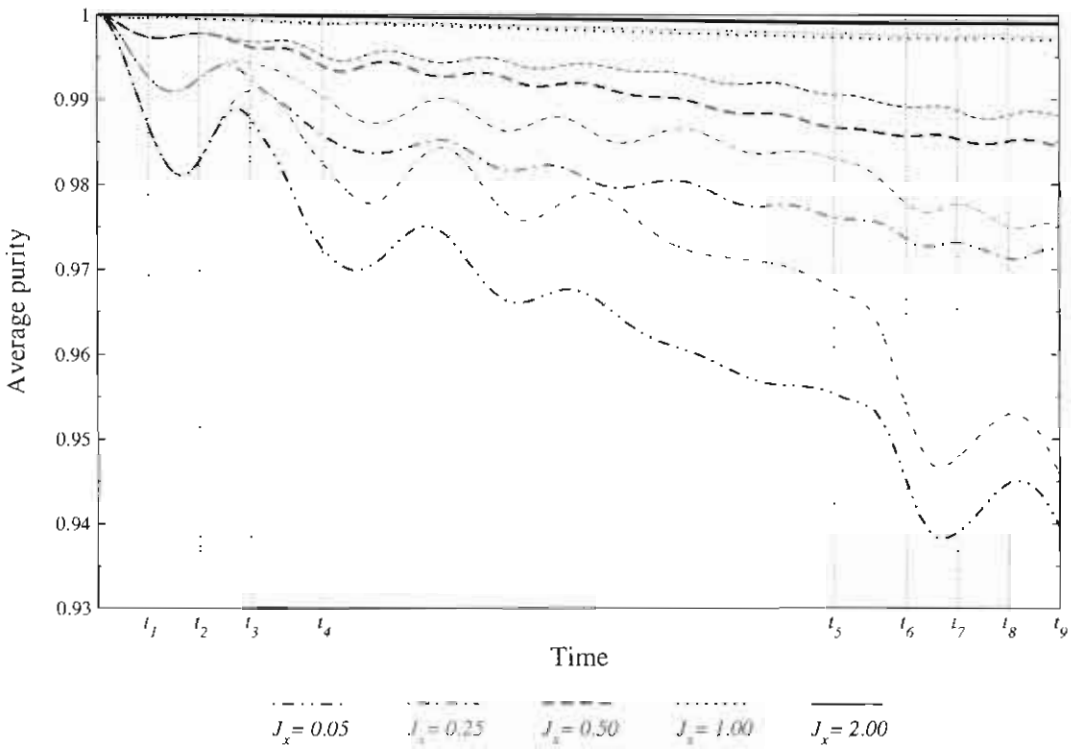

Figure 4.1: Time evolution of average purity, $\bar{\mathcal{P}}(t)$, for standard basis states (thin lines) and Bell states (thick lines) in the case of bit–flip errors (generated by xx-type coupling) plotted for five different values of intra-bath coupling, $J_x = 0.05, 0.25, 0.50, 1.00, 2.00$ ϵ.

4.1 Overall performance: standard basis states versus Bell states

In figure 4.1, the average purity, $\bar{\mathcal{P}}(t)$, versus time, and in figure 4.2, the average fidelity, $\bar{\mathcal{F}}(t)$, versus time is plotted for bit-flip errors generated by the xx-type interaction operator for five different values of intra-bath couplings, J_x. In figures 4.3 and 4.4, $\bar{\mathcal{P}}(t)$ and $\bar{\mathcal{F}}(t)$ are plotted for phase errors generated by the zz-type interaction operator. In all figures the Bell states are plotted with thick lines to distinguish them from the standard basis states.

Non-negligible deviations from the perfect purity, i.e. $\bar{\mathcal{P}}(t) = 1$, which are greater than the theoretically acceptable limit of 0.99999 [87], are observed in almost all cases, which indicates that internal decoherence exists and may be an issue of concern even for a

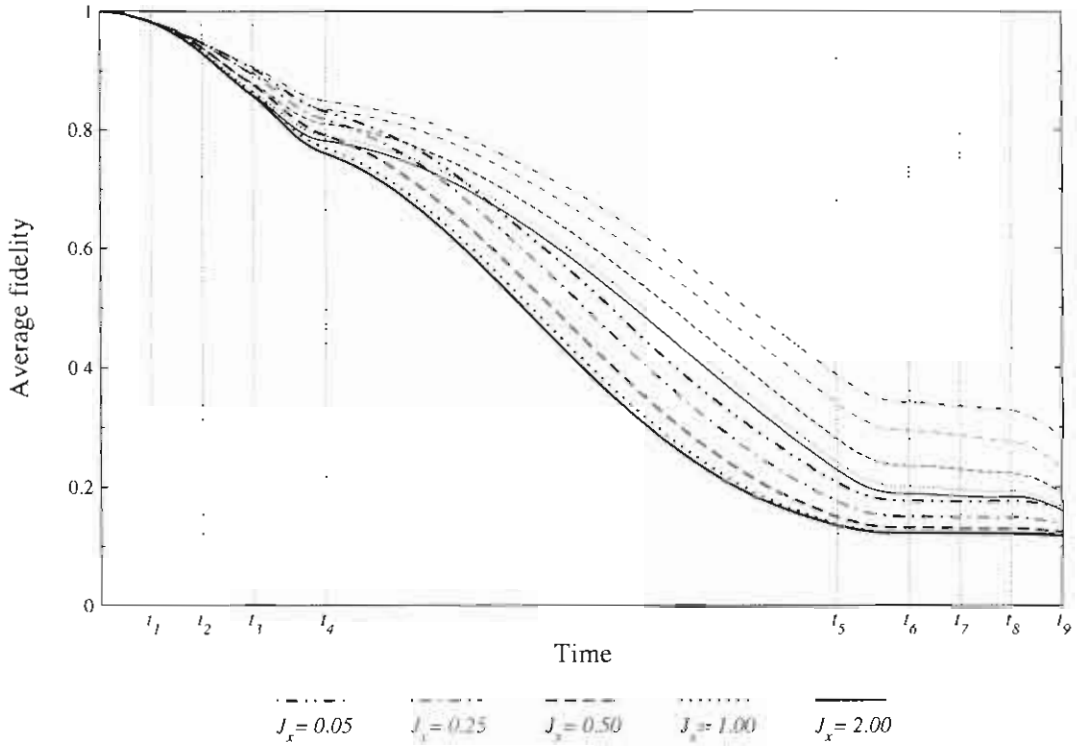

Figure 4.2: Time evolution of average fidelity, $\bar{\mathcal{F}}(t)$, for standard basis states (thin lines) and Bell states (thick lines) in the case of bit–flip errors (generated by xx-type coupling) plotted for five different values of intra-bath coupling, $J_x = 0.05, 0.25, 0.50, 1.00, 2.00\ \epsilon$.

relatively small number of bath qubits. However, with increasing J_x, a transition to chaos occurs, which in turn results in a rapid suppression of errors due to the decoherence. The confirmation of chaos is discussed in chapter 7. The results indicate that the bath is chaotic above $J_x > 0.15\ \epsilon$. The strongest intra–environmental coupling, $J_x = 2.00\ \epsilon$, leads to an almost complete suppression of decoherence. This is the case for bit-flip as well as phase errors. Hence, deliberately induced chaotic bath interactions can enhance the performance of a QC, and may even serve as an error correction strategy when such strong interactions are practical for a QC design. The results show that the Bell states are slightly more susceptible to the effects of internal imperfections than the standard basis states, and the bit-flip type errors are of the same magnitude as phase-errors for all initial conditions.

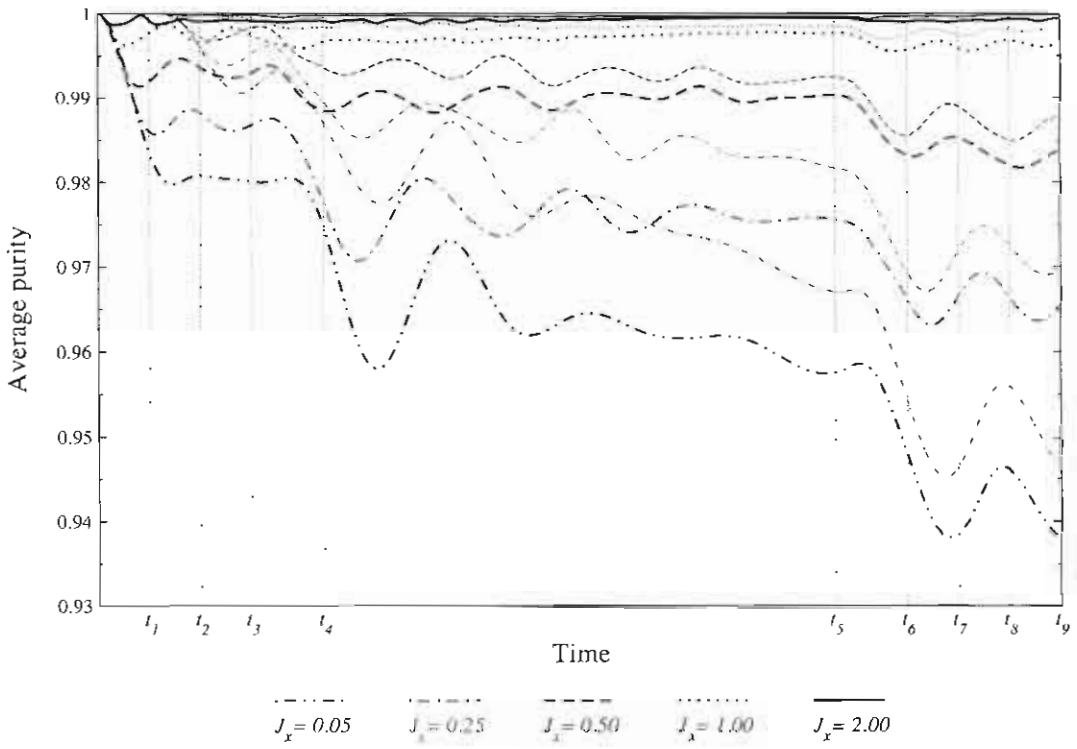

Figure 4.3: Time evolution of average purity, $\bar{\mathcal{P}}(t)$, for standard basis states (thin lines) and Bell states (thick lines) in the case of phase errors (generated by zz-type coupling) plotted for five different values of intra-bath coupling, $J_x = 0.05, 0.25, 0.50, 1.00, 2.00\ \epsilon$.

The fidelity plots display very large and unexpected deviations from ideality, i.e. $\bar{\mathcal{F}}(t) = 1$. However, the purity plots did not indicate such behavior. Since the purity is insensitive to unitary effects, the large deviations between the purity and fidelity plots indicate the presence of environment–induced large unitary errors in the CNOT dynamics. Increasing J_x results in an improvement in fidelity for phase errors. However, almost no-improvement is observed for bit-flip type errors. In fact, increasing J_x, slightly deteriorates the performance for xx-type interactions.

The results indicate that the surprisingly high magnitude unitary errors destroy the fidelity of QC operations, and error correction methods [79] need to operate in order to correct the dynamics. Here, the large errors are observed for the two-qubit subsystem

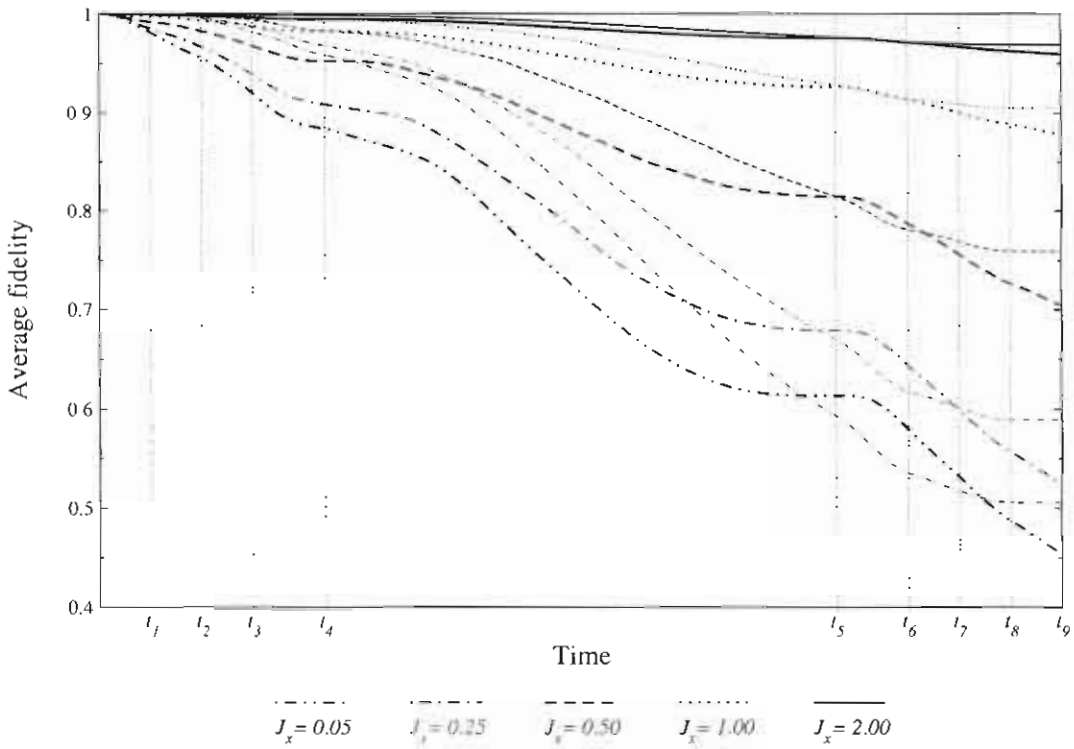

Figure 4.4: Time evolution of average fidelity, $\bar{\mathcal{F}}(t)$, for standard basis states (thin lines) and Bell states (thick lines) in the case of phase errors (generated by zz-type coupling) plotted for five different values of intra-bath coupling, $J_x = 0.05, 0.25, 0.50, 1.00, 2.00\ \epsilon$.

and these errors are common to the entire active part which in principle may comprise a large number of qubits. While existing error correction schemes [79] can be used to remove the undesirable errors induced by the coherent shift process, the number of single-qubit operations needed to correct these errors will be quite high, which in turn considerably increases the computational cost. However, since the errors induced by the coherent shift process are of unitary nature and thus deterministic, a much simpler error correction scheme may be possible.

Ten different realizations of the QC were explored. The results presented here are only for a single realization of the QC but these results are typical. However, some exceptional realizations were also encountered. In some cases the bath density of states increases with

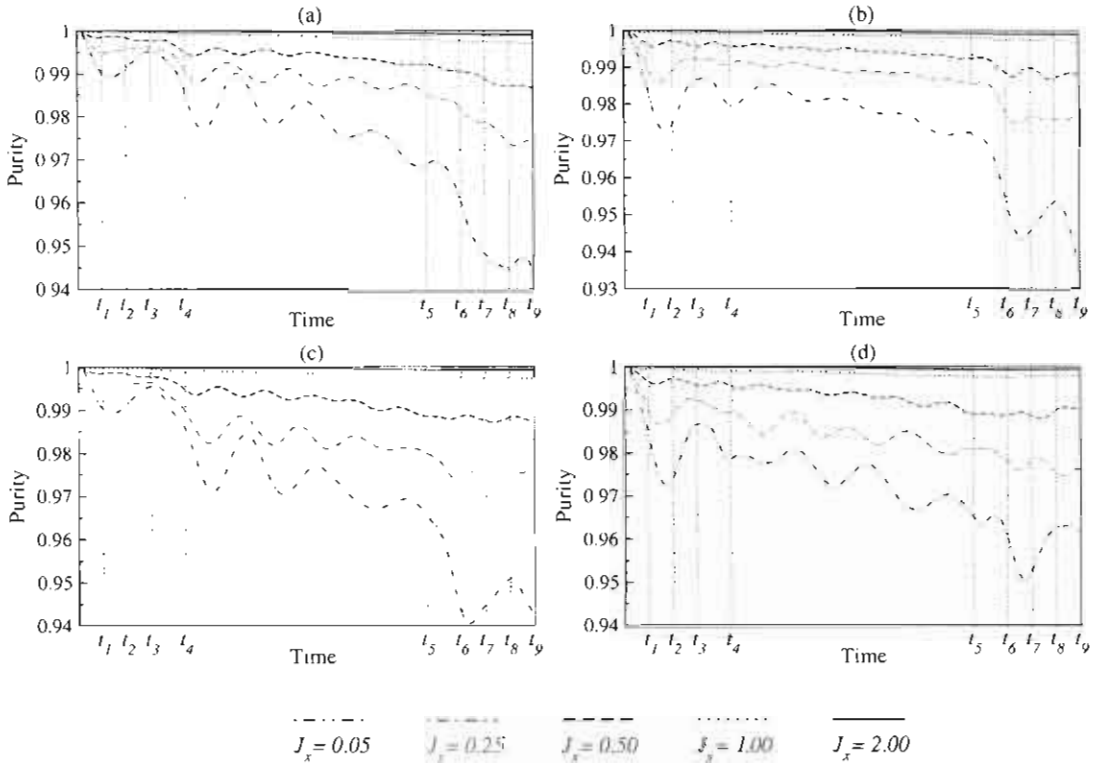

Figure 4.5: Time evolution of purity, $\mathcal{P}(t)$, in the case of bit–flip errors (generated by xx-type coupling) plotted for five different values of intra-bath coupling, $J_x = 0.05, 0.25, 0.50, 1.00, 2.00$ ϵ in (a) for $|00\rangle$, in (b) for $|01\rangle$, in (c) for $|10\rangle$, and in (d) for $|11\rangle$.

increasing J_x, which causes accidental near degeneracies in the low energy spectrum of the bath. The number of thermally and dynamically populated bath states can then increase with increasing J_x. This then results in an anomalous increase of decoherence with J_x. In some QC architectures (e.g. symmetric xy-models) not considered here, this is the dominant effect. In these cases the bath chaos may not be an efficient approach to correct the non-unitary errors. However, in all cases, large unitary errors originating from the coherent shift process were observed.

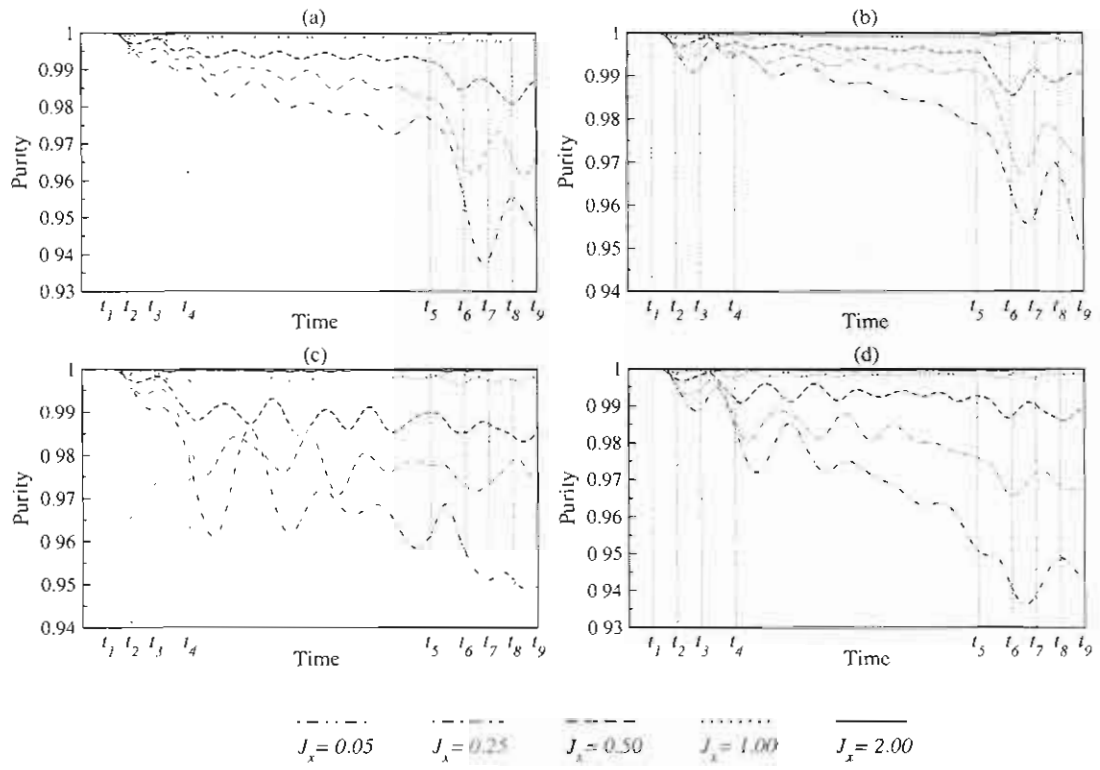

Figure 4.6: Time evolution of purity, $\mathcal{P}(t)$, in the case of phase errors (generated by zz-type coupling) plotted for five different values of intra-bath coupling, $J_x = 0.05, 0.25, 0.50, 1.00, 2.00$ ϵ in (a) for $|00\rangle$, in (b) for $|01\rangle$, in (c) for $|10\rangle$, and in (d) for $|11\rangle$.

4.2 Performance for individual initial states

In this section the performance of the CNOT gate is examined for individual initial states. In section 4.2.1, by examining the purity plots, the errors due to the decoherence and dissipation are discussed. In section 4.2.2 the unitary errors due to the coherent shifting are discussed by examining the fidelity plots.

Figures 4.5–4.8 show purities, $\mathcal{P}(t)$, and figures 4.9-4.12 show fidelities, $\mathcal{F}(t)$, as a function of time. Each figure contains four subfigures in which results for four initial register states are plotted. For the standard initial states the subfigure (a) is reserved for the state $|00\rangle$, the subfigure (b) for $|01\rangle$, the subfigure (c) for $|10\rangle$, and the subfigure (d) for $|11\rangle$.

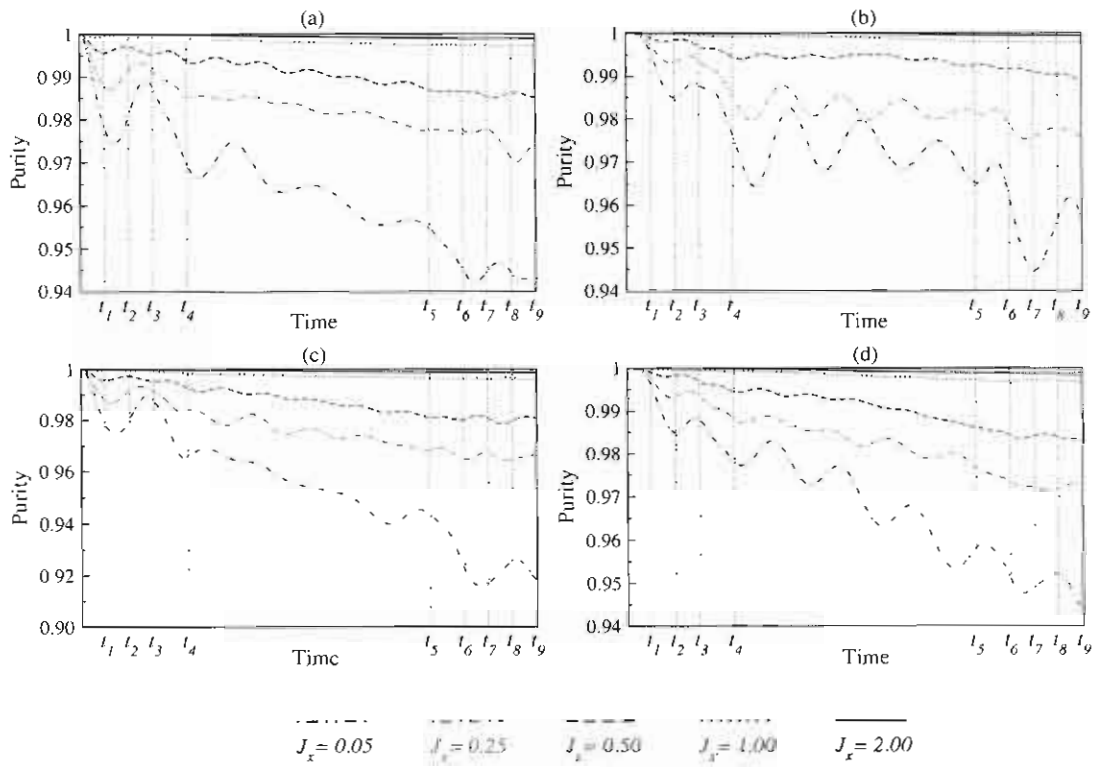

Figure 4.7: Time evolution of purity, $\mathcal{P}(t)$, in the case of bit–flip errors (generated by xx-type coupling) plotted for five different values of intra-bath coupling, $J_x = 0.05, 0.25, 0.50, 1.00, 2.00$ ϵ in (a) for $(|00\rangle + |11\rangle)/\sqrt{2}$, in (b) for $(|00\rangle - |11\rangle)/\sqrt{2}$, in (c) for $(|01\rangle + |10\rangle)/\sqrt{2}$, and in (d) for $(|01\rangle - |10\rangle)/\sqrt{2}$.

Similarly, for the initial Bell states, the subfigure (a) is reserved for $(|00\rangle + |11\rangle)/\sqrt{2}$, the subfigure (b) for $(|00\rangle - |11\rangle)/\sqrt{2}$, the subfigure (c) for $(|01\rangle + |10\rangle)/\sqrt{2}$, and the subfigure (d) for $(|01\rangle - |10\rangle)/\sqrt{2}$. For each initial condition the purity or fidelity is plotted for five different values of the intra-bath coupling, J_x, in the same subfigure. The switching times of elementary gates are also labeled for each subfigure.

4.2.1 Errors due to decoherence and dissipation

The purity is plotted for xx-type coupling in figure 4.5 for the standard initial basis states. In each subfigure, five different curves represent the different values of J_x. Clearly, the lower

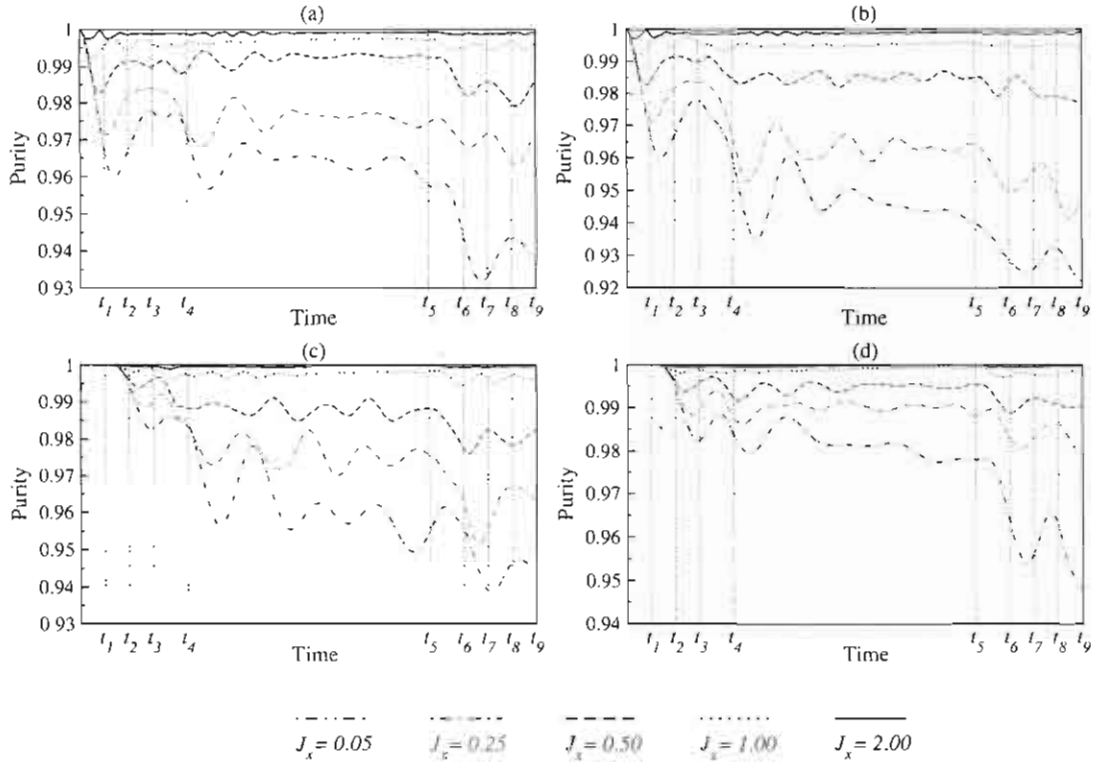

Figure 4.8: Time evolution of purity, $\mathcal{P}(t)$, in the case of phase errors (generated by zz-type coupling) plotted for five different values of intra-bath coupling, $J_x = 0.05, 0.25, 0.50, 1.00, 2.00\ \epsilon$ in (a) for $(|00\rangle + |11\rangle)/\sqrt{2}$, in (b) for $(|00\rangle - |11\rangle)/\sqrt{2}$, in (c) for $(|01\rangle + |10\rangle)/\sqrt{2}$, and in (d) for $(|01\rangle - |10\rangle)/\sqrt{2}$.

the J_x the greater the deviations from the ideal value of purity, i.e. $\mathcal{P}(t) = 1$. For the smallest value of intra-bath interaction (i.e. $J_x = 0.05\ \epsilon$), the highest magnitude of error is observed. With increasing J_x, the errors systematically decrease. For $J_x = 2.00\ \epsilon$, there is almost no sign of error. For the lower values of J_x some oscillations in purity are observed. These are indicators of the memory effects present in the dynamics. These effects suggest that regular baths (i.e. non-chaotic) are more non-Markovian and cause more decoherence and dissipation than chaotic baths.

All subfigures for the standard initial states show qualitatively similar behavior. Clearly, however, there are also some quantitative differences which are indicators of state specificity.

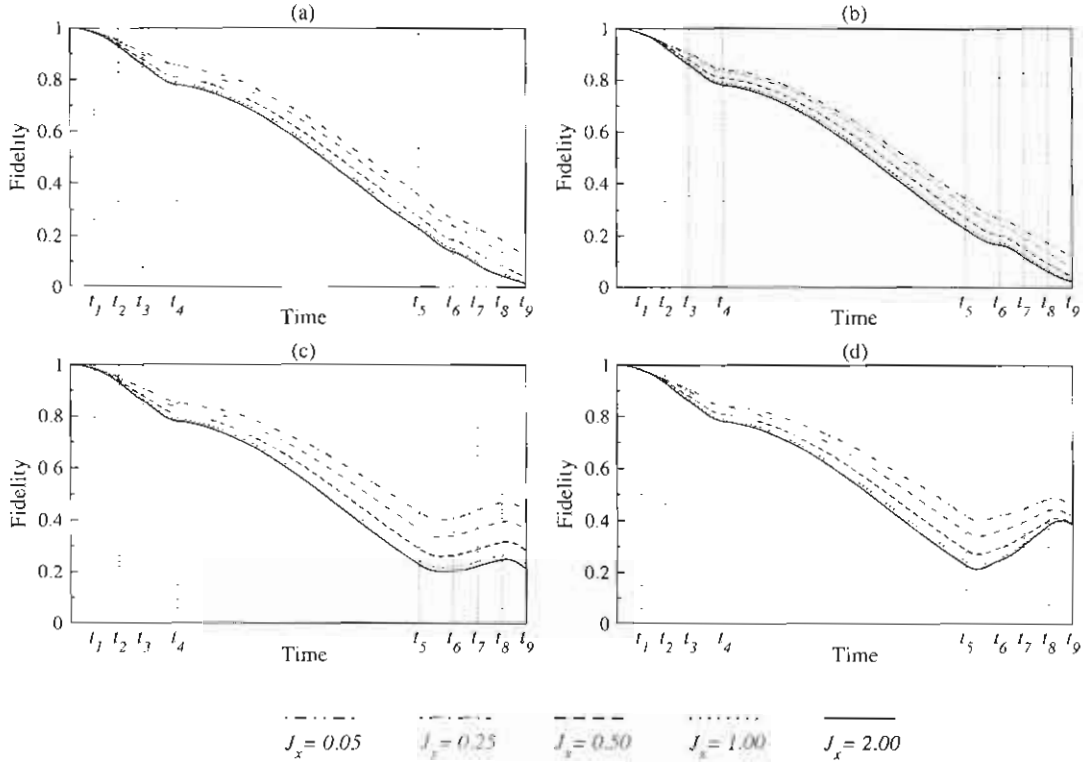

Figure 4.9: Time evolution of fidelity, $\mathcal{F}(t)$, in the case of bit–flip errors (generated by xx-type coupling) plotted for five different values of intra-bath coupling, $J_x = 0.05, 0.25, 0.50, 1.00, 2.00\ \epsilon$ in (a) for $|00\rangle$, in (b) for $|01\rangle$, in (c) for $|10\rangle$, and in (d) for $|11\rangle$.

For example, in figure 4.5, the early dynamics $t \leq t_4$ look similar in subfigures (a) and (c), and in subfigures (b) and (d) for $J_x = 0.05, 0.25, 0.50\ \epsilon$. But subfigures (a) and (b) look quite different on the same time scale, where bunching of the curves is seen at t_3 in subfigures (a) and (c), but there are clearly separated curves in subfigures (b) and (d) at the same time. While the short time similarities of subfignres (a) and (c) continue throughout the dynamics, the dynamics of purity in subfigures (b) and (d) then evolve rather differently. The pronounced oscillations in the purity are seen at the regular bath regime in subfigure (d), but those seen in subfigure (b) are more monotonic. For $J_x = 0.05\ \epsilon$, the purity at t_9 is roughly 0.935 in subfigure (b) and 0.9625 in subfigure (d) which is a significant

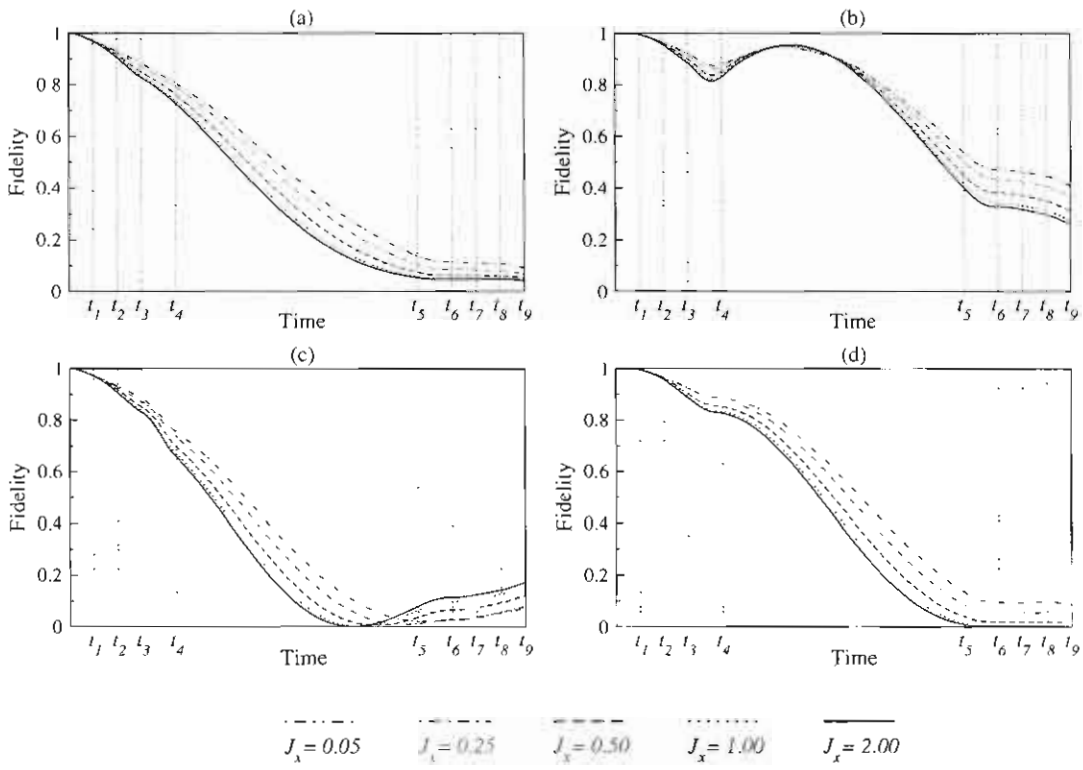

Figure 4.10: Time evolution of fidelity, $\mathcal{F}(t)$, in the case of bit-flip errors (generated by xx-type coupling) plotted for five different values of intra-bath coupling, $J_x = 0.05, 0.25, 0.50, 1.00, 2.00$ ϵ in (a) for $(|00\rangle + |11\rangle)/\sqrt{2}$, in (b) for $(|00\rangle - |11\rangle)/\sqrt{2}$, in (c) for $(|01\rangle + |10\rangle)/\sqrt{2}$, and in (d) for $(|01\rangle - |10\rangle)/\sqrt{2}$.

difference. Hence, there is an apparent state specificity to some degree for xx-type coupling for the smaller J_x values. However, the $J_x = 1.00$ and 2.00 ϵ curves show almost no state specificity.

In figure 4.6, the purity for the standard initial basis states and zz- type error generator is plotted. Here the purity plots again show an improvement in purity as J_x increases. The magnitude of the errors is quite similar to that for xx-type coupling. The early dynamics $t \leq t_4$ are similar in subfigures (a) and (c), and in subfigures (b) and (d) for the lowest J_x values. There are no strong similarities in purity for any subfigures after t_4. Here state specific behavior appears quite strong with the most divergence taking place during the

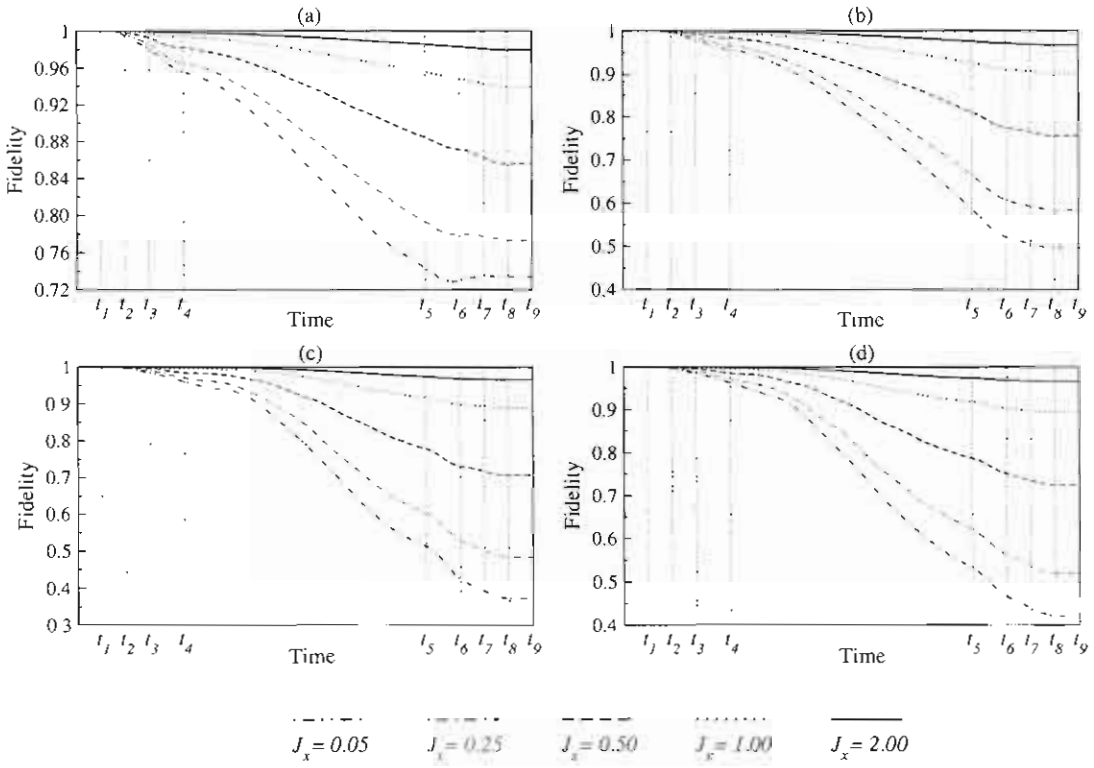

Figure 4.11: Time evolution of fidelity, $\mathcal{F}(t)$, in the case of phase errors (generated by zz-type coupling) plotted for five different values of intra-bath coupling, $J_x = 0.05, 0.25, 0.50, 1.00, 2.00\ \epsilon$ in (a) for $|00\rangle$, in (b) for $|01\rangle$, in (c) for $|10\rangle$, and in (d) for $|11\rangle$.

two-qubit gate. However, the highest two J_x values show little state specificity.

In figure 4.7, the purity for xx-type coupling and the Bell type initial conditions are examined. A rapid correction of errors is observed with increasing J_x. For $J_x = 0.05\ \epsilon$, again, the worst decoherence is seen, but otherwise the dynamics display qualitatively similar behavior to that for the standard basis states. State specific effects look slightly less pronounced than those seen in figure 4.5.

In figure 4.8, the purity is plotted for the Bell states and zz-type system-bath interactions. The behavior of phase errors does not differ much relative to those observed for the standard basis states. However, in subfigures (a) and (b) the short time dynamics are quite

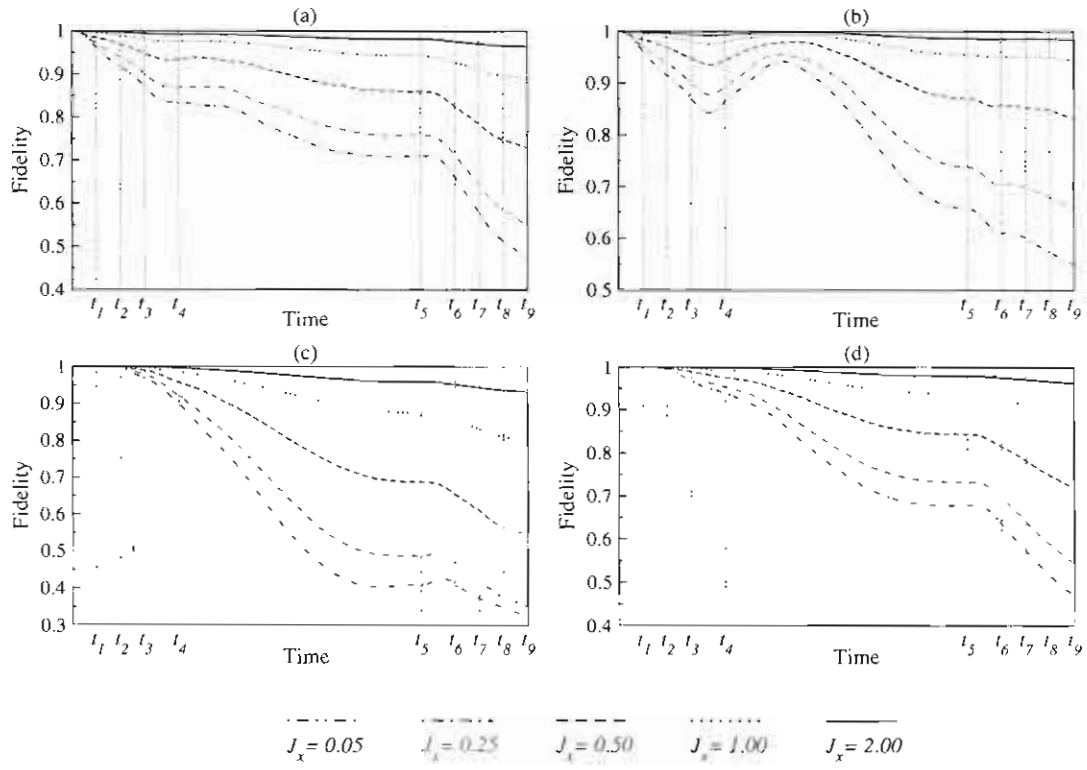

Figure 4.12: Time evolntion of fidelity, $\mathcal{F}(t)$, in the case of phase errors (generated by zz-type coupling) plotted for five different values of intra-bath coupling, $J_x = 0.05, 0.25, 0.50, 1.00, 2.00\ \epsilon$ in (a) for $(|00\rangle + |11\rangle)/\sqrt{2}$, in (b) for $(|00\rangle - |11\rangle)/\sqrt{2}$, in (c) for $(|01\rangle + |10\rangle)/\sqrt{2}$, and in (d) for $(|01\rangle - |10\rangle)/\sqrt{2}$.

different.

In all figures non-negligible deviations of the purity from the theoretically desirable limit of 0.99999 [87] are observed for the experimentally relevant two-qubit coupling strength $J_x = 0.05\ \epsilon$. Recall that the number of idle bath qubits directly participating in the decoherence process was relatively small, i.e. $N = 10$. This number could be higher for larger QCs, which suggests that internal decoherence can be a matter of concern in a QC core in the presence of static internal imperfections. However, it is also clear that increasing the intra-bath interaction strength, J_x, causes a rapid improvement in purity. Hence, the bath chaos stabilizes the gate implementation by causing a reduction of decoherence. For the

strongest coupling case, $J_x = 2.00\ \epsilon$, the effect of decoherence almost completely disappears for both types of coupling operators and all initial conditions. This suggests that induced bath chaos may serve as an error correcting strategy when such strong intra-bath interactions are experimentally accessible.

Overall, the decrease of the purities with time appears qualitatively similar for all initial conditions, but the Bell states perform slightly worse than the standard basis states. Since the Bell states are entangled states representing the state of two spatially separated qubits, they seem more susceptible to the destructive effects of decoherence. Performance with respect to the type of coupling operator appears to be quite similar in all cases. Overall, the purity decays are of comparable magnitude for both bit-flip and phase type couplings. However, intriusic decoherence due to particular initial conditions and coupling operators is also seen. For example, decoherence by xx-type coupling affects the system during the first gate operation for all initial conditions. In the case of zz-type coupling, however, the errors do not emerge until the second gate operation for all standard basis states (as seen in figure 4.6) and for two of the Bell states (as seen in figures 4.8(c) and 4.8(d)).

Decoherence is a state–dependent phenomenon. The slight state specificity discussed above cannot be dismissed as negligible, because the small effects observed in one gate could get amplified over time during other gates. In almost all cases the observed state specific effects are stronger in the non-chaotic bath regime. The chaotic bath dynamics also reduce the state specific effects.

4.2.2 Errors due to coherent shifting

The time evolution of fidelity, $\mathcal{F}(t)$, for xx-type coupling is plotted in figure 4.9 for the standard initial basis states and in figure 4.10 for the Bell states. Overall, the fidelity plots show qualitatively similar behavior in that they start at one and decay quite uniformly toward zero at the end of the gate. The fidelity plots show almost no dependency on J_x.

However, with increasing J_x fidelities do get slightly worse. The purity plots showed that the deviations of the purity from unity were less than ten percent in all cases. Here all fidelity is lost over the course of a single CNOT gate. Moreover, all of this error should be of unitary origin as it does not affect the purity. The degree of error the fidelity plots indicate is alarming. But since the error is mostly unitary and thus deterministic, there may be some systematic way to remove the unitary error component. Some state specific recurrences are also seen in subfigures 4.9(c), 4.9(d) and in subfigure 4.10(c).

Figures 4.11 and 4.12 plot the fidelity for the initial standard basis states and the initial Bell states, respectively. The fidelity plots indicate that the behavior of phase errors is quite different from those observed for the bit-flip errors. Interestingly, with increasing J_x, dramatic improvements in fidelity are observed. While in the regular bath regime, the fidelity loss is about sixty percent, in the chaotic regime it is close to the acceptable limit. Moreover, the magnitude of fidelity improvement is highly sensitive to the strength of the intra-bath coupling, J_x,. The fidelity plots do not show a strong initial state dependency but the fidelity decay for the Bell states in subfigures 4.12(a) and (b), and (c) and (d) show similar behaviors for $t \leq t_4$.

Chapter 5

Probing internal bath dynamics by a Rabi detector

Internal errors in a quantum computer (QC) core may arise due to the existence of one-body imperfections or as a consequence of residual two-body interactions, or even as a result of strong residual interactions with other local impurities in a QC core. One–body imperfections can be readily corrected in many cases. Two-body interactions are more difficult to deal with and their effects are difficult to predict, since these interactions generate an internal decoherence mechanism. Knowledge of the strength of the two-body intra-bath interactions may prove very useful for eliminating their effects. It has been observed in [16, 17] and shown in chapter 4 that the coherent shift is sensitive to the strength of bath self-interaction [16, 17]. In this chapter[§], it is shown that a single qubit detector can be configured to measure the bath self-interactions. A model system representing a qubit detector interacting with an isolated QC with static internal imperfections is presented. In the absence of interactions with the QC, the detector undergoes phase evolution only. When the detector experiences a coherent shift, as a result of interaction with the QC,

[§]This chapter is partly based on a study [18] reported by Çetinbaş and Wilkie.

it begins Rabi oscillations. The fidelity of the detector also exhibits a periodicity on a much longer timescale with a period which is highly sensitive to the strength of bath self-interaction. Measuring the Rabi oscillations or the period fidelity allows one to find the intra-bath coupling strength. Moreover, it should be possible to apply the basic ideas behind the detector set-up in more general contexts such as optical impurities in solids where knowledge of bath self-interaction could be important.

The study presented in this chapter has been previously published in [18], where in addition to exact numerical calculations, approximate results based on a mean-field master equation have been also reported. Recently, errors have been detected in the master equation calculations, making their results of questionable reliability. Here, discussions are be based on exact numerical results. Since the master equation is used as an alternative method to obtain open system dynamics, and the predictions of this master equation are only approximate, the absence of the master equation calculations does not alter the conclusions presented here to any extent.

The organization of this chapter is as follows. The Rabi detector model is described in section 5.1. The exact numerical approach used in the simulations is explained in section 5.2. In section 5.3, exact numerical results are presented for short and very long time dynamics and the results are discussed.

5.1 Description of model

The self-interacting spin-bath model, representing the QC core, consists of $N+1$ two level systems, and is given by the following total Hamiltonian,

$$\hat{H} = \hat{H}_S + \hat{S}\hat{B} + \hat{H}_B, \tag{5.1}$$

where the first term is the free system Hamiltonian,

$$\hat{H}_S = -\frac{1}{2} B_0^z \hat{\sigma}_z^{(0)}, \tag{5.2}$$

the second term represents a system-bath interaction operator in the system $\hat{S}$ and bath $\hat{B}$ degrees of freedom,

$$\hat{S}\hat{B} = \hat{\sigma}_x^{(0)}\hat{\Sigma}_x \quad \text{and} \quad \hat{\Sigma}_x = \sum_{i=1}^{N} \lambda_i \hat{\sigma}_x^{(i)}, \tag{5.3}$$

and the third term is the batb Hamiltonian given by

$$\hat{H}_B = -\frac{1}{2}\sum_{i=1}^{N}\left(B_i^x\hat{\sigma}_x^{(i)} + B_i^z\hat{\sigma}_z^{(i)}\right) + \sum_{i=1}^{N-1}\sum_{j=i+1}^{N} J_x^{i,j}\hat{\sigma}_x^{(i)}\hat{\sigma}_x^{(j)}. \tag{5.4}$$

The index 0 is used to label the detector qubit. The index runs from 1 to N for the bath qubits. The imperfections are modeled by choosing the parameters of $\hat{S}\hat{B}$ and $\hat{H}_B$ randomly as done previously in chapter 3.

5.1.1 Parameters

The parameters used in the numerical calculations are based on a Josephson charge-qubit QC proposal [68, 69] for which the experimentally accessible one–qubit energy to perform a single-qubit rotation is $B_0^z = 1.00\ \epsilon$ where $\epsilon = 200$ mK. Since all qubits in the Hamiltonian (5.1) are the components of the same QC, the imperfections in single–qubit parameters should only differ from B_0^z by a detuning parameter, which is set to the value $\delta = 0.4\ \epsilon$. Static noise is added to all qubits except the detector qubit by choosing $B_i^z \in [B_0^z - \delta/2, B_0^z + \delta/2]$ and $B_i^x \in [B_0^z - \delta/2, B_0^z + \delta/2]$. The residual two-body interactions are modeled randomly and uniformly by choosing λ_i and $J_x^{i,j}$ from $\lambda_i \in [-\lambda, \lambda]$ and $J_x^{i,j} \in [-J_x, J_x]$, respectively. While a number of intra-bath coupling strengths, i.e. $J_x = 0.00, 0.15, 0.50, 1.00, 2.00$ in units of ϵ, are considered to explore the integrable to chaotic transition (see the final chapter for confirmation of chaos), only one system-bath coupling value, which corresponds to the experimental value for a two-qubit rotation, i.e. $\lambda = 0.05\ \epsilon$, is considered. In all the calculations the temperature is set to $kT = 0.25\ \epsilon$, and the time step of integration is $\Delta t = 0.2\ \hbar/\epsilon$ s.

5.1.2 Initial conditions

It is assumed that the dynamics of the QC are initiated from a state of product form,

$$\hat{\rho}(0) = \hat{\rho}_S(0) \otimes \hat{\rho}_B(0). \tag{5.5}$$

Here, $\hat{\rho}_B(0)$ is the canonical bath density and $\hat{\rho}_S(0) = |\psi(0)\rangle\langle\psi(0)|$ is the reduced density operator for the detector where $|\psi(0)\rangle = (|0\rangle + |1\rangle)/\sqrt{2}$. This state of the detector qubit will only undergo phase evolution in the absence of interactions with the QC. However, once the interactions are in effect, the detector will show Rabi oscillations.

5.2 Exact numerical approach

By exploiting the low temperature regime for the bath degrees of freedom, the initial bath density is approximated as

$$\hat{\rho}_B(0) = \sum_{n=1}^{n_{eig}} p_n |\phi_n^B\rangle\langle\phi_n^B| \tag{5.6}$$

where $p_n = \exp(-E_n/kT)/\sum_{m=1}^{n_{eig}} \exp(-E_m/kT)$ are the populations of the thermal bath state and $\hat{H}_B|\phi_n^B\rangle = E_n|\phi_n^B\rangle$. Here, the sum in (5.6) is over only the thermally populated lowest energy eigenstates of the bath. Therefore, n_{eig} is a cutoff such that the states with $n_{eig}+1$ and higher are unoccupied for the fixed low temperature. While the density of bath states and thus the number of thermally populated states varies slowly with J_x for a fixed bath temperature, $n_{eig} = 20$ was sufficient for all cases.

The time–evolved reduced density is obtained from,

$$\hat{\rho}_S(t) = \sum_{n=1}^{n_{eig}} p_n \ \mathrm{Tr}_B[|\Psi_n(t)\rangle\langle\Psi_n(t)|], \tag{5.7}$$

where each $|\Psi_n(t)\rangle$ evolves according to the Schrödinger equation,

$$i\hbar\frac{d}{dt}|\Psi_n(t)\rangle = \hat{H}|\Psi_n(t)\rangle, \tag{5.8}$$

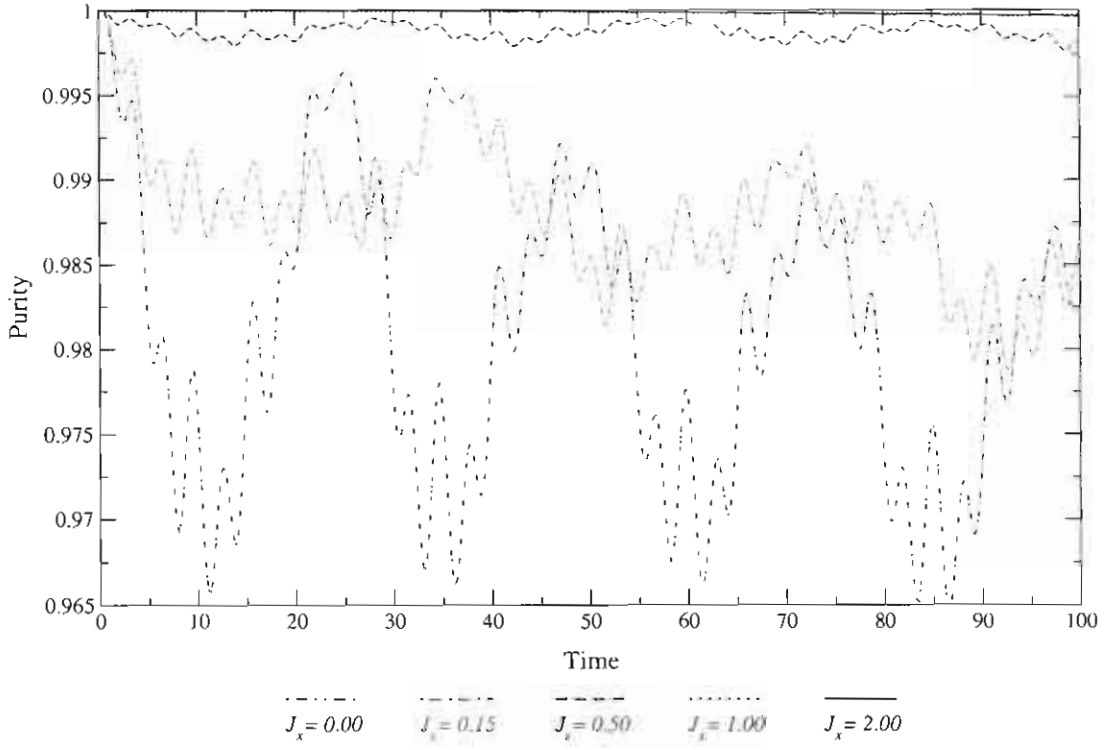

Figure 5.1: Short time dynamics of purity, $\mathcal{P}(t)$, plotted for five different values of intra-bath couplings, $J_x = 0.00, 0.15, 0.50, 1.00, 2.00\ \epsilon$.

for all initial states of the form, $|\Psi_n(0)\rangle = |\psi(0)\rangle \otimes |\phi_n^B\rangle$. A Lanczos algorithm [85] is used for the diagonalization of the bath Hamiltonian for $N = 10$ qubits, and an eighth order variable stepsize Runge-Kutta method [86] for the numerical integrations.

5.3 Results

Purity and fidelity are used to estimate deviations from the pure phase evolution in the state of the detector qubit. Purity, defined by $\mathcal{P}(t) = \mathrm{Tr}_S[\hat{\rho}_S(t)^2]$, is a good measure of decoherence and dissipation since it is insensitive to the coherent effects. For pure initial states, the ideal value of purity is equal to one. This would be the case if interaction with the bath causes only coherent shifting but no decoherence. Fidelity, defined by $\mathcal{F}(t) =$

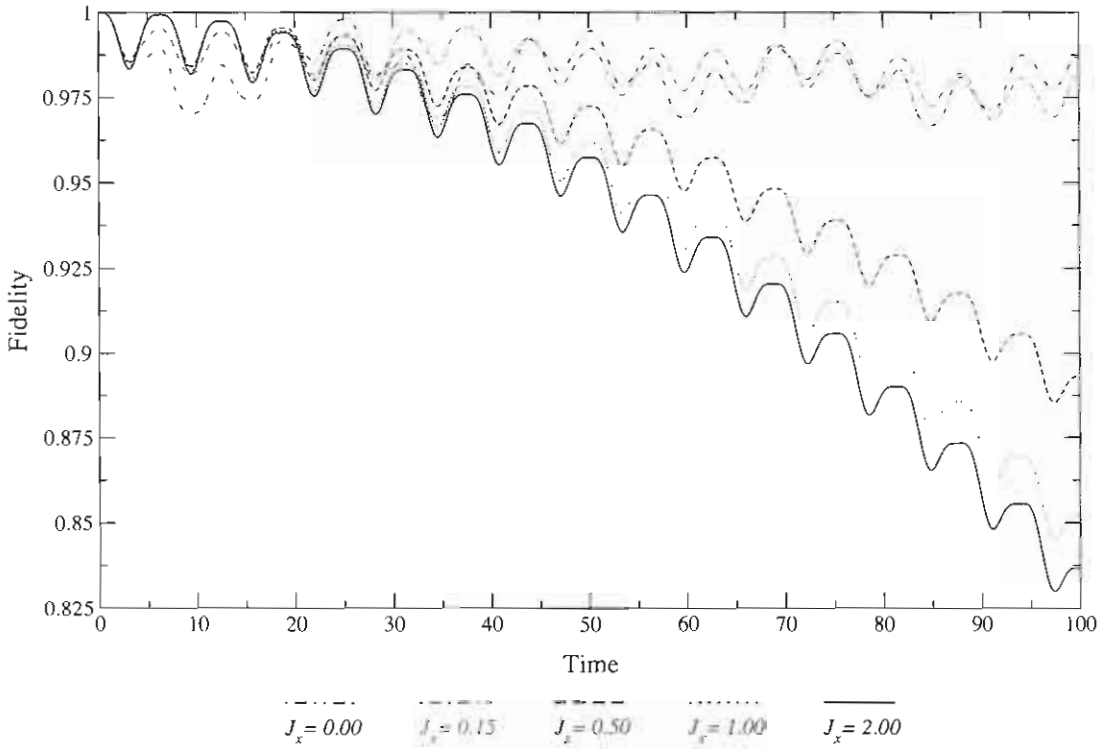

Figure 5.2: Short time dynamics of fidelity, $\mathcal{F}(t)$, plotted for five different values of intra-bath couplings, $J_x = 0.00, 0.15, 0.50, 1.00, 2.00\ \epsilon$.

$\mathrm{Tr}_S[\hat{\rho}_S(t)\hat{\rho}_S^{ideal}(t)]$ is sensitive to both coherent effects and decoherence. Here, $\hat{\rho}_S^{ideal}(t)$ stands for the ideal system evolution at time t, in the absence of system-bath interactions. Fidelity measures how close an open system's evolution is to the ideal system evolution. For pure initial states, the ideal value of fidelity is also one in the absence of system-bath interactions. The large deviations in the magnitudes of purity and fidelity gives an indication of coherent shifting.

Recall that the initial state of the detector qubit is $(|0\rangle + |1\rangle)/\sqrt{2}$. In the absence of coherent shifting, this state should undergo only phase evolution without significant population transfer. However, in the presence of coherent shifting, the free system Hamiltonian will be shifted by the system coupling operator and thus the detector qubit should display large amplitude Rabi oscillations. Therefore, the populations of the detector qubit will also

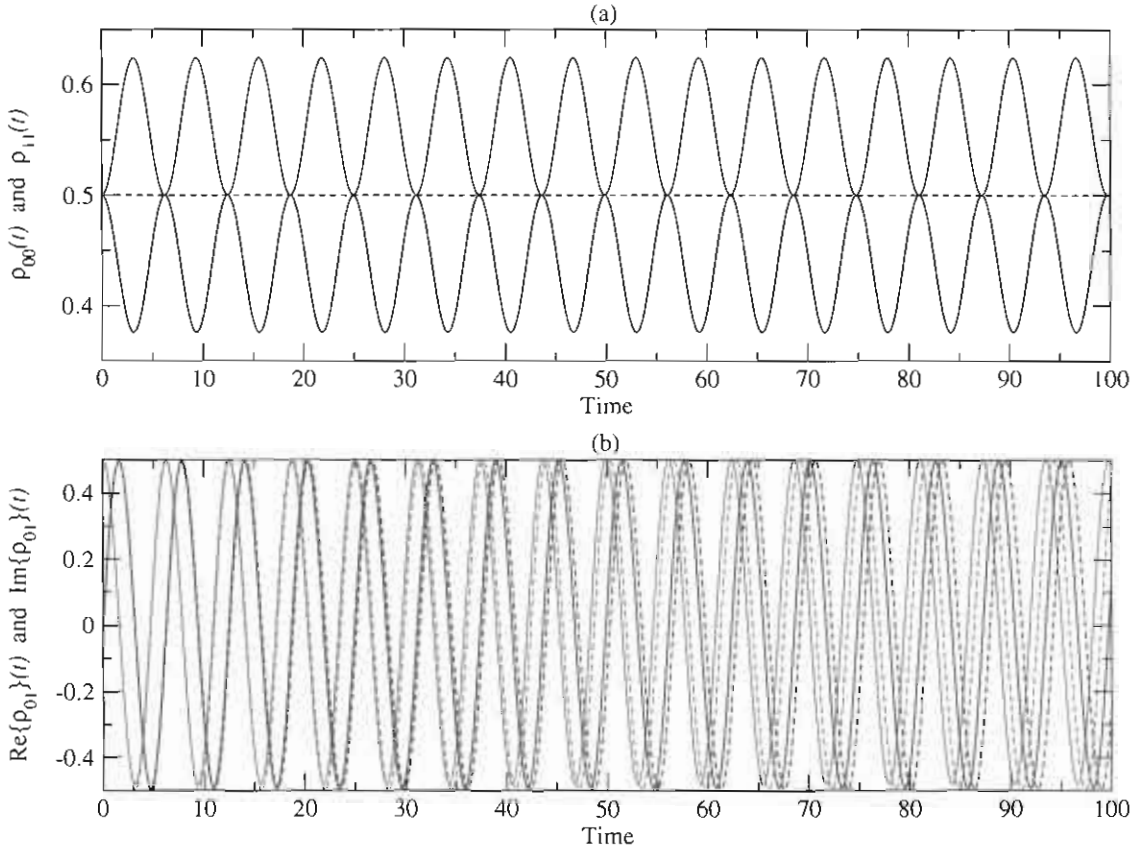

Fignre 5.3: Short time dynamics of matrix elements of density operator, $\hat{\rho}_S(t)$, plotted for coherent (dashed lines) and decoherent (solid lines) time evolntion for $J_x = 1.00\ \epsilon$: (a) Diagonals of $\hat{\rho}_S(t)$, $\rho_{00}(t) = \langle 0|\hat{\rho}_S(t)|0\rangle$ (blue) and $\rho_{11}(t) = \langle 1|\hat{\rho}_S(t)|1\rangle$ (black). (b) Real part of off-diagonal element of $\hat{\rho}_S(t)$, $\mathrm{Re}\{\rho_{01}\}(t) = \mathrm{Re}\{\langle 0|\hat{\rho}_S(t)|1\rangle\}$ (green) and imaginary part of off-diagonal of $\hat{\rho}_S(t)$, $\mathrm{Im}\{\rho_{01}\}(t) = \mathrm{Im}\{\langle 0|\hat{\rho}_S(t)|1\rangle\}$ (red).

be monitored to see emergence of the Rabi oscillations as a result of the coherent shift process.

5.3.1 Short time dynamics

The short time dynamics of $\mathcal{P}(t)$ and $\mathcal{F}(t)$ are plotted in figures 5.1 and 5.2, respectively, for five different values of intra-bath couplings, J_x. Figure 5.1 shows a systematic improvement in $\mathcal{P}(t)$ with increasing J_x. For the regular bath, i.e. $J_x = 0.00\ \epsilon$, the decoherence is at its

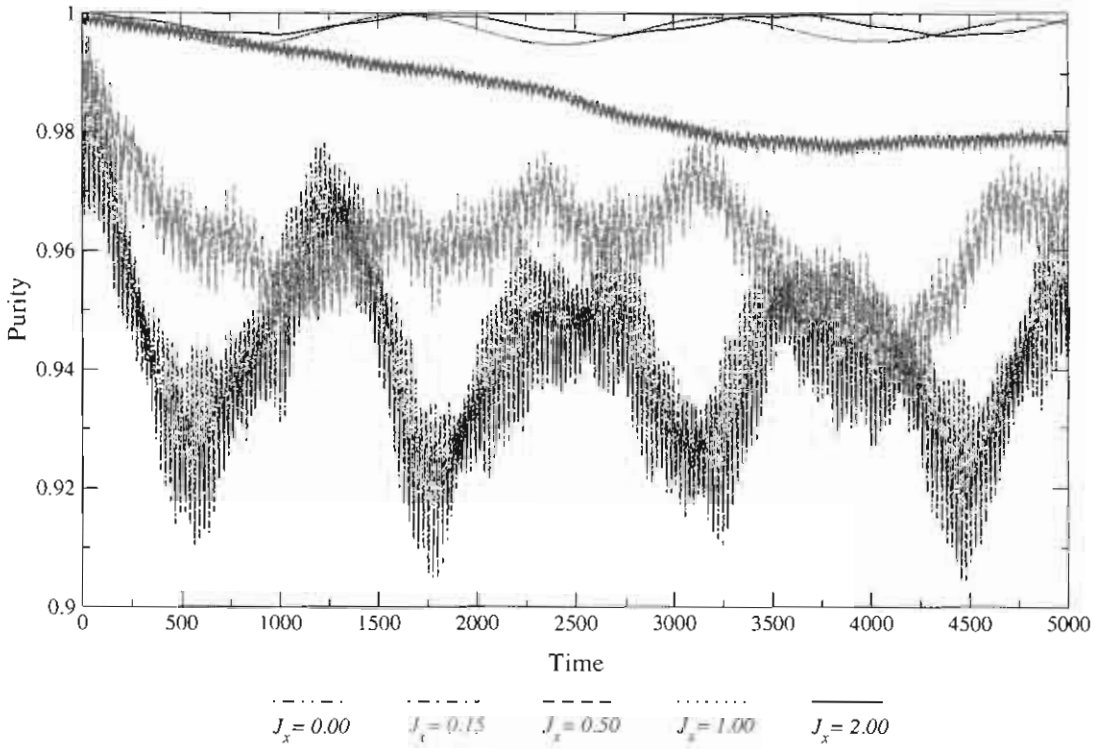

Figure 5.4: Long time dynamics of purity, $\mathcal{P}(t)$, plotted for five different values of intra-bath couplings, $J_x = 0.00, 0.15, 0.50, 1.00, 2.00\ \epsilon$.

maximum. Above $J_x = 0.15\ \epsilon$, chaos sets in and the decoherence is systematically reduced. For the strongly chaotic regime, i.e. $J_x = 2.00\ \epsilon$, the decoherence almost totally vanishes. This result is in agreement with earlier studies, e.g. [29, 30], in which the bath chaos is predicted to reduce decoherence.

The purity plots show partial recurrences in the regular bath regime. Such purity recurrences have been previously observed for a number of studies [29, 88]. These recurrences lessen with increasing magnitude of intra-bath coupling. This effect is attributed to the transition from non-Markovian to Markovian behavior as a result of chaos, and is discussed in detail in the final chapter of this thesis.

The fidelity plots in figure 5.2 show the presence of much larger deviations from unity than those shown by the purity plots. The fidelity plots also show a quite different trend

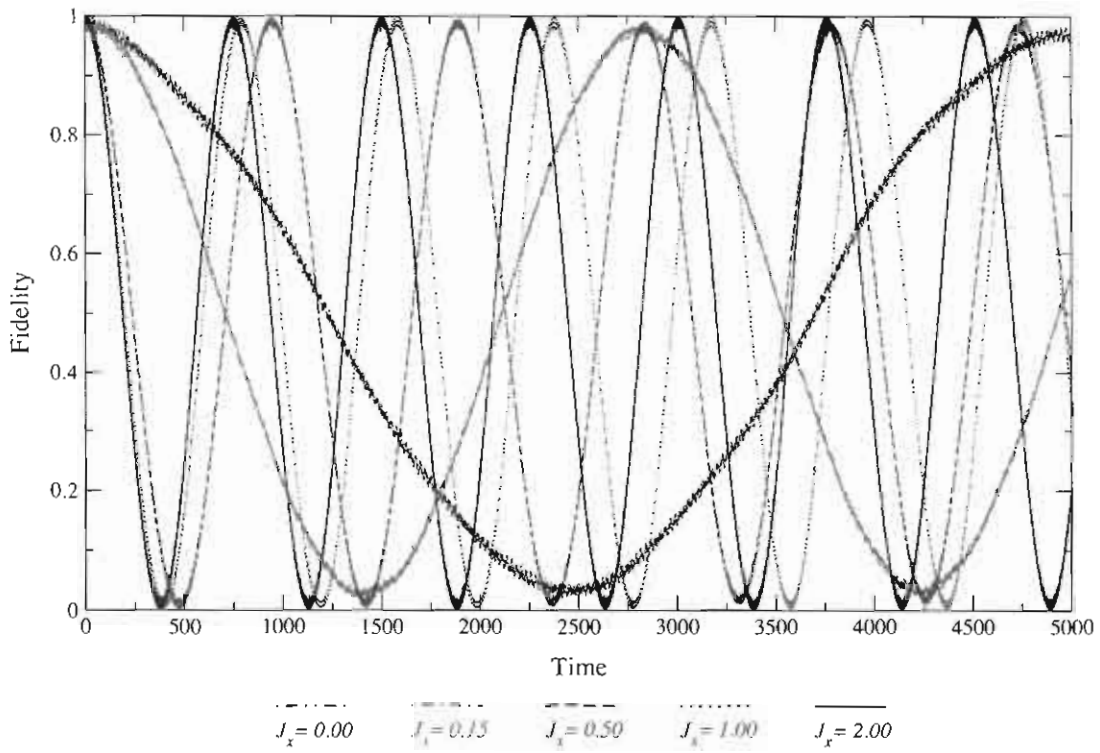

Figure 5.5: Long time dynamics of fidelity, $\mathcal{F}(t)$, plotted for five different values of intra-bath couplings, $J_x = 0.00, 0.15, 0.50, 1.00, 2.00\ \epsilon$.

with increasing J_x. After a short time, $\mathcal{F}(t)$ begins to decay more rapidly for larger values of J_x. This supports the conclusion that large coherent shifts are again present in the dynamics as was the case in the CNOT study [16, 17] of chapter 5. It seems that the coherent shift process is much more harmful than decoherence or dissipation processes as a potential error source for quantum computation [16, 17]. However, it is shown here that the coherent shifting can be put to a good purpose. It is also noteworthy that while the coherent shift vanishes in some standard models of decoherence, it is nonzero in general for self-interacting baths. Therefore, large magnitude errors induced by the coherent shift process should also be expected for condensed phase environments.

In figure 5.3, the matrix elements of the detector qubit are plotted for $J_x = 1.00\ \epsilon$. In figure 5.3(a), large magnitude Rabi oscillations are seen in the populations. There is also

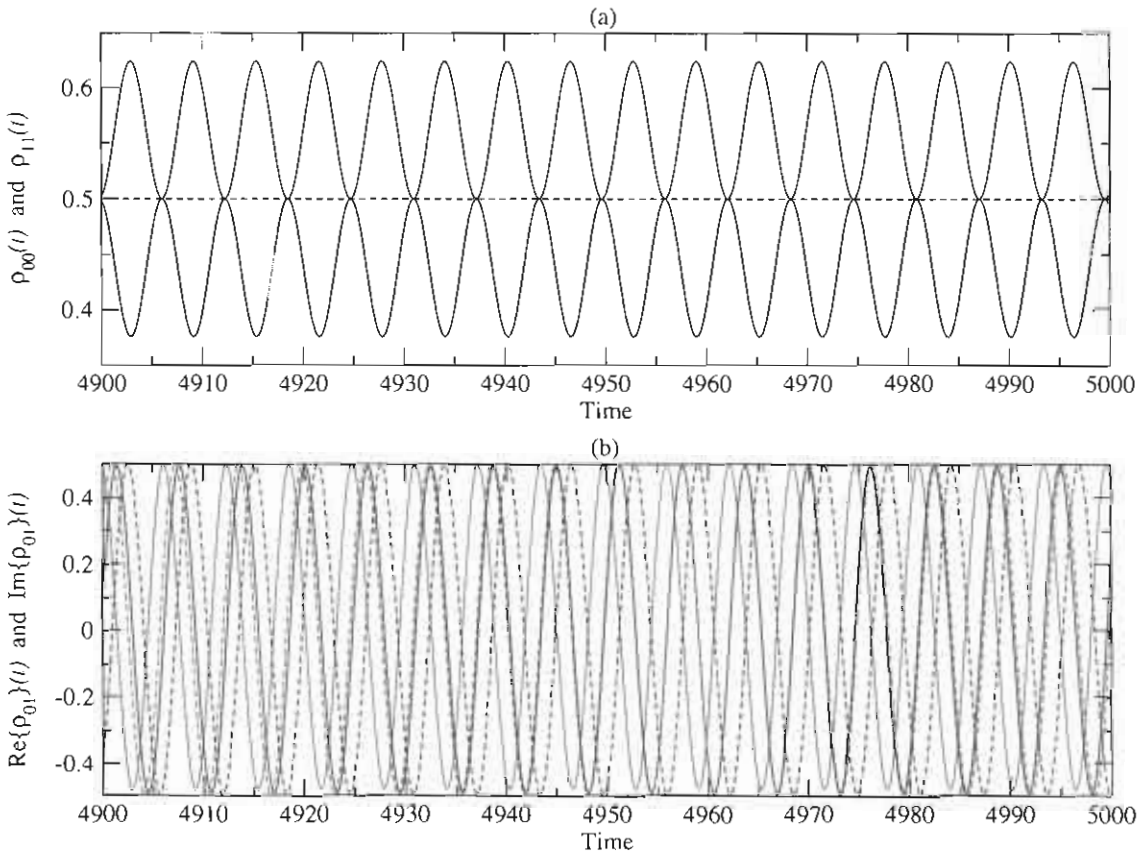

Figure 5.6: Long time dynamics of matrix elements of density operator, $\hat{\rho}_S(t)$, plotted for coherent (dashed lines) and decoherent (solid lines) time evolution for $J_x = 1.00\ \epsilon$: (a) Diagonals of $\hat{\rho}_S(t)$, $\rho_{00}(t) = \langle 0|\hat{\rho}_S(t)|0\rangle$ (blue) and $\rho_{11}(t) = \langle 1|\hat{\rho}_S(t)|1\rangle$ (black). (b) Real part of off-diagonal element of $\hat{\rho}_S(t)$, $\mathrm{Re}\{\rho_{01}\}(t) = \mathrm{Re}\{\langle 0|\hat{\rho}_S(t)|1\rangle\}$ (green) and imaginary part of off-diagonal of $\hat{\rho}_S(t)$, $\mathrm{Im}\{\rho_{01}\}(t) = \mathrm{Im}\{\langle 0|\hat{\rho}_S(t)|1\rangle\}$ (red).

a small shift of off-diagonal matrix elements seen in figure 5.3(b). These oscillations are a direct consequence of the coherent shift process that emerges as a result of system-bath interactions.

5.3.2 Long time dynamics

In figure 5.4 the exact numerical results for purity are plotted for five different values of J_x. Figure 5.4 shows that suppression of decoherence with increasing J_x is also the dominant

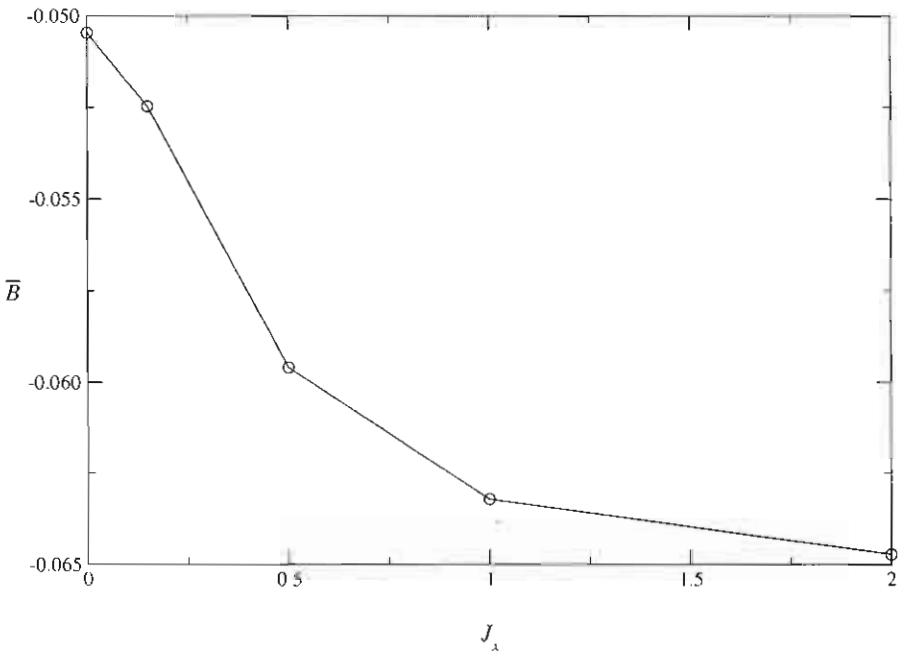

Figure 5.7: Canonical average of bath coupling operator, $\bar{B}$, versus J_x.

effect in the long time dyuamics of the purity. In addition, the purity plots reflect the presence of long time partial recurrences iu the regular bath regime. These recurrences are again caused by memory effects.

In figure 5.5, the exact numerical results for the long time dynamics of the fidelity are plotted. In the long time limit, the unitary effects of system-environment interactions overwhelm the non-unitary ones, and the contributions of decoherence to the open system dynamics are hardly noticeable anymore. This is true even in the non-chaotic bath regime. Small–magnitude, high–frequency oscillations are still noticeable. However, the fidelity plot displays an additional long–time, large–amplitude periodicity. Moreover, the period of the fidelity is strongly dependent on the magnitude of J_x.

In figure 5.6, the long time dynamics of matrix elements of the detector qubit is plotted for $J_x = 1.00\ \epsilon$. The Rabi oscillations observed in the populations of $\hat{\rho}_S(t)$ for short time dynamics do still persist for the long time dynamics. The magnitudes of the Rabi oscillations

are the same as those of the short dynamics and they do not subside in time.

The form of the chaotic Kraus decomposition and certain approximate master equations [47-51] suggests that the coherent shift process modifies the free system Hamiltonian as $\hat{H}_S \rightarrow \hat{H}_S + \bar{B}\hat{S}$ where $\bar{B} = \mathrm{Tr}\{\hat{B}\hat{\rho}_B(0)\}$ is the canonical average of the bath coupling operator and $\hat{S}$ is the system part of the system-bath coupling operator. Hence, for the detector qubit, the shifted system Hamiltonian is then the following,

$$\hat{H}_S = -\frac{1}{2}B_0^z\hat{\sigma}_z^{(0)} + \bar{B}\hat{\sigma}_x^{(0)}. \tag{5.9}$$

As noted earlier, only phase evolution is expected for the detector qubit in the absence of coherent shifting. The observed Rabi oscillations in the populations of the detector qubit are then induced by the shift term, $\bar{B}\hat{\sigma}_x^{(0)}$.

In figure 5.7, the canonical average of the bath coupling operator, $\bar{B}$, is given as a function of J_x. Figure 5.7 shows that $\bar{B}$ decreases – while its magnitude $|\bar{B}|$ increases – with increasing J_x. The changes in the magnitude of $|\bar{B}$ are fast and very sensitive to intra-bath couplings for small coupling values, i.e. $J_x < 1$, but quite slow above $J_x > 1$. This behavior is in good agreement with the fidelity decay behavior seen in figures 5.2 and 5.5.

Explaining the sensitivity of the fidelity to J_x is straightforward. Neglecting the effects of decoherence and dissipation, it can readily be argued that the shifted system dynamics should beat with a frequency of $\Omega = (B_0^{z2} + \bar{B}^2)^{1/2}/2h$ while the unperturbed system phase evolves with frequency, $\omega = B_0^z/2h$. The period of the Rabi oscillations in the populations seen in figure 5.3(a) is Ω^{-1}. It then follows that the fidelity takes the form,

$$\begin{aligned}\mathcal{F}(t) &= \frac{1}{2}[1 + (\frac{\bar{B}}{\Omega})^2\cos 2\omega t - \frac{B_0^z(\Omega - B_0^z/2)}{4\Omega^2}\cos 2(\Omega+\omega)t \\ &+ \frac{B_0^z(\Omega + B_0^z/2)}{4\Omega^2}\cos 2(\Omega-\omega)t].\end{aligned} \tag{5.10}$$

The second term is very small since $\bar{B}^2$ is very much smaller than Ω^2. The third term is small since $\Omega - B_0^z/2 < \Omega$, and the fourth term is of order 1. Hence, the small magnitude oscillations in fidelity have frequency, $2(\Omega+\omega)$. The large amplitude oscillations are caused

by the fourth term, and they have period, $\pi/(\Omega - \omega) \simeq hB_0^z/2\bar{B}^2$. Generally, $\bar{B}$ is much smaller than B_0^z, but $\bar{B}$ increases with J_x, resulting in a shorter period. This gives rise to the changes in the period of the fidelity and explains the behavior observed in figures 5.2 and 5.5. Since $2(\Omega + \omega)$ varies more slowly with $\bar{B}$, the Rabi oscillations in the populations are not very sensitive to J_x. The above formula (5.10) for $\mathcal{F}(t)$ is in excellent agreement with the exact results for strong intra-bath coupling values, $J_x \geq 1$, and thus strongly supports the conclusion that the shift manifests as $\hat{H}_S \rightarrow \hat{H}_S + \bar{B}\hat{S}$.

Lastly, by measuring the period of the fidelity oscillation one can obtain an estimate of $\bar{B}$, and from figure 5.7 the magnitude of J_x can then be obtained. Hence, this is a detector of the strength of bath self-interaction for this isolated QC model. The same basic setup should also carry over to the case of oscillator baths, and the technique could potentially be used to measure the strength of anharmonic interactions in the condensed phase medium.

Chapter 6

Tests for chaotic Kraus decomposition

A Kraus decomposition for quantum systems interacting with large chaotic environments is derived in chapter 2, where the extension of the decomposition to include time-dependent system Hamiltonians is also provided. The chaotic Kraus decomposition (CKD) is only exact for chaotic baths of thermodynamic dimension. Therefore, the performance of the CKD should be assessed for small sized baths before it can be used for general applications.

In this chapter[§] the CKD is tested against exact numerical results reported in chapters 4 and 5. In particular, the performance of the time-independent form of the CKD is tested against exact numerical results of the Rabi detector study of chapter 5, and the time-dependent extension of the CKD is tested against the exact numerical results obtained for the CNOT study of chapter 4.

To assess the performance of the CKD, the predictions of the CKD are compared with those of exact numerical results for two error quantifiers, i.e. purity and fidelity. The purity is used to assess the accuracy of the CKD for the non-unitary effects, i.e. decoherence and

[§]This chapter is taken from two studies [14, 15] reported by Çetinbaş and Wilkie.

dissipation, and the fidelity is used to estimate the accuracy for the unitary effects of system-environment interactions. In addition, the matrix elements of the reduced density operator predicted by the CKD are compared with those obtained by exact numerical simulations.

The test results show that the CKD is very accurate in spite of the relatively small bath dimension used in the exact simulations. These promising results suggest that the CKD can be a practical computational tool for low temperature simulations of open quantum system dynamics induced by chaotic environments.

6.1 Rabi detector study

In this section an analytic solution of the CKD is presented for the Rabi detector study. The details of Hamiltonians, initial conditions and numerical parameters used in this study are discussed in chapter 5. Here these quantities are reviewed and used to construct the explicit form of Kraus operators for the CKD.

The total Hamiltonian for the Rabi detector study is of the form, $\hat{H} = \hat{H}_S + \hat{S}\hat{B} + \hat{H}_B$; see equation (5.1). Here, $\hat{H}_S$ is the subsystem Hamiltonian defined in equation (5.2). The system-bath coupling operator, $\hat{S}$ for the system part and $\hat{B}$ for the bath part, is given by equation (5.3). The bath Hamiltonian, $\hat{H}_B$, is defined by equation (5.4). The Kraus operators for the Rabi detector study take the following simple form,

$$\hat{\mathcal{K}}_n(t) = \sqrt{p_n} \exp\left\{ \frac{i}{\hbar} (\frac{1}{2} B_z^{(0)} \hat{\sigma}_z - B_{n,n} \hat{\sigma}_x^{(0)}) t \right\}. \tag{6.1}$$

The initial bath populations, $p_n = \exp(-E_n/k_B T)/\sum_{m=1}^{n_{eig}} \exp(-E_m/k_B T)$, and the diagonal matrix elements of the bath coupling operator, $B_{n,n} = \langle \phi_n^B(0)|\hat{B}|\phi_n^B(0)\rangle|$, are calculated by using the exact eigenstates of the bath Hamiltonian obtained in chapter 5.

The reduced density at time t is expressed in terms of these Kraus operators,

$$\hat{\rho}_S(t) = \sum_{n=1}^{n_{eig}} \hat{\mathcal{K}}_n(t) \hat{\rho}_S(0) \hat{\mathcal{K}}_n^\dagger(t). \tag{6.2}$$

Now, inserting the initial density, $\hat{\rho}_S(0) = |\psi(0)\rangle\langle\psi(0)|$, where $|\psi(0)\rangle = (|0\rangle + |1\rangle)/\sqrt{2}$, into the above equation, the CKT for the given temperature, $k_BT = 0.25$ and $n_{eig} = 20$ then has the form,

$$\hat{\rho}_S(t) = \sum_{n=1}^{n_{eig}} p_n \begin{pmatrix} |c_1^n(t)|^2 & c_1^n(t)[c_0^n(t)]^* \\ c_0^n(t)[c_1^n(t)]^* & |c_0^n(t)|^2 \end{pmatrix}, \tag{6.3}$$

where

$$c_1^n(t) = \frac{\sqrt{2}}{2}\left[\cos a_n t + i\frac{(B_z - 2B_{n,n})}{b_n}\sin a_n t\right], \tag{6.4}$$

$$c_0^n(t) = \frac{\sqrt{2}}{2}\left[\cos a_n t - i\frac{(B_z + 2B_{n,n})}{b_n}\sin a_n t\right], \tag{6.5}$$

and

$$a_n = \frac{b_n}{2\hbar} \quad \text{and} \quad b_n = \sqrt{B_z^2 + 4B_{n,n}^2}\,. \tag{6.6}$$

6.1.1 Results for purity and fidelity

The accuracy of the CKD has been tested for several values of intra-bath couplings in the chaotic bath regime, i.e. for $J_x = 0.50, 1.00, 2.00\ \epsilon$. Here, the predictions of the CKD are compared with exact numerical results for the purity, $\mathcal{P}(t)$, and fidelity, $\mathcal{F}(t)$, of the reduced density.

In figure 6.1 for short time dynamics, and in figure 6.2 for long time dynamics, $\mathcal{P}(t)$ is plotted for three different values of intra-bath coupling, J_x. The time is in units of $\hbar/\epsilon$. The red dashed lines are the CKD predictions while the black solid lines represent the exact dynamics. Even for $J_x = 0.50\ \epsilon$, shown in subfigures 6.1(a) and 6.2(a), the decoherence predicted by the CKD is of the correct order of magnitude. However, it is not quantitatively accurate. There is a faster time scale to the exact dynamics which is not captured at all by the CKD. Much better agreement is observed in subfigures 6.1(b) and 6.2(b) where $J_x = 1.00\ \epsilon$ and hence the chaos is stronger. As seen in subfigures 6.1(c)

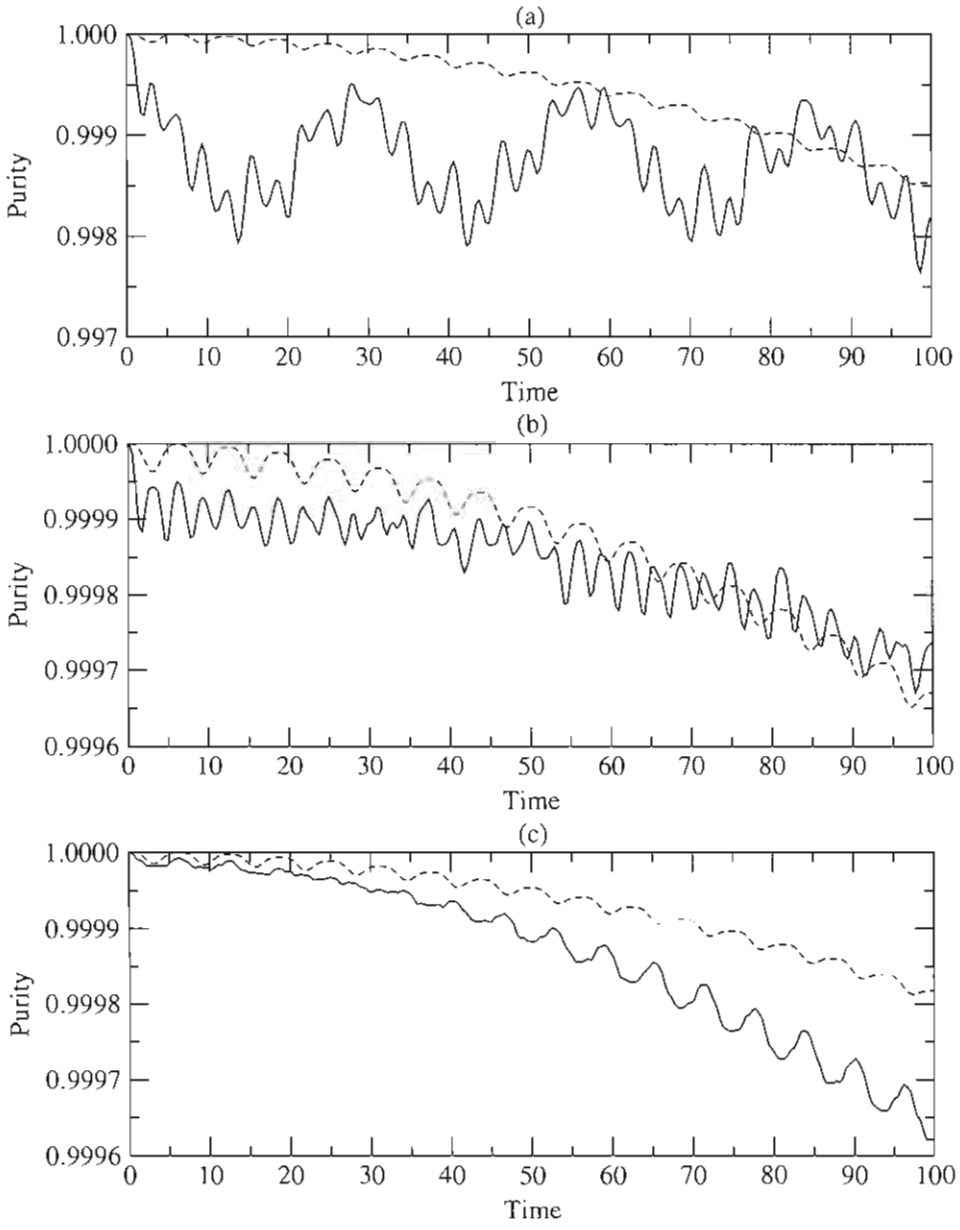

Figure 6.1: Short time dynamics: exact numerical (black solid lines) and CKD (red dashed lines) results for purity, $\mathcal{P}(t)$, plotted in (a) for $J_x = 0.50\ \epsilon$, in (b) for $J_x = 1.00\ \epsilon$, and in (c) for $J_x = 2.00\ \epsilon$.

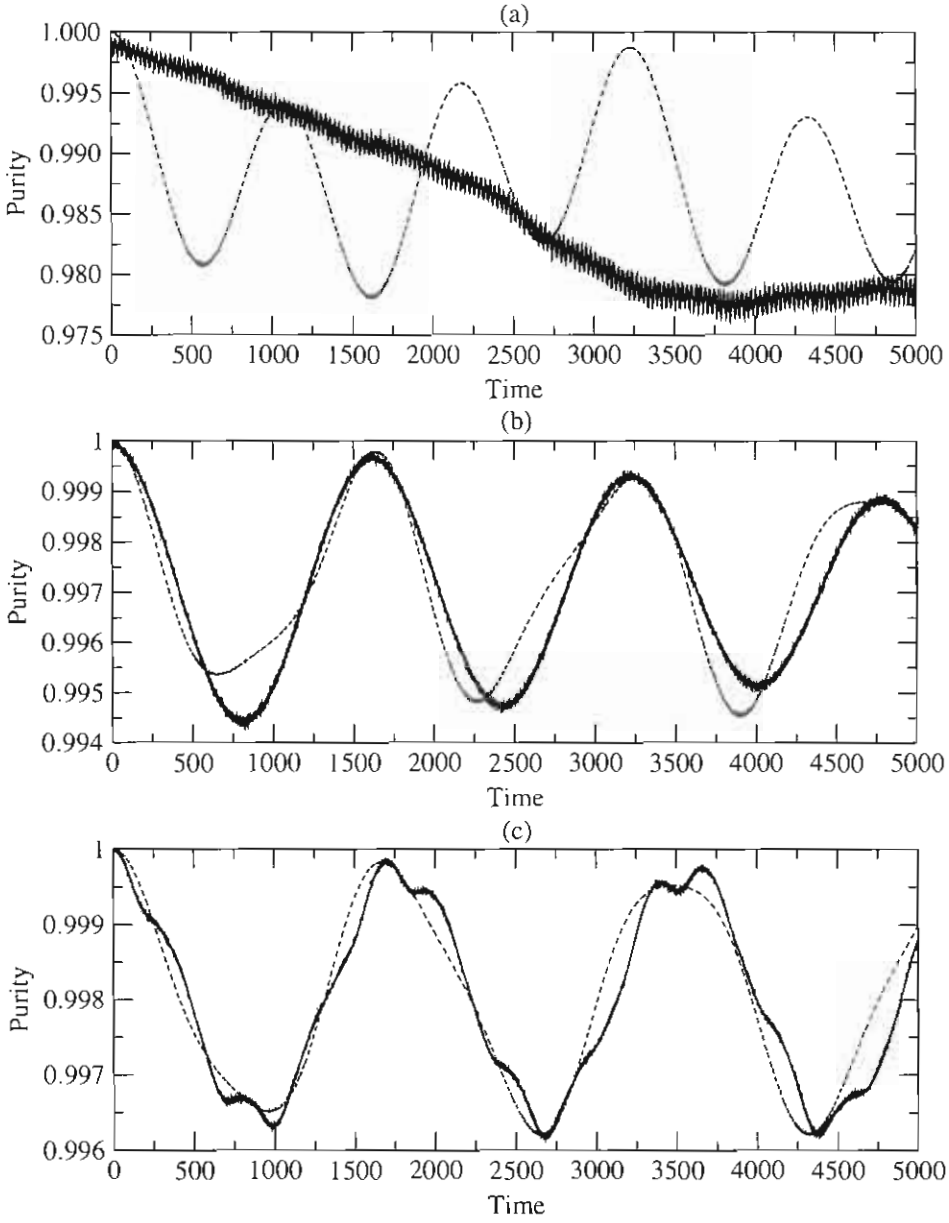

Figure 6.2: Long time dynamics: exact numerical (black solid lines) and CKD (red dashed lines) results for purity, $\mathcal{P}(t)$, plotted in (a) for $J_x = 0.50\ \epsilon$, in (b) for $J_x = 1.00\ \epsilon$, and in (c) for $J_x = 2.00\ \epsilon$.

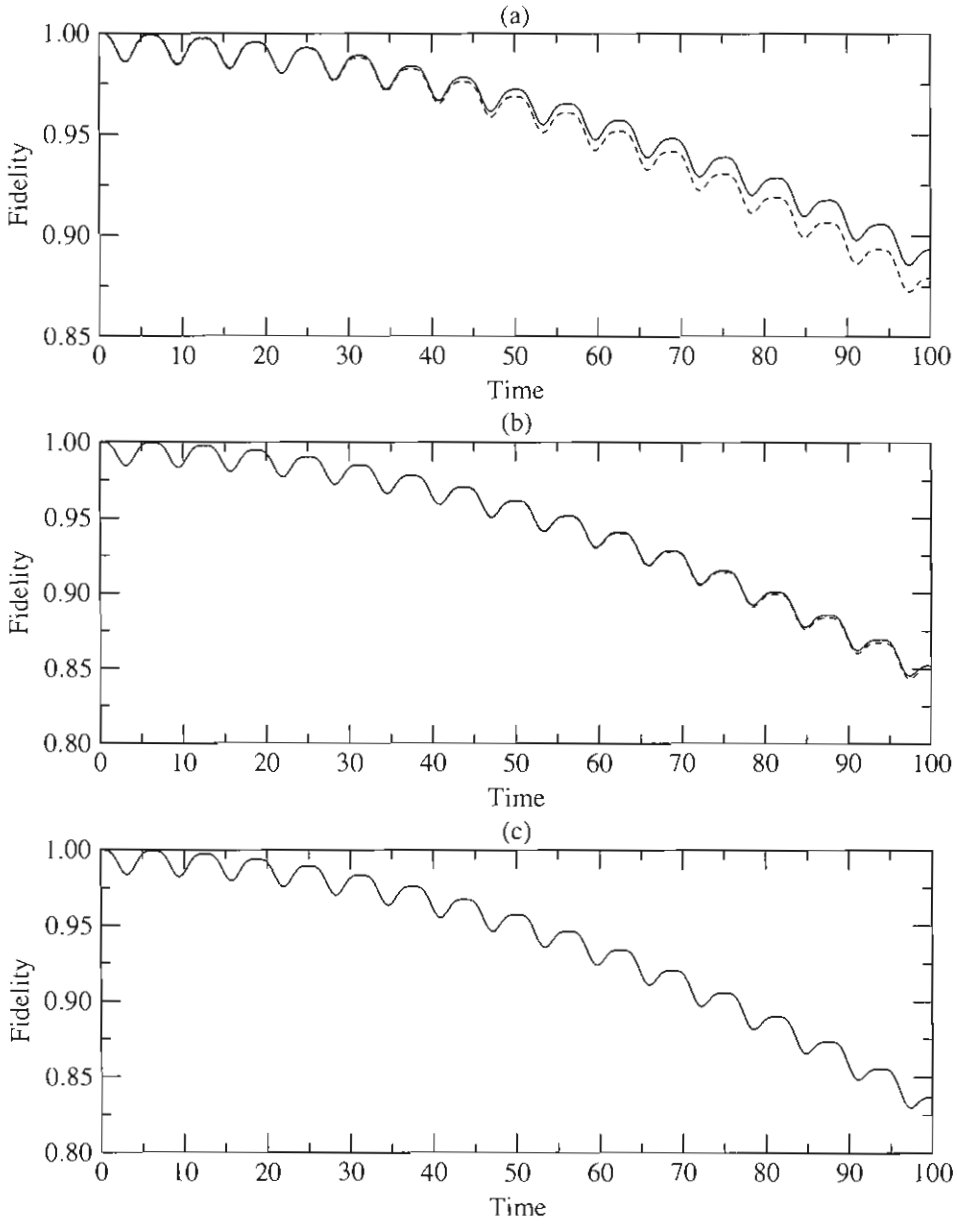

Figure 6.3: Short time dynamics: exact numerical (black solid lines) and CKD (red dashed lines) results for fidelity, $\mathcal{F}(t)$, plotted in (a) for $J_x = 0.50\ \epsilon$, in (b) for $J_x = 1.00\ \epsilon$, and in (c) for $J_x = 2.00\ \epsilon$.

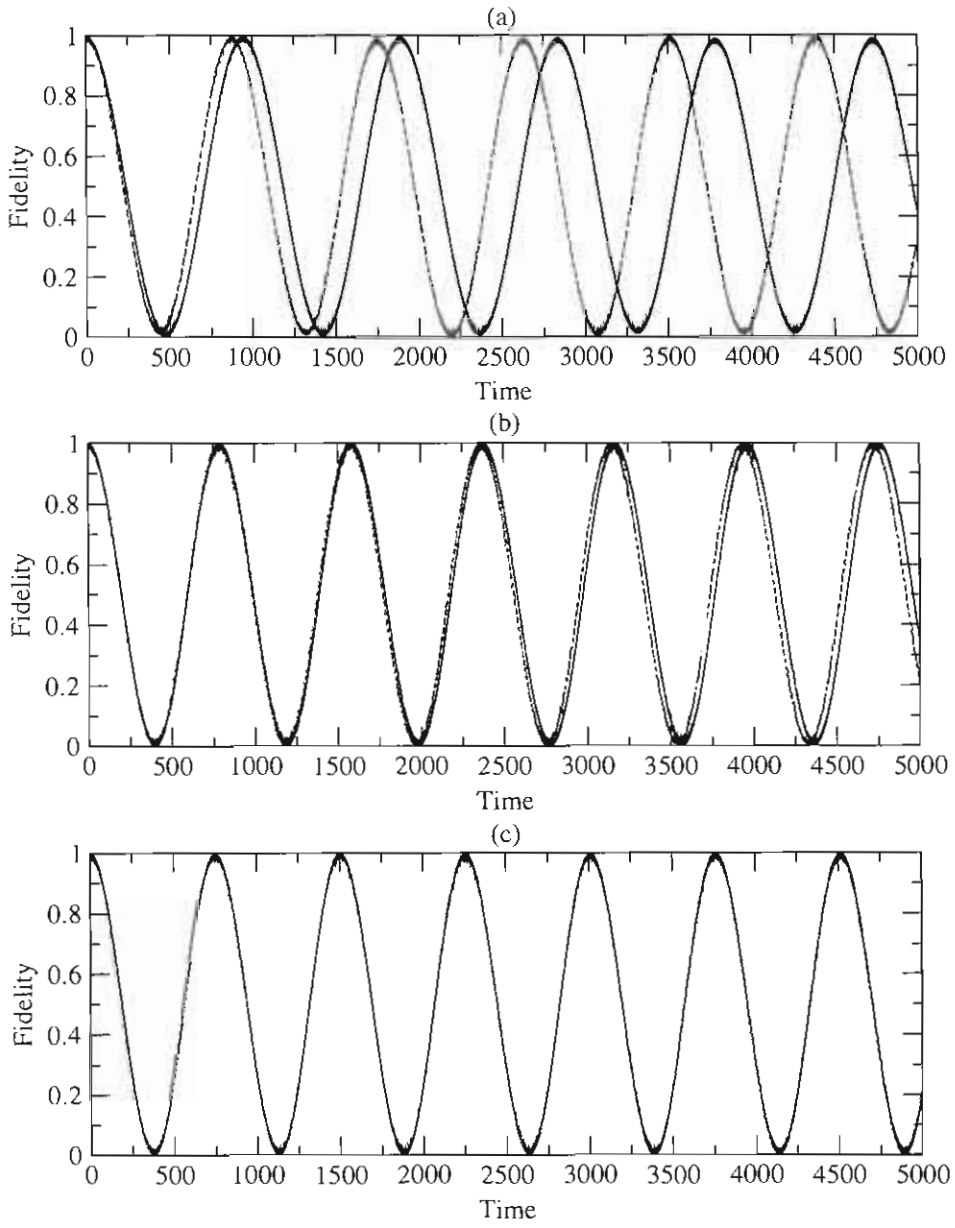

Figure 6.4: Long time dynamics: exact numerical (black solid lines) and CKD (red dashed lines) results for fidelity, $\mathcal{F}(t)$, plotted in (a) for $J_x = 0.50\ \epsilon$, in (b) for $J_x = 1.00\ \epsilon$, and in (c) for $J_x = 2.00\ \epsilon$.

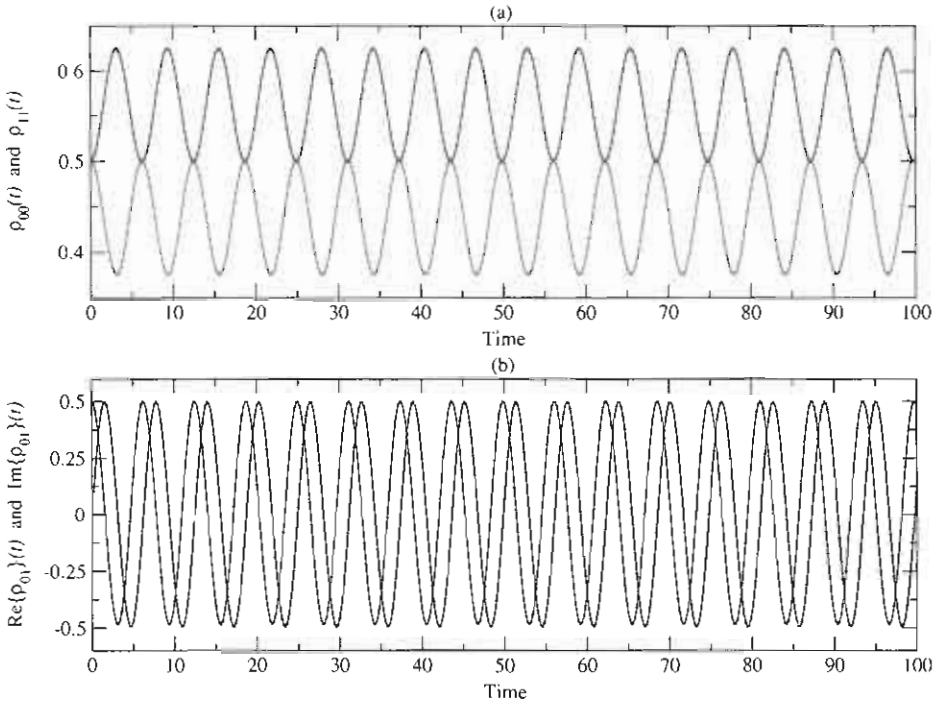

Figure 6.5: Short time dynamics of matrix elements of snbsystem density, $\hat{\rho}_S(t)$, for $J_x = 1.00\ \epsilon$: Exact numerical results are given by solid lines and CKD results by dotted lines. (a) Diagonals of $\hat{\rho}_S(t)$, $\langle 0|\hat{\rho}_S(t)|0\rangle$ (green) and $\langle 1|\hat{\rho}_S(t)|1\rangle$ (red). (b) Real part of off-diagonal element of $\hat{\rho}_S(t)$, $\mathrm{Re}\{\langle 0|\hat{\rho}_S(t)|1\rangle\}$ (black) and imaginary part of off-diagonal of $\hat{\rho}_S(t)$, $\mathrm{Im}\{\langle 0|\hat{\rho}_S(t)|1\rangle\}$ (blue).

and 6.2(c), for the strongest chaotic case, i.e. $J_x = 2.00\ \epsilon$, the CKD results are in very good agreement with the exact results.

In figure 6.3 for short time dynamics, and in figure 6.4 for long time dynamics, $\mathcal{F}(t)$ is plotted for both exact and CKD results for the same three different values of intra-bath coupling J_x. The magnitudes of the errors in $\mathcal{F}(t)$ are much larger than those in $\mathcal{P}(t)$. The purity measures only non-unitary errors but the fidelity is also sensitive to unitary errors. The large deviation of $\mathcal{F}(t)$ from $\mathcal{P}(t)$ therefore indicates the presence of a large coherent shift. The agreement between the CKD and exact results is quite good even for $J_x = 0.50\ \epsilon$, shown in subfigures 6.3(a) and 6.4(a). For $J_x = 1.00\ \epsilon$, shown in subfigures 6.3(b) and 6.4(b), the agreements are very good. For $J_x = 2.00\ \epsilon$,the agreements seen in subfigures 6.3(c)

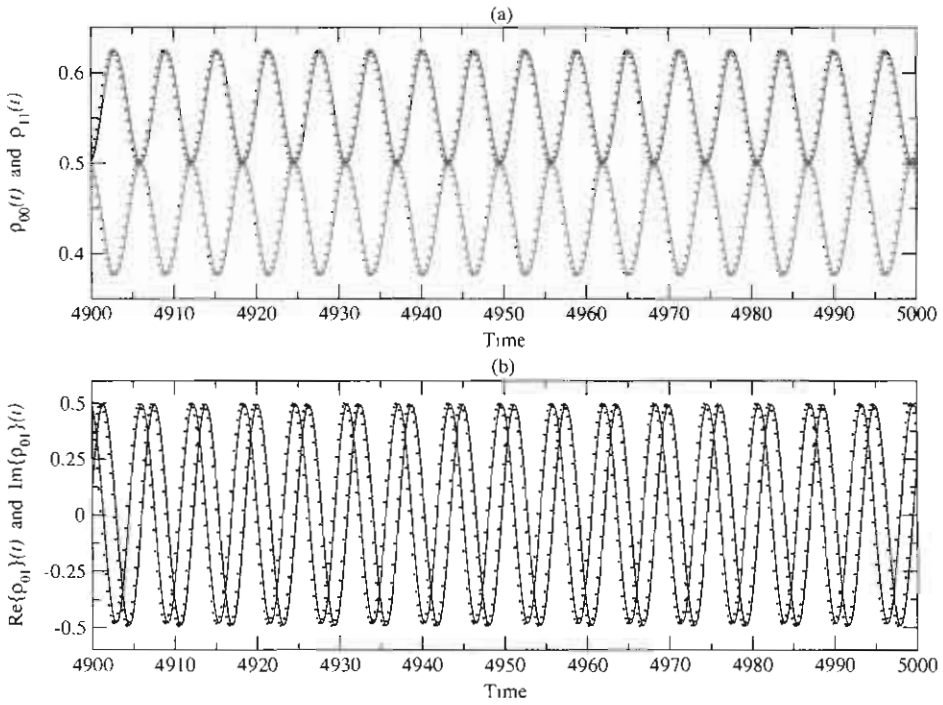

Figure 6.6: Long time dynamics of matrix elements of subsystem density, $\hat{\rho}_S(t)$, for $J_x = 1.00\ \epsilon$: Exact numerical results are given by solid lines and CKD results by dotted lines. (a) Diagonals of $\hat{\rho}_S(t)$, $\langle 0|\hat{\rho}_S(t)|0\rangle$ (green) and $\langle 1|\hat{\rho}_S(t)|1\rangle$ (red). (b) Real part of off-diagonal element of $\hat{\rho}_S(t)$, $\mathrm{Re}\{\langle 0|\hat{\rho}_S(t)|1\rangle\}$ (black) and imaginary part of off-diagonal of $\hat{\rho}_S(t)$, $\mathrm{Im}\{\langle 0|\hat{\rho}_S(t)|1\rangle\}$ (blue).

and 6.4(c) are excellent where the Kraus and exact results almost completely overlap.

6.1.2 Results for reduced density matrix elements

In this section, the matrix elements of reduced density predicted by the CKD are compared to those obtained by exact numerical simulations. The matrix elements are plotted for the short time dynamics in figure 6.5, and for the long time dynamics in figure 6.6 for $J_x = 1.00\ \epsilon$. In subfigures 6.5(a) and 6.6(a), the populations of reduced density and in subfigures 6.5(b) and 6.6(b), the off-diagonal matrix elements are plotted. In all these figures, the exact results are plotted with solid lines and the CKD results are plotted with dotted lines.

Matrix element plots show a high degree of accuracy in all cases. Indeed, the CKD

results are virtually indistinguishable from the exact results. This is true for short as well as long time dynamics. Similar degrees of accuracy are also obtained for other intra–coupling values, $J_x = 0.50\ \epsilon$ and $J_x = 2.00\ \epsilon$, not reported here. This high degree of accuracy is remarkable given that the bath contains only ten qubits. Moreover, it suggests that the CKD can actually be employed as a useful computational method for low temperature simulations of open system dynamics where the new quantum technologies are expected to operate.

6.2 CNOT study

In this section, the test results for the CNOT study of chapter 4 are presented. Analytic solutions for the CKD should be readily obtainable due to the low dimension of the CNOT system. However, an alternative numerical strategy was employed here, as is outlined in section 2.7. While this approach is also generally applicable for any subsystem state, it is even more straightforward for pure initial system states, as is the case for the CNOT study.

The first step in the numerical strategy is to construct the effective system Hamiltonians for the Kraus operators by using the original system Hamiltonians and coherent shift terms:

$$\hat{H}_{\text{eff}}(t) = \hat{H}_S(t) + \Sigma_\alpha^{n,n}(\hat{\sigma}_\alpha^{(1)} + \hat{\sigma}_\alpha^{(2)}) \tag{6.7}$$

where $\alpha \in \{x, z\}$ stands for xx- and zz-type coupling, respectively. The subsystem Hamiltonians, $\hat{H}_S(t)$, and corresponding switching times for the CNOT gate are given in table 3.1. Here, $\Sigma_\alpha^{n,n}(\hat{\sigma}_\alpha^{(1)} + \sigma_\alpha^{(2)})$ are the coherent shift terms. More specifically, $(\hat{\sigma}_\alpha^{(1)} + \sigma_\alpha^{(2)})$ are the system coupling operators and $\Sigma_\alpha^{n,n} = \langle\phi_n^B|\hat{\Sigma}_\alpha|\phi_n^B\rangle$ are the diagonal matrix elements of the bath coupling operators in the complete bath eigenbasis, i.e. $\hat{H}_B|\phi_n^B\rangle = E_n|\phi_n^B\rangle$. A summary of the effective system Hamiltonians can be found in table 6.1. In the numerical calculations, $n_{eig} = 20$ low lying exact bath eigenstates $|\phi_n^B\rangle$ are used to calculate $\Sigma_\alpha^{n,n}$ terms for $J_x = 0.50, 1.00, 2.00\ \epsilon$.

Given the effective system Hamiltonians for the CNOT gate, the time–evolved dynamics

Table 6.1: Switching times and Hamiltonians including coherent shift terms used to implement the CNOT gate by the CKD.

Switching Intervals	Effective Hamiltonian
$[t_0 = 0, t_1 = \pi/(2\mathcal{B}^z)]$	$-\frac{1}{2}\mathcal{B}^z\hat{\sigma}_z^{(2)} + \Sigma_\alpha^{n,n}(\hat{\sigma}_\alpha^{(1)} + \hat{\sigma}_\alpha^{(2)})$
$[t_1, t_2 = t_1 + \pi/(2\mathcal{B}^x)]$	$-\frac{1}{2}\mathcal{B}^x\hat{\sigma}_x^{(2)} + \Sigma_\alpha^{n,n}(\hat{\sigma}_\alpha^{(1)} + \hat{\sigma}_\alpha^{(2)})$
$[t_2, t_3 = t_2 + \pi/(2\mathcal{B}^z)]$	$+\frac{1}{2}\mathcal{B}^z\hat{\sigma}_z^{(2)} + \Sigma_\alpha^{n,n}(\hat{\sigma}_\alpha^{(1)} + \hat{\sigma}_\alpha^{(2)})$
$[t_3, t_4 = t_3 + \sqrt{2}\pi/(2\mathcal{B}^z)]$	$-\frac{1}{2}\mathcal{B}^z\sum_{i=1}^{2}(\hat{\sigma}_z^{(i)} + \hat{\sigma}_x^{(i)}) + \Sigma_\alpha^{n,n}(\hat{\sigma}_\alpha^{(1)} + \hat{\sigma}_\alpha^{(2)})$
$[t_4, t_5 = t_4 + \pi/(4\mathcal{J}_x)]$	$\mathcal{J}_x(-\hat{\sigma}_x^{(1)} - \hat{\sigma}_x^{(2)} + \hat{\sigma}_x^{(1)}\hat{\sigma}_x^{(2)}) + \Sigma_\alpha^{n,n}(\hat{\sigma}_\alpha^{(1)} + \hat{\sigma}_\alpha^{(2)})$
$[t_5, t_6 = t_5 + \sqrt{2}\pi/(2\mathcal{B}^z)]$	$+\frac{1}{2}\mathcal{B}^z\sum_{i=1}^{2}(\hat{\sigma}_z^{(i)} + \hat{\sigma}_x^{(i)}) + \Sigma_\alpha^{n,n}(\hat{\sigma}_\alpha^{(1)} + \hat{\sigma}_\alpha^{(2)})$
$[t_6, t_7 = t_6 + \pi/(2\mathcal{B}^z)]$	$-\frac{1}{2}\mathcal{B}^z\hat{\sigma}_z^{(2)} + \Sigma_\alpha^{n,n}(\hat{\sigma}_\alpha^{(1)} + \hat{\sigma}_\alpha^{(2)})$
$[t_7, t_8 = t_7 + \pi/(2\mathcal{B}^x)]$	$+\frac{1}{2}\mathcal{B}^x\hat{\sigma}_x^{(2)} + \Sigma_\alpha^{n,n}(\hat{\sigma}_\alpha^{(1)} + \hat{\sigma}_\alpha^{(2)})$
$[t_8, t_9 = t_8 + \pi/(2\mathcal{B}^z)]$	$+\frac{1}{2}\mathcal{B}^z\hat{\sigma}_z^{(2)} + \Sigma_\alpha^{n,n}(\hat{\sigma}_\alpha^{(1)} + \hat{\sigma}_\alpha^{(2)})$

for each bath eigenstate, $\{|\phi_n^B\rangle\}$ with $n = 1, ..., n_{eig} = 20$, can be calculated by numerical solutions of the Schrödinger equation,

$$d|\psi_n(t)\rangle/dt = -(i/\hbar)\hat{H}_{\text{eff}}(t)|\psi_n(t)\rangle. \tag{6.8}$$

The Schrödinger equation is solved for two sets of eight initial states. The first set consists of standard basis states, i.e. $|\psi_0\rangle \in \{|00\rangle, |01\rangle, |10\rangle, |11\rangle\}$, and the second set includes the Bell states, i.e. $'\psi_0\rangle \in \{(|00\rangle \pm |11\rangle)/\sqrt{2}, (|01\rangle \pm |10\rangle)/\sqrt{2}\}$.

In the following the time–evolved redneed density for each initial condition is constructed via

$$\hat{\rho}_S(t) = \sum_n^{n_{eig}} p_n|\psi_n(t)\rangle\langle\psi_n(t)|, \tag{6.9}$$

where $p_n = \exp(-E_n/k_BT)/\sum_{m=1}^{n_{eig}}\exp(-E_m/k_BT)$ are the initial bath populations.

The CKD requires exact bath eigenstates in the calculations of the $B_\mu^{n,n}$ terms. Exact diagonalization of the bath Hamiltonian should be easy to achieve for quite large bath

dimensions by standard matrix diagonalization routines. In cases when the bath dimension is too large and thus exact diagonalization is impossible, such as large coupled oscillator baths, alternative approaches may be taken to calculate $B_\mu^{n,n}$ and E_n. For example, quantum-semi-classical molecular dynamics simulations can prove very useful to calculate $B_\mu^{n,n}$ terms. Perhaps, the Wigner method [46] would suffice to calculate $B_\mu^{n,n}$ once the E_n are known. These approaches are not within the scope of this thesis and will be investigated elsewhere.

6.2.1 Results for average purity and fidelity

In this section, the accuracy of the CKD is tested by comparing the predictions of the CKD with those of exact results for average purity, $\bar{\mathcal{P}}(t)$, and fidelity, $\bar{\mathcal{F}}(t)$. Definition of these error quantifiers can be found in section 3.4.1.

The average purity, $\bar{\mathcal{P}}(t)$, is plotted for xx-type coupling, the generator of bit-flip errors, in figure 6.7 and for zz-type coupliug, the generator of phase errors, in figure 6.8 for three different values of intra-bath coupling in the chaotic regime, i.e. $J_x = 0.50, 1.00, 2.00\ \epsilon$. The exact nnmerical results are represented by solid lines and the CKD results are given by dotted lines, and each coupling value J_x is assigned to the same color and line convention throughout. Results for the standard basis states and Bell states are shown in subfigures (a) and (b), respectively. Switching times of elementary gate operations are also indicated by the grid lines.

All purity figures for both type couplings indicate that decoherence and dissipation result in a purity decay of less than 1 % over the course of the CNOT gate. For xx-type system-bath coupling, subfigure 6.7(a) shows excellent quantitative agreement between the exact and CKD for the most chaotic case of $J_x = 2.00\ \epsilon$. For $J_x = 1.00\ \epsilon$, the agreement is also good with errors in the purity of less than 0.05 %. For the least chaotic case of $J_x = 0.50\ \epsilon$, the discrepancy is on the order of 0.2 %. Overall, these results are surprisingly accurate for the small bath. The results for Bell states presented in subfigure 6.7(b) also show the same

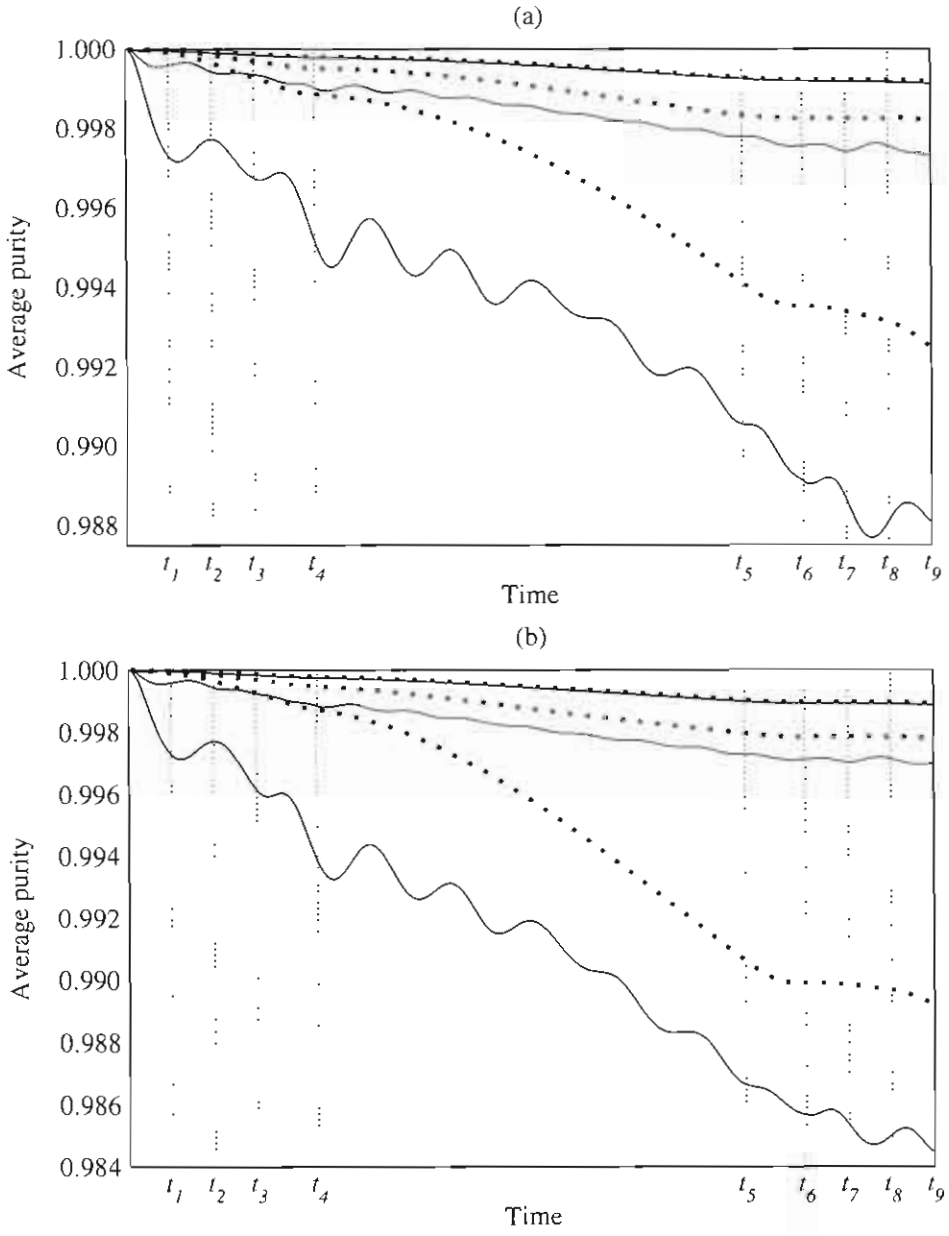

Figure 6.7: Exact numerical (solid lines) and CKD (dotted lines) results for averaged purity, $\mathcal{P}(t)$, iu the case of xx-type coupling for $J_x = 0.50\ \epsilon$ (black), $J_x = 1.00\ \epsilon$ (red), and $J_x = 2.00\ \epsilon$ (blue). (a) Standard basis states and (b) Bell states.

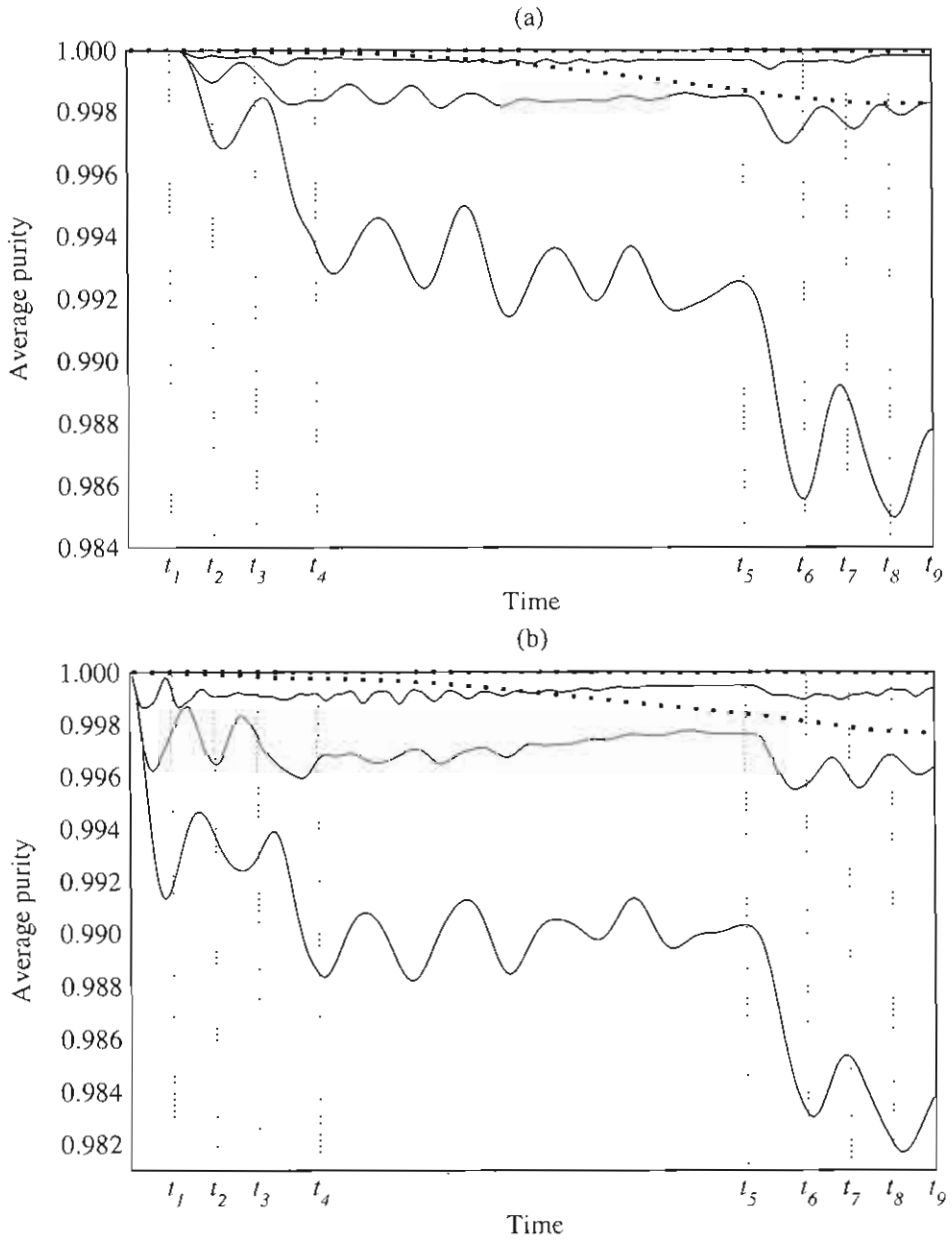

Figure 6.8: Exact numerical (solid lines) and CKD (dotted lines) results for averaged purity, $\mathcal{P}(t)$, in the case of zz-type conpling for $J_x = 0.50\ \epsilon$ (black), $J_x = 1.00\ \epsilon$ (red), and $J_x = 2.00\ \epsilon$ (blue). (a) Standard basis states and (b) Bell states.

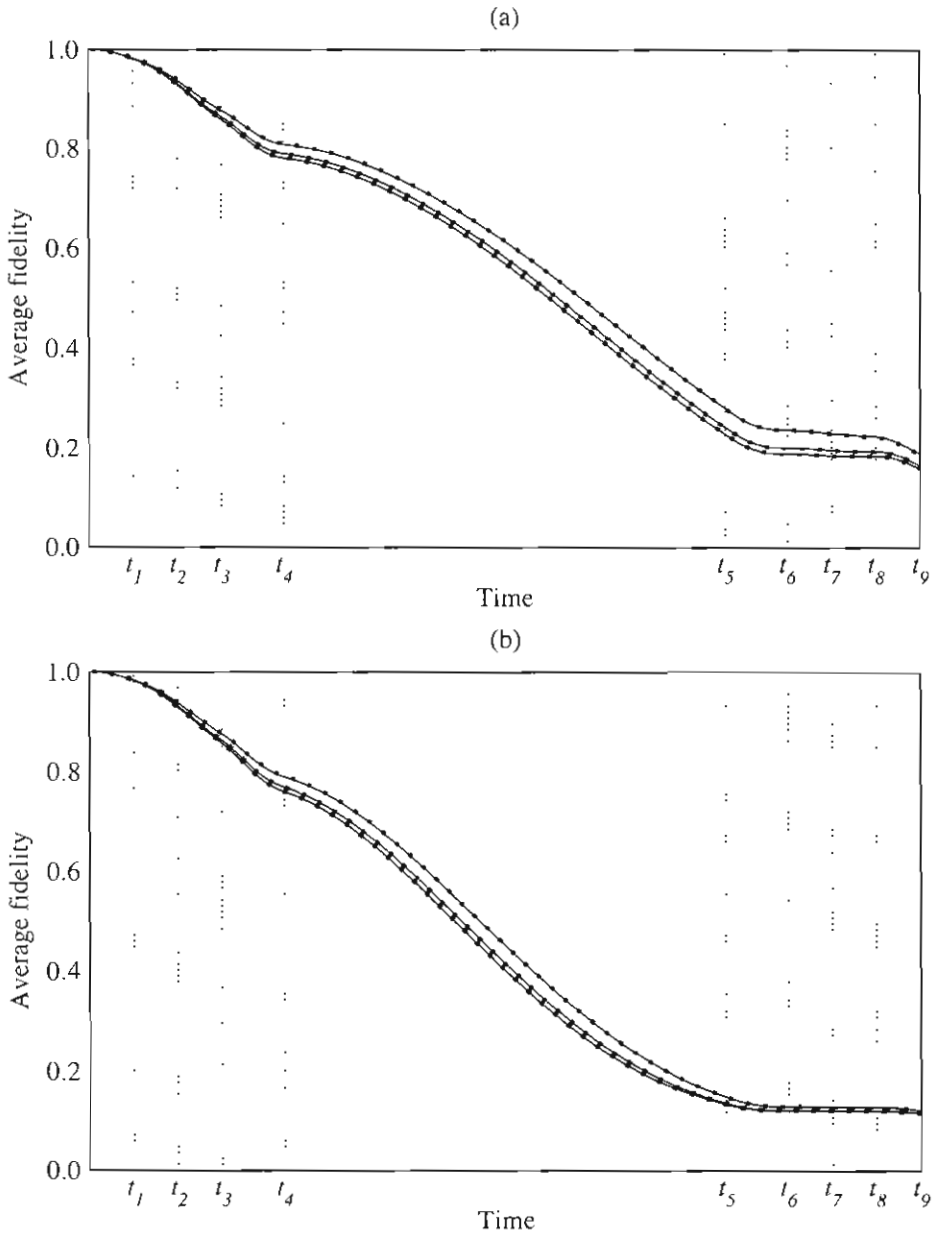

Figure 6.9: Exact numerical (solid lines) and CKD (dotted lines) results for averaged fidelity, $\mathcal{F}(t)$, in the case of xx-type coupling for $J_x = 0.50\ \epsilon$ (black), $J_x = 1.00\ \epsilon$ (red), and $J_x = 2.00\ \epsilon$ (blue). (a) Standard basis states and (b) Bell states.

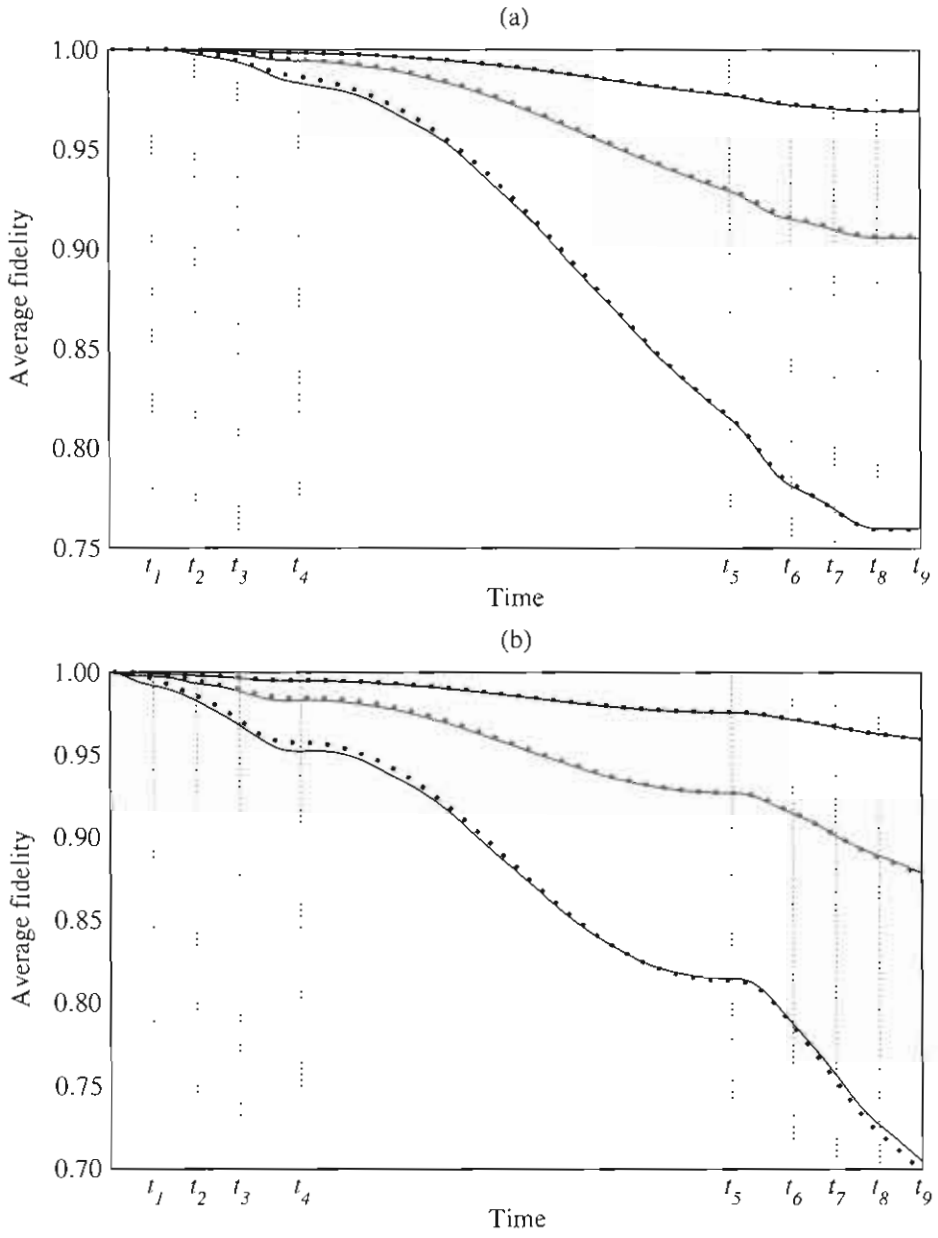

Figure 6.10: Exact numerical (solid lines) and CKD (dotted lines) results for averaged fidelity, $\mathcal{F}(t)$, in the case of zz-type coupling for $J_x = 0.50\ \epsilon$ (black), $J_x = 1.00\ \epsilon$ (red), and $J_x = 2.00\ \epsilon$ (blue). (a) Standard basis states and (b) Bell states.

degree of high accuracy obtained for standard basis states.

For zz-type system-bath coupling, subfigure 6.8(a) shows quite low accuracy as compared to the xx-type system-bath coupling cases seen in subfigure 6.7(a). The overall exact decay of purity for all couplings is comparable, but the CKD discrepancies for $J_x = 2.00\ \epsilon$ are on the order of 0.1 %, while those for $J_x = 1.00\ \epsilon$ are about 0.2 %. For $J_x = 0.50\ \epsilon$, the error is of order 2 %, which is significant but is still not catastrophic. Subfigure 6.8(b) for Bell states again shows the same degree of accuracy as seen in subfigure 6.8(a) for standard basis states.

The average fidelity, $\bar{\mathcal{F}}(t)$, is plotted for xx-type coupling in figure 6.9 and for zz-type coupling in figure 6.10, for the same J_x values. Here, a perfect agreement between the exact and CKD predictions is seen for all states, for all J_x values, and for all couplings. This degree of accuracy is remarkable since these errors are now very large. The fidelity in figure 6.9 decays to 10 % of its initial value, while that in figure 6.10 decays to 70 % of its initial value. The average fidelity of figure 6.9 for xx-type coupling shows almost no sensitivity to J_x, while that in figure 6.10 for zz-type coupling varies snbstantially with J_x. The CKD captures both of these effects. The large magnitude of the fidelity decay in both cases is duc to a coherent shifting of the subsystem dynamics.

6.2.2 Results for reduced density matrix elements

The purity and fidelity suffice for an overall identification of the magnitudes of non-unitary and unitary errors. The comparison of ideal and actual reduced density matrix elements, however, provides further valuable information on what actually goes wrong during the implementation of an algorithm. Here, as a generic representation of the results, a comparison of the matrix elements for two initial subsystem states is presented; $|11\rangle$ is representative of the standard basis states, and $(|00\rangle + |11\rangle)/\sqrt{2}$ is representative of Bell states. Both xx-type and zz-type couplings for $J_x = 1.00\ \epsilon$ are considered.

The matrix elements are compared for xx-type coupling in figure 6.11 and for zz-type coupling in figure 6.12 for the initial state $|11\rangle$. In these and subsequent figures, the coherent (i.e. error-free) time evolution is given by black solid lines. Exact time evolutions are plotted by solid green lines, and the CKD results are given by dashed red lines.

Each subfigure represents a different matrix element. The specific matrix elements plotted in each subfigure are as follows: $\rho_{00}^{(1)}(t) = \langle 0|\mathrm{Tr}_2[\hat{\rho}_S(t)]|0\rangle$ is plotted in subfigure (a), $\rho_{11}^{(1)}(t) = \langle 1|\mathrm{Tr}_2[\hat{\rho}_S(t)]|1\rangle$ in (b), $\mathrm{Re}\{\rho_{01}^{(1)}(t)\} = \mathrm{Re}\{\langle 0|\mathrm{Tr}_2[\hat{\rho}_S(t)]|1\rangle\}$ in (c) and $\mathrm{Im}\{\rho_{01}^{(1)}(t)\} = \mathrm{Im}\{\langle 0|\mathrm{Tr}_2[\hat{\rho}_S(t)]|1\rangle\}$ in (d). Similarly, $\rho_{00}^{(2)}(t) = \langle 0|\mathrm{Tr}_1[\hat{\rho}_S(t)]|0\rangle$ is plotted in subfigure (e), $\rho_{11}^{(2)}(t) = \langle 1|\mathrm{Tr}_1[\hat{\rho}_S(t)]|1\rangle$ in (f), $\mathrm{Re}\{\rho_{01}^{(2)}(t)\} = \mathrm{Re}\{\langle 0|\mathrm{Tr}_1[\hat{\rho}_S(t)]|1\rangle\}$ in (g), and $\mathrm{Im}\{\rho_{01}^{(2)}(t)\} = \mathrm{Im}\{\langle 0|\mathrm{Tr}_1[\hat{\rho}_S(t)]|1\rangle\}$ in (h).

The agreement between the exact and CKD results is excellent in all cases. The deviations from the coherent time evolution are large in all cases, while the discrepancies between the exact and CKD results are basically negligible. The worst deviations are again seen in the zz-type coupling case, but these are still very small.

The results are shown for the matrix elements for the initial Bell state $(|00\rangle + |11\rangle)/\sqrt{2}$ in figure 6.13 for xx-type coupling and in figure 6.14 for zz-type coupling. The agreement between the exact and the CKD predictions is again very good. The only visible deviations arise from zz-type conpling cases. See, for example, subfigure 6.14(a) and subfigure 6.14(c) where some small deviations are seen.

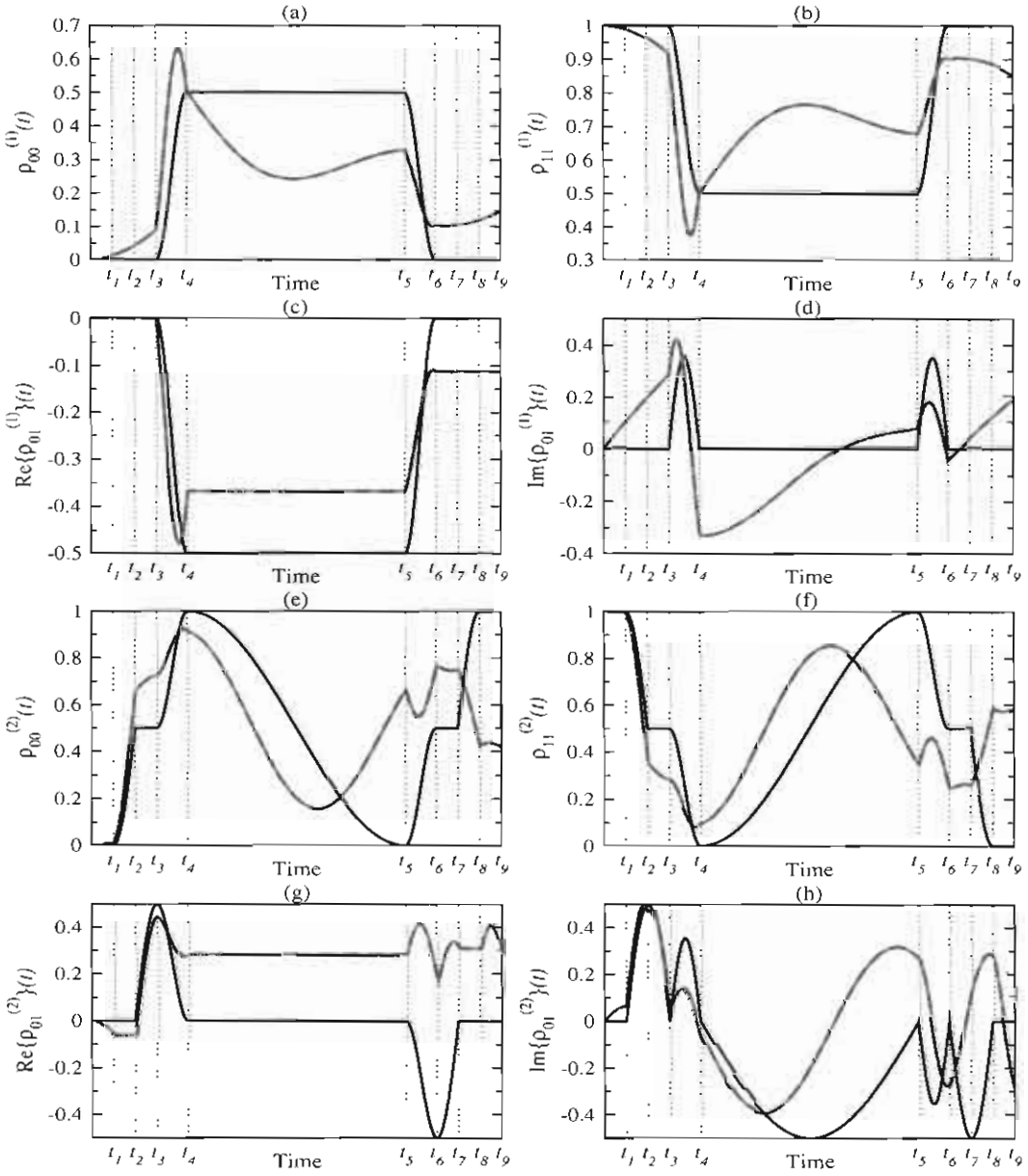

Figure 6.11: Exact numerical (solid green lines) and CKD (dashed red lines) results for matrix elements of reduced density of first and second qubits in the case of xx-type coupling. Error–free time evolution is given by a solid black line. The initial state of the system is $|11\rangle$ and the intra-bath coupling $J_x = 1.00\ \epsilon$. $\rho_{00}^{(1)}(t)$ plotted in subfigure (a), $\rho_{11}^{(1)}(t)$ in (b), $\mathrm{Re}\{\rho_{01}^{(1)}(t)\}$ in (c), and $\mathrm{Im}\{\rho_{01}^{(1)}(t)\}$ in (d), $\rho_{00}^{(2)}(t)$ in (e), $\rho_{11}^{(2)}(t)$ in (f), $\mathrm{Re}\{\rho_{01}^{(2)}(t)\}$ in (g), and $\mathrm{Im}\{\rho_{01}^{(2)}(t)\}$ in (h).

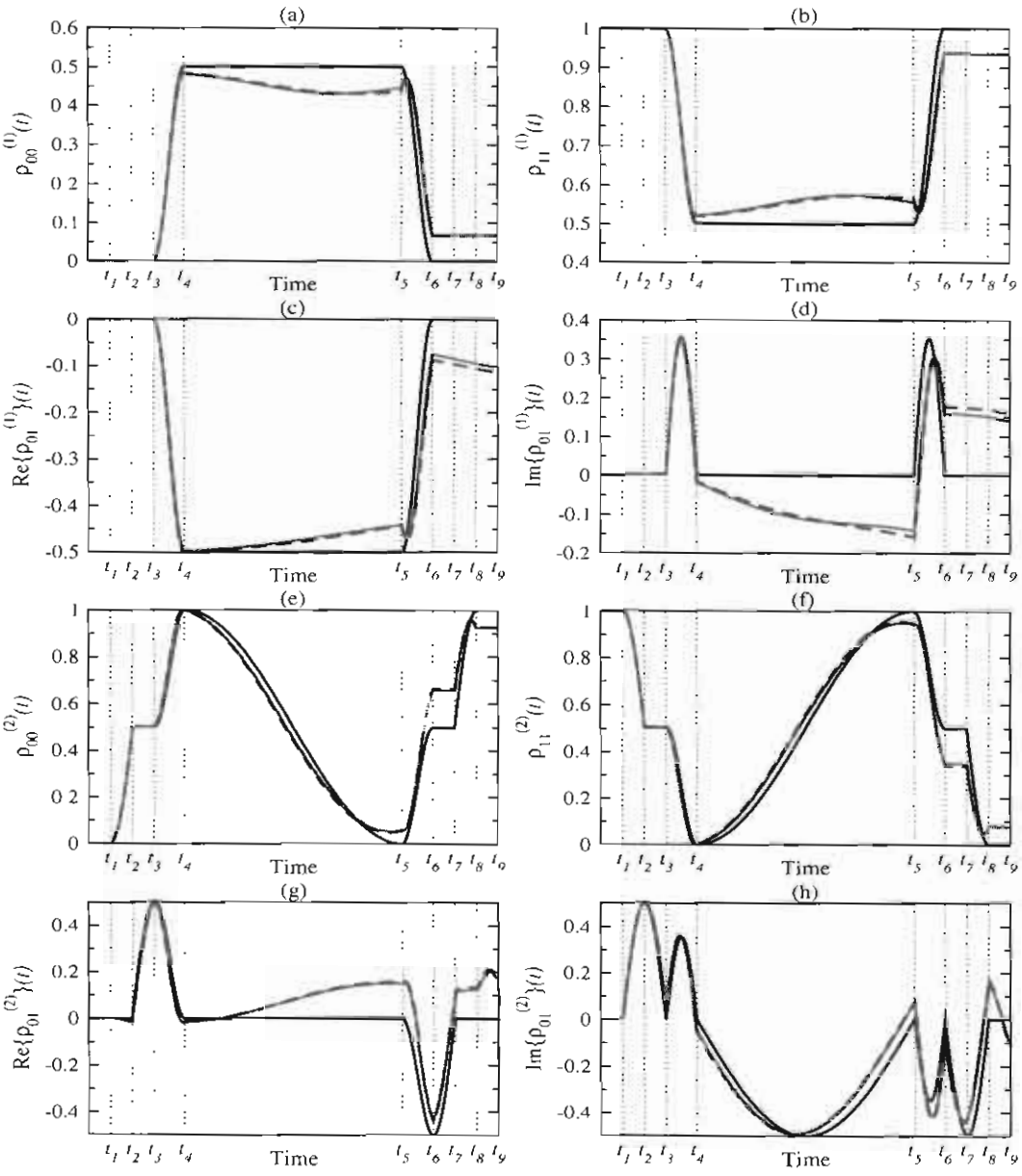

Figure 6.12: Exact numerical (solid green lines) and CKD (dashed red lines) results for matrix elements of reduced density of first and second qubits in the case of zz-type coupling. Coherent time evolution is given by a solid black line. The initial state of the system is $|11\rangle$ and the intra-bath coupling $J_x = 1.00\ \epsilon$. $\rho_{00}^{(1)}(t)$ plotted in subfigure (a), $\rho_{11}^{(1)}(t)$ in (b), $\mathrm{Re}\{\rho_{01}^{(1)}(t)\}$ in (c), and $\mathrm{Im}\{\rho_{01}^{(1)}(t)\}$ in (d), $\rho_{00}^{(2)}(t)$ in (e), $\rho_{11}^{(2)}(t)$ in (f), $\mathrm{Re}\{\rho_{01}^{(2)}(t)\}$ in (g), and $\mathrm{Im}\{\rho_{01}^{(2)}(t)\}$ in (h).

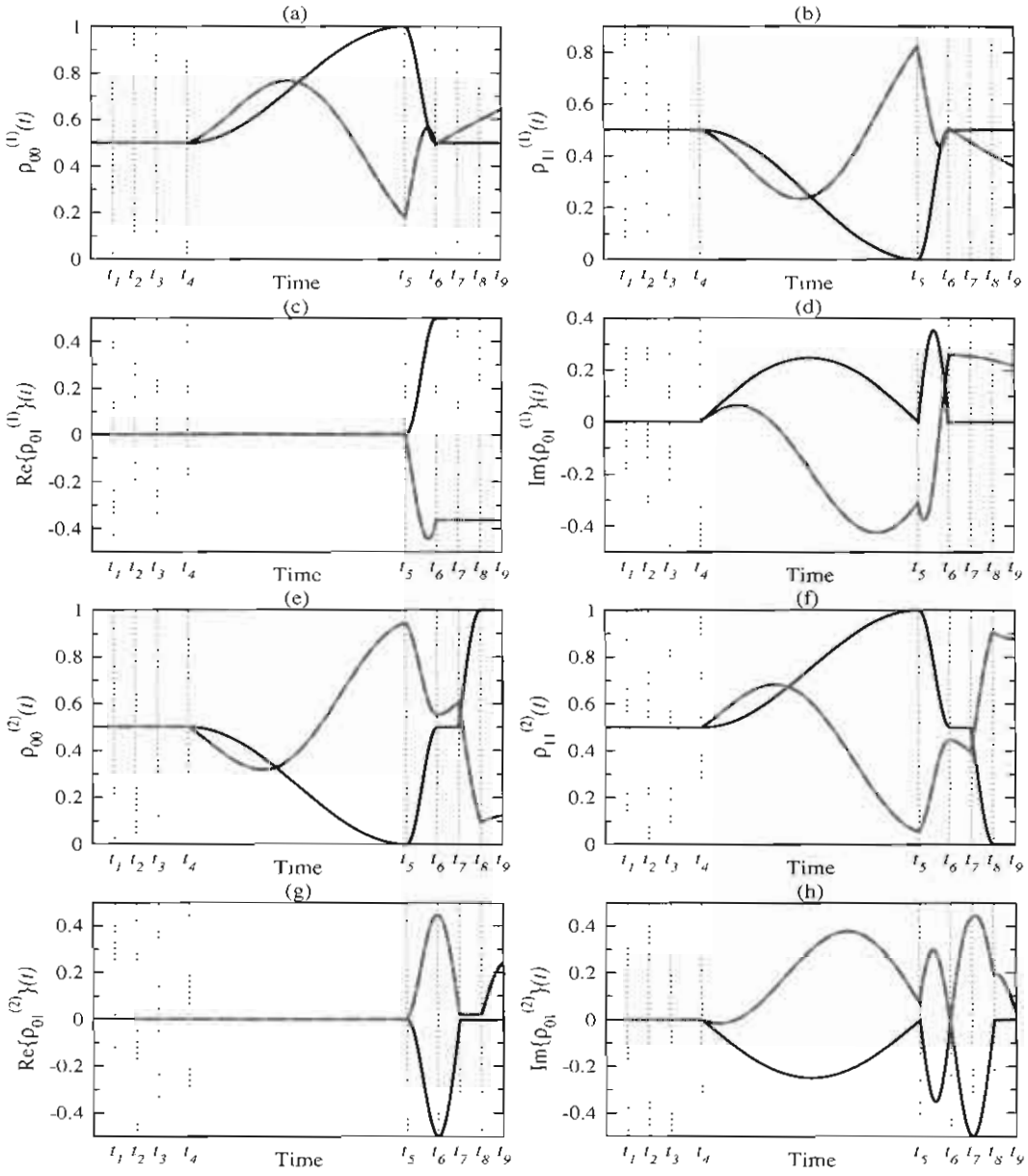

Figure 6.13: Exact numerical (solid green lines) and CKD (dashed red lines) results for matrix elements of reduced density of first and second qubits in the case of xx-type coupling. Coherent time evolution is given by a solid black line. The initial state of the system is a Bell state of the form $(|00\rangle + |11\rangle)/\sqrt{2}$ and the intra-bath coupling $J_x = 1.00\ \epsilon$. $\rho_{00}^{(1)}(t)$ plotted in subfigure (a), $\rho_{11}^{(1)}(t)$ in (b), $\mathrm{Re}\{\rho_{01}^{(1)}(t)\}$ in (c), and $\mathrm{Im}\{\rho_{01}^{(1)}(t)\}$ in (d), $\rho_{00}^{(2)}(t)$ in (e), $\rho_{11}^{(2)}(t)$ in (f), $\mathrm{Re}\{\rho_{01}^{(2)}(t)\}$ in (g), and $\mathrm{Im}\{\rho_{01}^{(2)}(t)\}$ in (h).

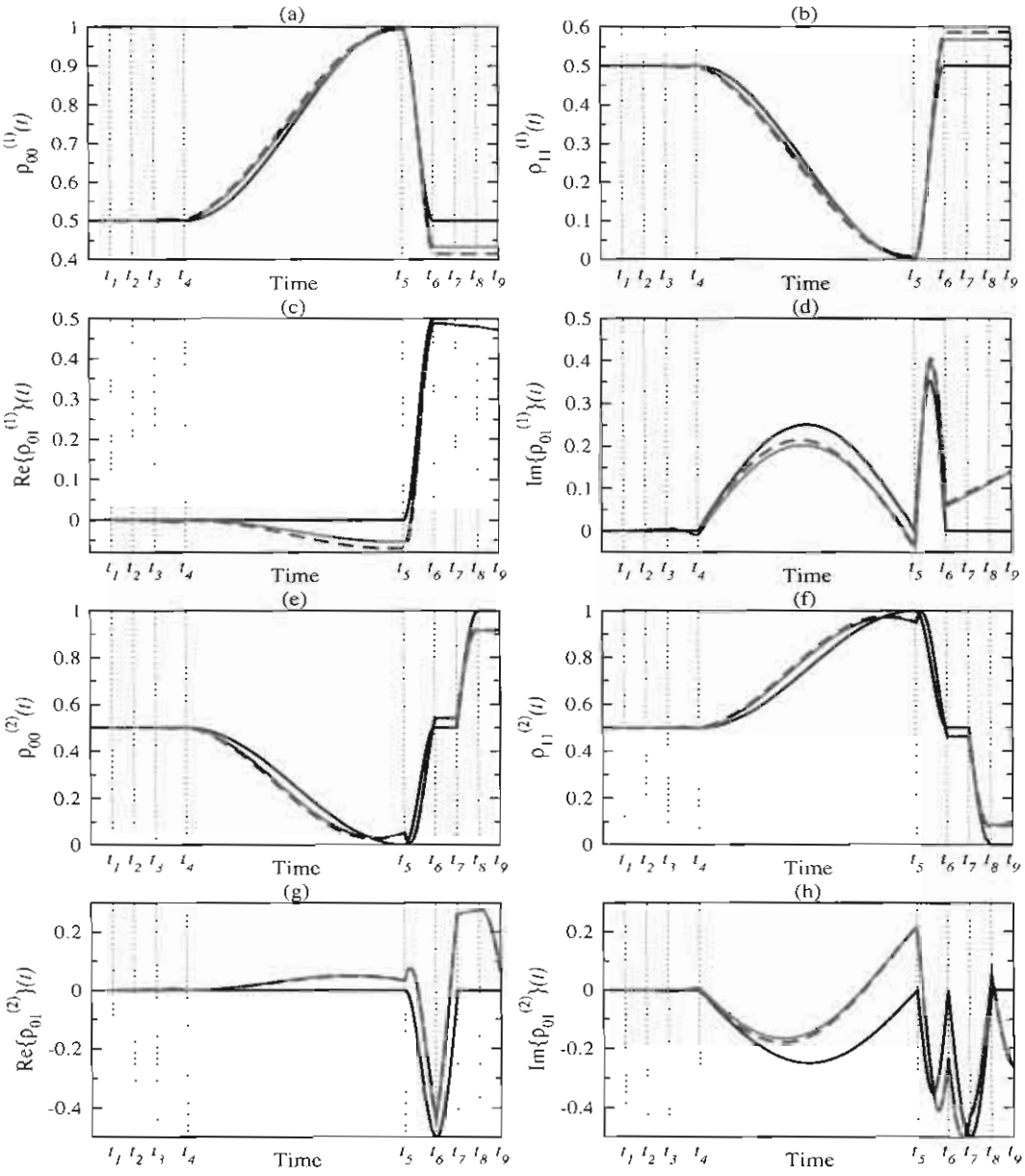

Figure 6.14: Exact numerical (solid green lines) and CKD (dashed red lines) results for matrix elements of reduced density of first and second qubits in the case of zz-type coupling. Coherent time evolution is given by a solid black line. The initial state of the system is a Bell state of the form $(|00\rangle + |11\rangle)/\sqrt{2}$ and the intra-bath coupling $J_x = 1.00\ \epsilon$. $\rho_{00}^{(1)}(t)$ plotted in subfigure (a), $\rho_{11}^{(1)}(t)$ in (b), $\mathrm{Re}\{\rho_{01}^{(1)}(t)\}$ in (c), and $\mathrm{Im}\{\rho_{01}^{(1)}(t)\}$ in (d), $\rho_{00}^{(2)}(t)$ in (e), $\rho_{11}^{(2)}(t)$ in (f), $\mathrm{Re}\{\rho_{01}^{(2)}(t)\}$ in (g), and $\mathrm{Im}\{\rho_{01}^{(2)}(t)\}$ in (h).

Chapter 7

Discussions

This chapter[§] is reserved for discussions and explanations of a number of effects observed in the studies reported in this thesis. In previous chapters the effects of static internal imperfections on QC operations have been investigated. The primary objective has been to determine the effect of internal errors on QC operations, and also secondarily to determine the effects of attendant chaos on these errors. In doing so, a variety of two-qubit intra-bath interaction strengths have been considered for which one can expect that increasing two-qubit intra-bath interactions would induce chaos in the bath degree of freedom. In section 7.1, by using two independent methods, it has been confirmed that the bath Hamiltonians are chaotic. It was observed that increasing two-qubit intra-bath interactions results in reduced decoherence and dissipation. In section 7.2 this effect is explained based on three different arguments. In section 7.3 a detailed discussion of the coherent shift process is given and the consequent large unitary errors are explained. In particular, by a comparison between the time scales of fidelity decays for the CNOT and Rabi studies it is argued that the errors arising from coherent shifting can be a serious obstacle for QC operations.

[§]This chapter is partly based on a study [17] reported by Çetinbaş and Wilkie.

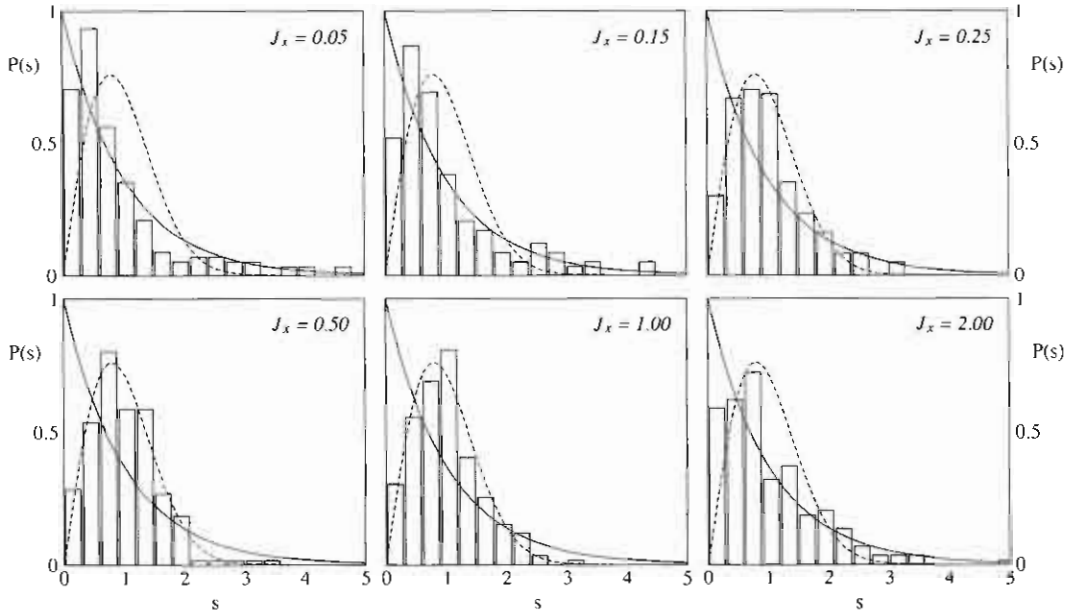

Figure 7.1: Level spacing distribution $P(s)$ versus s. The Poisson distribution $P(s) = \exp(-s)$ is plotted by a solid red line and the Wigner–Dyson distribution $P(s) = (\pi/2)s\exp(-\pi s^2/4)$ is plotted by a dashed blue line.

7.1 Identification of chaos: level statistics and Loschmidt echo

A convenient way to verify the crossover from the regular (i.e. non-chaotic) to chaotic regimes is to observe the nearest–neighbor level–spacing distribution $P(s)$. As chaos emerges, the functional form $P(s)$ changes from the Poisson distribution $P(s) = \exp(-s)$, characteristic of regular systems, to the Wigner–Dyson distribution $P(s) = (\pi/2)s\exp(-\pi s^2/4)$, appropriate for chaotic systems [23, 24].

To verify that this transition does indeed occur in the bath Hamiltonian of the QC core, a level statistics analysis was performed on the unfolded spectrum of 200 lowest eigenenergies of $\hat{H}_B$. The unfolded energies, $\bar{E}_i$, were generated from the actual energies, E_i, using the smoothed staircase functions, i.e. $\bar{N}(E)$ via $\bar{E}_i = \bar{N}(E_i)$. Here $\bar{N}(E)$ was obtained as a polyuomial least squares fit to the actual staircase function, $N(E) = \sum_{i=1}^{200}\Theta(E - E_i)$ where

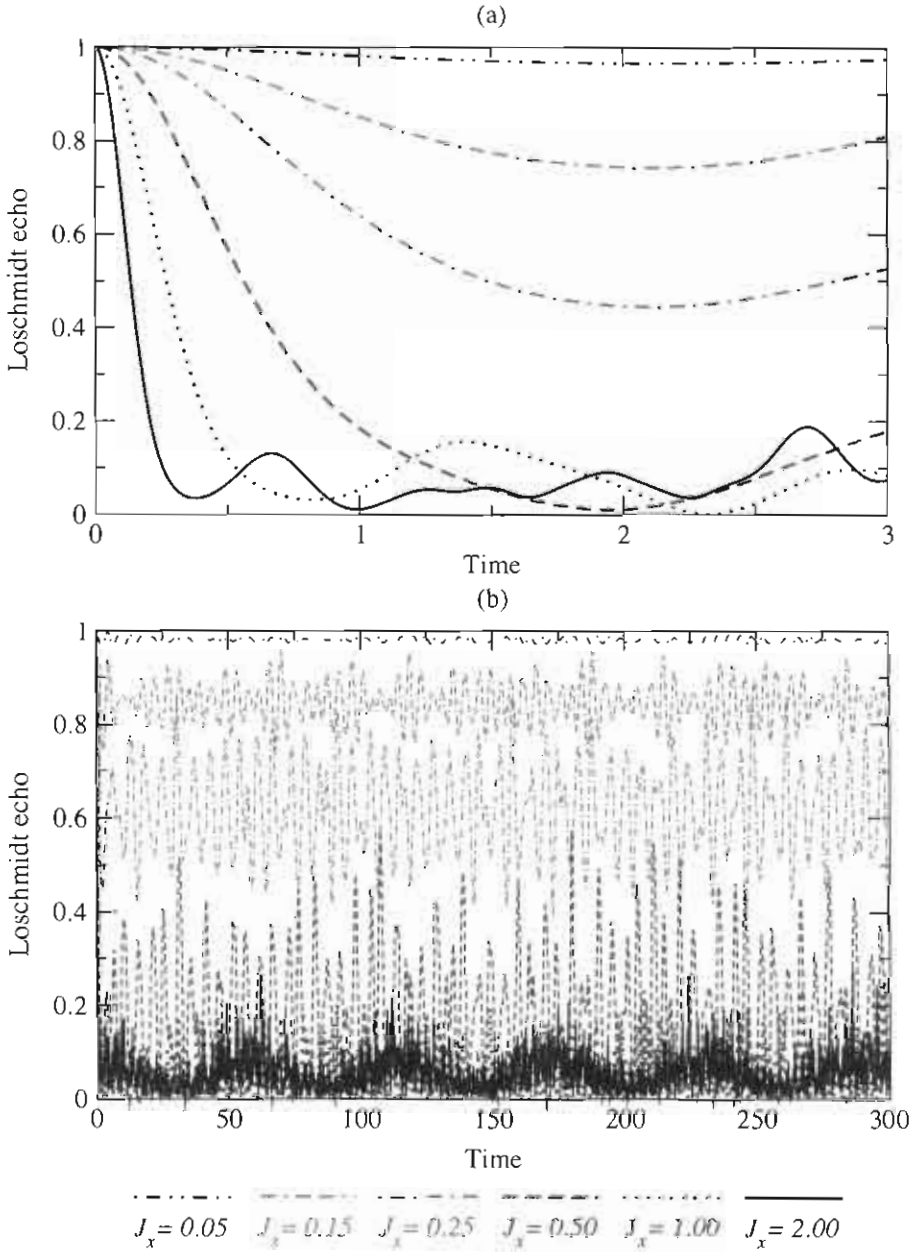

Figure 7.2: (a) Short and (b) long time Loschmidt echo dynamics of the bath Hamiltonian for $J_x = 0.05, 0.15, 0.25, 0.50, 1.00, 2.00$.

$\Theta(x)$ is the Heaviside step function.

A summary of the results of the nearest neighbor spacing analysis are given in figure 7.1. The onset of chaos can be seen for a relatively weak inter-qubit coupling strength of $J_x = 0.15$ where the functional form is close to the Wigner–Dyson distribution. Above this value chaos sets in, and the eigenstatistics are basically consistent with the characteristics of the Wigner–Dyson distribution.

While level–spacing statistics are considered to be a universal indicator of quantum chaos, they do not provide information on the degree of chaos. Therefore, the Loschmidt echo, $M(t)$ [89] was also examined, which is widely believed to be an efficient indicator of quantum chaos [90], and which also gives a quantitative indication of the strength of the chaos.

The Loschmidt echo is calculated for the bath Hamiltonian with the following formula,

$$M(t) = |\langle\psi_0| \exp\{i\hat{H}_0 t/\hbar\} \exp\{-i(\hat{H}_0 + \hat{V})t/\hbar\}|\psi_0\rangle|^2, \tag{7.1}$$

where $|\psi_0\rangle$ is the ground eigenstate of $\hat{H}_0$, $\hat{H}_0$ is the regular bath Hamiltonian (i.e. $\hat{H}_B$ for $J_x = 0.00$) and $\hat{V}$ is the chaos generating perturbation Hamiltonian (i.e., the xx coupling terms) for $J_x = 0.05, 0.15, 0.50, 1.00, 2.00$. A summary of the $M(t)$ calculations is presented in figure 7.2.

It is clear from figure 7.2 that an increasing magnitude of intra-bath coupling J_x results in faster exponential decay of $M(t)$, and this may be interpreted as an increasing degree of chaos. Note that for smaller J_x (i.e $J_x < 0.50$) the echo $M(t)$ does not reach zero.

7.2 Non-unitary effects

In this section, the reduction of decoherence due to the chaos generating two-body intra-bath interactions is discussed. This effect was the subject of a number of studies and can be explained by three different but related arguments. The first argument is based on

the chaotic Kraus decomposition, the second argument is based on an approximate mean-field master equation and finally, the third argument is based on intra-bath entanglement generation due to two-body intra-bath interactions.

First argument

The performance of the CKD was tested in the chaotic regime for a large number of QC configurations and surpassingly accurate results were obtained despite the small bath size used in the simulations. It was observed that the accuracy of the CKD dramatically increased with increasing degree of bath chaos. The most accurate results were obtained for the strongly chaotic regime, i.e. $J_x = 2.00\ \epsilon$. In the case of xx-type system-bath interactions, the predictions of the CKD were in an excellent agreement with exact results. However, in the case of zz-type system-bath interactions, while the qualitative performance of the CKD was still good, the quantitative agreements between the CKD and exact results were relatively poor as compared to xx-type coupling cases.

The derivation of the CKD is based on the assumption that off-diagonal matrix elements of a bath coupling operator become vanishingly small for large chaotic baths, which implies that the CKD becomes exact in the semi-classical limit for large chaotic baths or when the number of bath modes approaches the thermodynamics limit. In what follows, it is expected that the performance of the CKD in predicting exact results should be proportional to the dimension of the bath degree of freedom. Hence, the larger the number of bath modes, the more accurate the CKD predictions should be. However, the exact benchmark results used to test the CKD were limited to quite small baths, i.e. 10-qubit baths. Nevertheless, surprisingly good results are obtained especially for xx-type coupling cases. For baths of such small size, the off-diagonals can be quite small, but should not be totally vanishing.

Figure 7.3 shows the absolute values of off-diagonal matrix elements of bath coupling operators, $|\langle\phi_n^B|\hat{\Sigma}_x|\phi_1^B\rangle|$ and $|\langle\phi_n^B|\hat{\Sigma}_z|\phi_1^B\rangle|$ versus eigenvector index n for increasing values

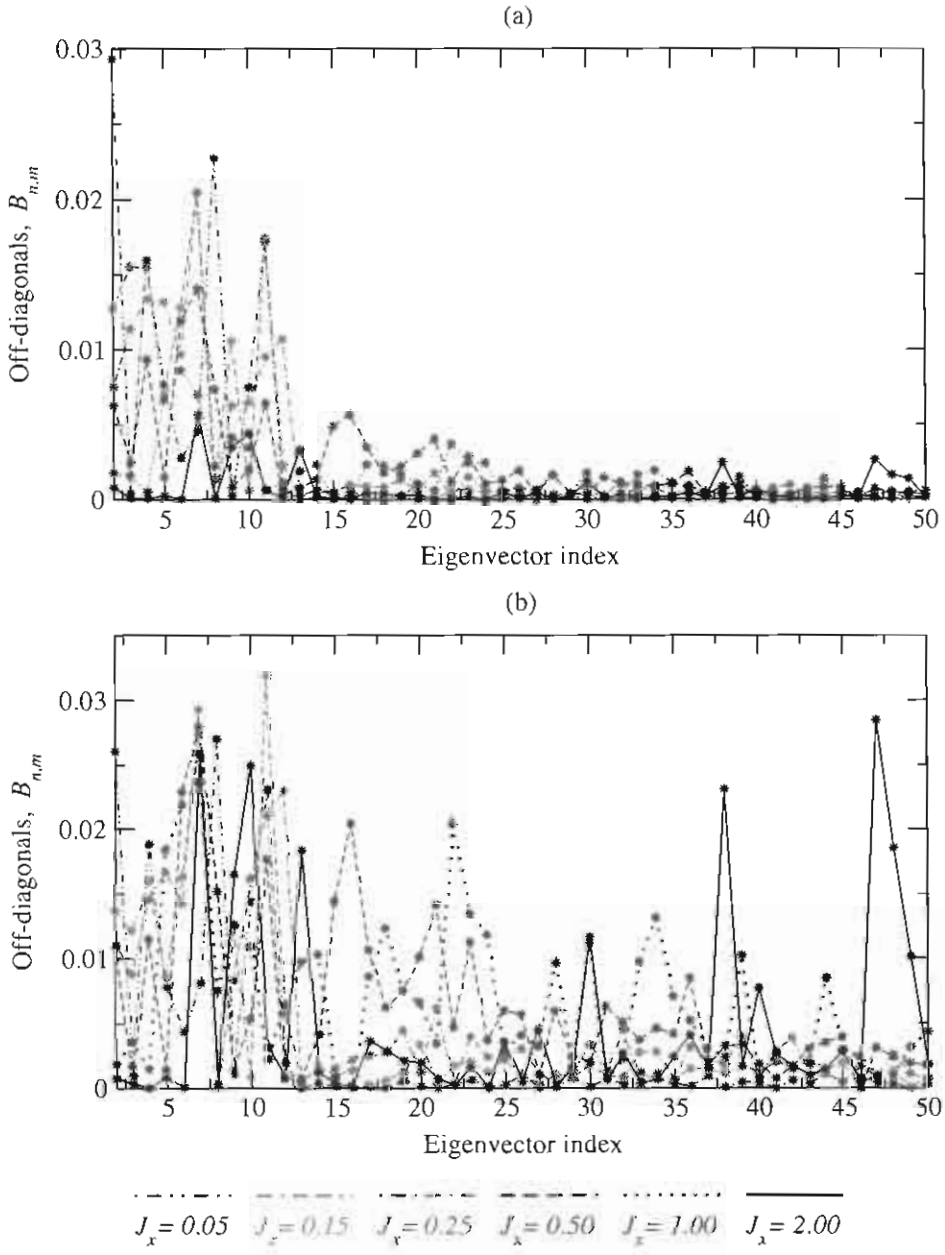

Figure 7.3: In (a) for xx-type coupling and in (b) for zz-type coupling, the absolute values of off-diagonal matrix elements of bath coupling operators, $|\langle\phi_n^B|\hat{\Sigma}_x|\phi_1^B\rangle|$ and $|\langle\phi_n^B|\hat{\Sigma}_z|\phi_1^B\rangle|$ versus eigenvector index are plotted for increasing values of intra-bath coupling J_x. Here the state $|\phi_1^B\rangle$ refers to the ground state of $\hat{H}_B$ and the index n labeling the eigenstates $|\phi_n^B\rangle$ of $\hat{H}_B$ runs from $n = 2$ to $n = 50$. Data points are connected by lines to guide to the eye.

of intra-bath coupling J_x. In figure 7.3(a) the off-diagonals are plotted for xx-type coupling and in figure 7.3(b), the off-diagonals are plotted for zz-type coupling. $n = 199$ matrix elements are calculated but only $n = 50$ of those are plotted for the clarity of the figures. The magnitude of the remaining matrix elements are very close the magnitude of matrix elements for $n = 50$. In the case of xx-type coupling, it is clear that increasing the magnitude of chaos generating intra-bath interactions, parameterized by J_x, results in a systematic reduction in the magnitudes of the off-diagonal matrix elements. However, in the case of zz-type coupling, it is not clear that the magnitude of the off-diagonal actually decreases. These observations are consistent with the accuracy of the CKD for differeut types of system-environment couplings. The test results showed very good agreement between exact and CKD results for xx-type coupling for which the off-diagonal matrix elements become small as intra-bath coupling increases. In the case of zz-type coupling, the performance of the CKD was poor as compared to the xx-type coupling cases for which the off-diagonal matrix elements did not show a systematic decrease as intra-bath coupling increases.

The good performance of the CKD in predicting exact results, especially for xx-type coupling cases, suggests that the suppression of decoherence effect should be related to the arguments used in derivation of the CKD. Nevertheless, since the arguments can only be justifiable for very large environments, the tendency of decreasing off-diagonals with increasing J_x as well as the observed accuracy of the CKD should be related to a special effect (which is justifiable for small baths) rather than the dimension of the bath degree of freedom.

The chaos generating two-body iuteractions, parameterized by J_x, in the bath Hamiltonians $\hat{H}_B$ are of xx-type. In the strongly chaotic regime the bath Hamiltonians are dominated by xx-type intra-bath interactions. Hence, in the case of xx-type sytem-bath interactions, and for strong J_x, the eigenstates of $\hat{H}_B$ are then also the eigenstates of xx-type interaction operators, which implies that the off-diagonals becomes very small due to the orthogonality

of these eigenstates rather than the large bath dimension. This special effect explains the surprisingly good accuracy of the CKD in the case of xx-type system-bath interactions. Since there is no such a special effect for zz-type system-bath interactions, the accuracy of the CKD for zz-type system-bath interactions was relatively poor. While this special effect explains the accuracy of the CKD for different types system-bath interactions it does not provide a complete explanation for the observed systematic suppression of decoherence effect in the case of zz-type system-bath interactions. Before giving the other arguments in this regard, it is noteworthy that there may also be a dynamical contribution to these off-diagonal matrix elements, i.e. rapid phase fluctuations originating from the fast chaotic bath dynamics so that their net contributions to open system dynamics average out to zero. Yet, this situation does not require vanishing of the off-diagonals. This subtlety remains to be confirmed.

Second argument

The second argument with which an attempt is made to explain the suppression of decoherence effect and chaos favored Markovian dynamics is based on a mean field master equation [47-51]. For a total Hamiltonian, $\hat{H} = \hat{H}_S + \hat{S}\hat{B} + \hat{H}_B$, this approximate master equation takes the following form,

$$\frac{d}{dt}\hat{\rho}_S(t) = -(i/\hbar)[\hat{H}_{\text{eff}}, \hat{\rho}_S(t)] - \int_0^t dt' W(t-t')\hat{\mathcal{L}}_D\hat{\rho}_S(t'), \tag{7.2}$$

where $\hat{H}_{\text{eff}}$ is an effective subsystem Hamiltonian including coherent shift terms, the form of which will be discussed in section 7.3, $\hat{\mathcal{L}}_D = (C/\hbar^2)\{[\cdot\hat{S}, \hat{S}] + [\hat{S}, \hat{S}\cdot]\}$ is a dissipative Lindblad-Kossakowski operator [9], $\hat{S}$ is the system coupling operator, and C is the canonical variance of the bath coupling operator, $\hat{B}$. The memory function of this master equation, $W(t)$, is given by

$$W(t) = [1 - \frac{4}{3\pi}(pt)^1 + \frac{1}{8}(pt)^2 - \frac{4}{45\pi}(pt)^3 + \frac{1}{48}(pt)^4]e^{-(qt)^2/8}, \tag{7.3}$$

where

$$p = [\langle \mathcal{A}\mathcal{A}^\dagger \rangle - \langle \mathcal{A}\mathcal{A} \rangle]/\sqrt{\langle \mathcal{A}\mathcal{A}^\dagger \rangle}, \tag{7.4}$$

$$q = [\langle \mathcal{A}\mathcal{A}^\dagger \rangle + \langle \mathcal{A}\mathcal{A} \rangle]/\sqrt{\langle \mathcal{A}\mathcal{A}^\dagger \rangle}, \tag{7.5}$$

and

$$\begin{aligned} \langle \mathcal{A}\mathcal{A} \rangle &= \frac{1}{m_S^2 m_B^2}[2m_S m_B \mathrm{Tr}\{\hat{H}^2\} - 2\mathrm{Tr}\{\hat{H}\}^2 + 4\mathrm{Tr}_B\{\mathrm{Tr}_S\{\hat{H}\}^2\hat{\rho}_B\} \\ &+ 2m_S \mathrm{Tr}_S\{\mathrm{Tr}_B\{\hat{H}\hat{\rho}_B\}^2\} - 4m_S \mathrm{Tr}\{\hat{H}^2\hat{\rho}_B\} - 2\mathrm{Tr}\{\hat{H}\hat{\rho}_B\}^2]. \end{aligned} \tag{7.6}$$

$$\begin{aligned} \langle \mathcal{A}\mathcal{A}^\dagger \rangle &= \frac{1}{m_S^2 m_B^2}[2m_S m_B \mathrm{Tr}\{\hat{H}^2\} - 2\mathrm{Tr}\{\hat{H}\}^2 - 8m_S \mathrm{Tr}\{\hat{H}^2\hat{\rho}_B\} - 4\mathrm{Tr}\{\hat{H}\hat{\rho}_B\}^2 \\ &+ 2m_S m_B \mathrm{Tr}\{\hat{H}^2\hat{\rho}_B^2\} + 2m_S \mathrm{Tr}\{\hat{H}^2\}\mathrm{Tr}_B\{\hat{\rho}_B^2\} + 4m_B \mathrm{Tr}\{\hat{H}\hat{\rho}_B\}\mathrm{Tr}\{\hat{H}\hat{\rho}_B^2\} \\ &+ 8\mathrm{Tr}_B\{\mathrm{Tr}_S\{\hat{H}\}^2\hat{\rho}_B\} + 4m_S \mathrm{Tr}_S\{\mathrm{Tr}_B\{\hat{H}\hat{\rho}_B\}^2\} + 4m_S \mathrm{Tr}_S\{\mathrm{Tr}_B\{\hat{H}\hat{\rho}_B^2\}\mathrm{Tr}_B\{\hat{H}\}\} \\ &- 4\mathrm{Tr}\{\hat{H}\}\mathrm{Tr}\{\hat{H}\hat{\rho}_B^2\} - 2m_B \mathrm{Tr}_B\{\mathrm{Tr}_S\{\hat{H}\hat{\rho}_B\}^2\} - 2\mathrm{Tr}_B\{\mathrm{Tr}_S\{\hat{H}\}^2\}\mathrm{Tr}_B\{\hat{\rho}_B^2\} \\ &- 4m_S m_B \mathrm{Tr}_S\{\mathrm{Tr}_B\{\hat{H}\hat{\rho}_B\}\mathrm{Tr}_B\{\hat{H}\hat{\rho}_B^2\}\} - 4m_S \mathrm{Tr}_S\{\mathrm{Tr}_B\{\hat{H}\}\mathrm{Tr}_B\{\hat{H}\hat{\rho}_B\}\}\mathrm{Tr}_B\{\hat{\rho}_B^2\} \\ &+ 2m_S m_B \mathrm{Tr}_S\{\mathrm{Tr}_B\{\hat{H}\hat{\rho}_B\}^2\}\mathrm{Tr}_B\{\hat{\rho}_B^2\} - 2m_B \mathrm{Tr}\{\hat{H}\hat{\rho}_B\}^2\mathrm{Tr}_B\{\hat{\rho}_B^2\} \\ &+ 4\mathrm{Tr}\{\hat{H}\}\mathrm{Tr}\{\hat{H}\hat{\rho}_B\}\mathrm{Tr}_B\{\hat{\rho}_B^2\}] \end{aligned} \tag{7.7}$$

Master equations which include a memory function like $W(t)$ are called non-Markovian master equations. Master equations which do not take into account the memory effects are called Markovian master equations.

The parameters, p and q, given by equations (7.4) and (7.5) are taken from the appendix of report [50]. These parameters are defined over a finite basis and thus it is necessary that all the operators appearing in equations (7.6) and (7.7) be represented by using a finite basis before calculations are done. The parameters of the master equation involve two types of averages: canonical and ordinary averages. According to the prescription given in [50], the canonical averages including C, $\bar{B}$, and also the terms involving the canonical bath density, $\hat{\rho}_B(0)$, are defined for a fixed bath temperature and should be calculated by choosing a cut-off, i.e. n_{eig} such that the states with $n_{eig}+1$ and higher are not populated for a given bath

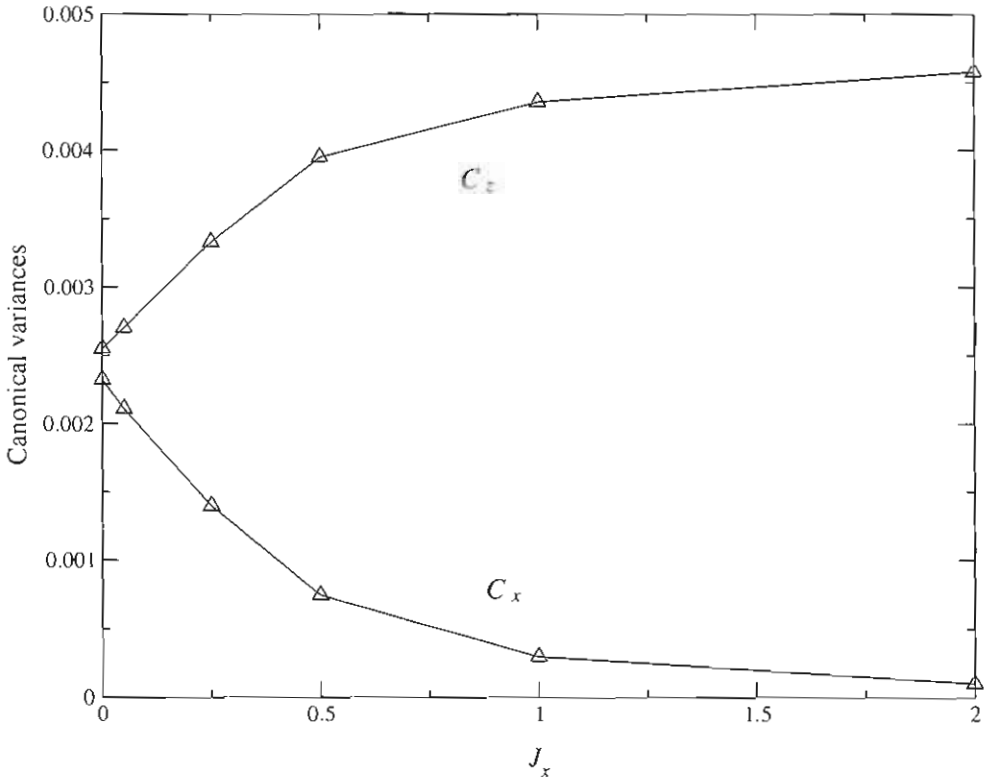

Figure 7.4: Canonical variances, C_x and C_z, in the bath coupling operators for xx- and zz-type couplings are plotted for increasing valnes of J_x. Data points are connected by lines to guide to the eye.

temperature. Note that this is the approximation used in the exact dynamical calculations of the CNOT and Rabi studies. However, the calculation of the ordinary averages such as $\mathrm{Tr}\{\hat{H}\}$ appearing in equations (7.6) and (7.7) requires a full Hamiltonian spectrum. Here, only the low energy spectrum of the bath Hamitonian (not the full spectrum) will be taken into account, and $n_{eig} = 20$ eigenvalues and eigenstates will be used in the calculation of C, $\bar{B}$, and all the terms appearing in p and q. This is because of the following reasons. Firstly, the intention here is not to test the performance of this master equation. Based on recent reports [50, 51], it is simply assumed here that the master equation is physical and captures the importaut aspects of open system dynamics induced by chaotic environments. Secoudly, the knowledge of the full bath spectrum may be important when the uumber of dynamically

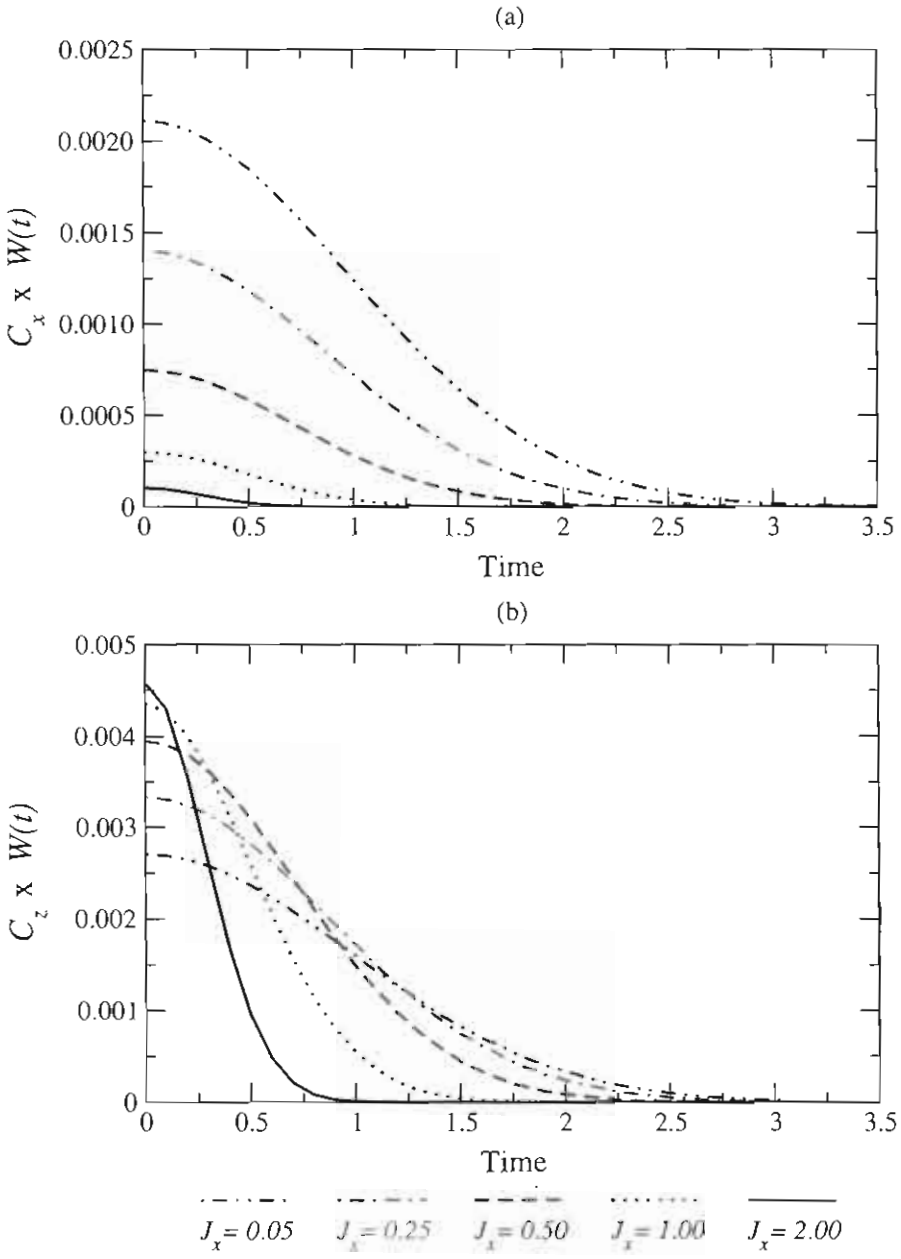

Figure 7.5: The products of the canonical variances, C_x and C_z, and the memory function, $W(t)$, versus time: (a) xx-type coupling and (b) zz-type coupling.

populated bath states is greater than the number of thermally populated bath states. If this were the case, $n_{eig} = 20$ might be a poor approximation. However, the very good agreement between the CKD and exact results indicates that the number of dynamically populated bath states should not be an issue of concern here, since the CKD does not take into account the dynamically populated bath states. Hence, $n_{eig} = 20$ should suffice to show that the chaotic baths favor Markovian dynamics and suppress decoherence.

The exact numerical calculations for the CNOT and the Rabi studies showed partial recurrences in the purity plots in the regular bath regime. The recurrences are signatures of quantum memory that stems from non-local correlations (between the states of the system and the environment) established by system-environment interactions. For both the CNOT and the Rabi studies, the quantum dynamics is initiated from a state of a product form, i.e. $\hat{\rho}(0) = \hat{\rho}_S(0) \otimes \hat{\rho}_B(0)$. In the course of dynamics, the system and environment states are correlated, which means that the time-evolved state $\hat{\rho}(t)$ cannot be written as a product state, i.e. $\hat{\rho}(t) \neq \hat{\rho}_S(t) \otimes \hat{\rho}_B(t)$. Hence, the effect of system-environment interactions is to generate a correlated state $\hat{\rho}(t)$ representing the state of both system and environment degrees of freedom. Since the correlated state $\hat{\rho}(t)$ represents both system and environment degrees of freedom, the state of the system $\hat{\rho}_S(t) = \mathrm{Tr}_B[\hat{\rho}(t)]$ has a certain memory of the bath degrees of freedom. The CNOT and the Rabi studies showed that the memory effects, i.e. the recurrences in the purity plots lessened with increasing magnitude of intra-bath coupling, i.e. with the emergence of chaos. This effect is attributed to the favored Markovian dynamics due to chaos. Markovian dyuamics (i.e. memoryless dynamics) require a separation of relaxation times for the system and bath degrees of freedom [91]. A chaotic bath can relax internally and quickly. However, the only available relaxation mechanism for a regular bath is through interaction with the subsystem. Therefore, chaotic baths should be more Markovian, which results in reduced memory effects and vanishing recurrences.

The master equation (7.2) predicts that decoherence and dissipation in the chaotic regime

are governed by two factors; the variance, C, of the bath coupling operator, and the positive Gaussian shaped memory function, $W(t)$ (unity at $t = 0$). Thus, based on this master equation, the suppression of decoherence must either be governed by a decreased variance or by an increased Markovian behavior.

To favor Markovian behavior the memory function is expected to shift its weight to shorter times as J_x increases. As a consequence, the bath will tend to cause less decoherence. One would also expect the variance in the xx-type system-bath coupling to decrease with increasing J_x due to the vanishingly small off-diagonal matrix elements. As explained above, the off-diagonals are vanishing because of the orthogonality of eigenstates. However, this need not be the case with zz-type system-bath coupling, because the zz-type coupling operator does not commute with the xx-type coupling operator. Hence, both factors should favor the reduction of decoherence in the xx-type coupling case, but the reduction of decoherence in the zz-type coupling case, according to this master equation, should originate from the increasing Markovian nature of the dynamics. To verify these conclusions, firstly, the variances of the bath coupling operators will be examined, and secondly, the product of the variances and memory functions associated with xx and zz-type couplings will be studied.

Defining the system-bath interactions as $\hat{\Sigma}_x = \sum_{i=3}^{N+2} \lambda_i \hat{\sigma}_x^{(i)}$ for xx-type coupling, and $\hat{\Sigma}_z = \sum_{i=3}^{N+2} \lambda_i \hat{\sigma}_z^{(i)}$ for zz-type coupling, the variances of these interactions operators can now be given via $C_x = \mathrm{Tr}_B[(\hat{\Sigma}_x - \bar{\Sigma}_x)^2 \hat{\rho}_B(0)]$ for the xx case, and $C_z = \mathrm{Tr}_B[(\hat{\Sigma}_z - \bar{\Sigma}_z)^2 \hat{\rho}_B(0)]$ for the zz case. Here $\bar{\Sigma}_x = \mathrm{Tr}_B[\hat{\Sigma}_x \hat{\rho}_B(0)]$ and $\bar{\Sigma}_z = \mathrm{Tr}_B[\hat{\Sigma}_z \hat{\rho}_B(0)]$ denote the canonical averages. The definition of $\hat{\rho}_B(0)$ is given in equation (3.37).

In figure 7.4, the canonical variances of bath coupling operators are plotted as a function of J_x. Figure 7.4 shows a decline of the variance for $\hat{\Sigma}_x$ with increasing J_x. Note, however, that there is a growth of variance for $\hat{\Sigma}_z$ with increasing J_x, as expected. C_x declines with increasing J_x because the chaos generating interactions, parameterized by J_x, and the bath

coupling operator, $\hat{\Sigma}_x$, are of the same kind. For strong J_x, the eigenstates of $\hat{H}_B$ are also eigenstates of $\hat{\Sigma}_x$. Hence, the off-diagonals of $\hat{\Sigma}_x$ in the basis of $\hat{H}_B$ are vanishing. Note that this situation does not require a large thermodynamic bath dimension because of the orthogonality of eigenstates. In parallel to the $\hat{\Sigma}_x$ case, a growth of C_z with J_x can also be understood because the variances are calculated over the same bath states and $\hat{\Sigma}_x$ and $\hat{\Sigma}_z$ operators are related by canonical commutation rules.

In figure 7.5(a), the product of the variance and the memory function for xx-type coupling is plotted for different values of J_x. The dominant effect here is the decrease in the magnitude caused by the reduction of variance. However, the function is also becoming more Markovian, since it is weighted over a smaller time interval. In figure 7.5(b), the the product of the variance and the memory function for zz-type coupling is plotted for different values of J_x. Figure 7.5(b) shows a growth in the initial magnitude which corresponds to an increase in the variance. But there is also a marked shift toward shorter times. Again, the dynamics are becoming more Markovian with strong J_x, and it is this which should cause the reduction of decoherence. Thus, both types of coupling show a reduction of decoherence in the chaotic regime, but the manifestation of this effect is a bit different.

Third argument

The suppression of decoherence in the presence of two-body intra-bath interactions can also be explained by an argument developed by Dawson *et al* [34]. The authors argued that this effect originates from the monogamous nature of quantum entanglement [92]. Examining the details of this argument requires basic information on entangled states and quantum entanglement which is provided below.

Entangled states can simply be considered as non-local superpositions of states between two quantum subsystems. Note however that multipartite entanglement among many quantum subsystems is also possible. Here, for the sake of argument, the discussions are limited

to two quantum subsystems. In the course of open system dynamics, for example, an initial state of product form, $\hat{\rho}(0) = \hat{\rho}_S(0) \otimes \hat{\rho}_B(0)$, for the subsystem, S, and the bath, B, becomes an entangled state due to the system-environment interactions, which means that the time evolved state for the bipartite system represented by $\hat{\rho}(t)$ cannot be written as a product form of its components anymore, i.e. $\hat{\rho}(t) \neq \hat{\rho}_S(t) \otimes \hat{\rho}_B(t)$. Hence, decoherence emerges in the subsystem state, $\hat{\rho}_S(t) = \mathrm{Tr}_B[\hat{\rho}(t)]$, for which $\mathcal{P}(t) = \mathrm{Tr}_S[\hat{\rho}_S^2] < 1$, since the bipartite state, $\hat{\rho}(t)$, is an entangled state.

The typical examples of entangled states are the Bell states (see equation (3.31), for example), which are also called maximally entangled states. Here, the maximality of entanglement has an important implication for decoherence. That is, the maximum entanglement between two subsystem states implies a complete decoherence on the state of each subsystem. Consider two qubits A and B in the possession of Alice and Bob. Assume that Alice and Bob's two qubit state is a Bell state of the form, $|AB\rangle = (|00\rangle + |11\rangle)/\sqrt{2}$, which represents a state of two qubits for the bipartite system, $A + B$. A probe on either Alice's qubit $\hat{\rho}_A = \mathrm{Tr}_B\{|AB\rangle\langle AB|\}$ or Bob's qubit $\hat{\rho}_B = \mathrm{Tr}_A\{|AB\rangle\langle AB|\}$ shows that

$$\hat{\rho}_A = \begin{pmatrix} \frac{1}{2} & 0 \\ 0 & \frac{1}{2} \end{pmatrix} \quad \text{and} \quad \hat{\rho}_B = \begin{pmatrix} \frac{1}{2} & 0 \\ 0 & \frac{1}{2} \end{pmatrix}.$$

Hence, while the two-qubit Bell state $|AB\rangle$ is a pure state, the single qubit states, $\hat{\rho}_A$ and $\hat{\rho}_B$, are non-pure and show a complete decoherence for which the purity takes its minimum value, $\mathcal{P}_A = \mathcal{P}_B = 1/2$.

To gain an insight into the monogamy of entanglement, consider now three qubits A, B, and C in the possession of Alice, Bob, and Charlie. Assume that Alice and Bob's qubits, i.e. $A + B$ are in a maximally entangled Bell state and Charlie's qubit is in an arbitrary one-qubit state. In order for this Bell state to correlate with the state of Charlie's qubit, the maximality condition on the Bell state must be given up. Otherwise, there would be no three-partite correlations. This is the simple picture of monogamy of entanglement which

suggests that quantum correlation cannot be freely shared.

Now, the supression of decoherence argument by Dawson *et al* [34] can be stated. The authors show in [34] that the entanglement shared by a bipartite quantum system, i.e. a subsystem and bath, is limited by the amount of entanglement each system (i.e. subsystem and bath) possesses separately. Hence, by maximizing the intra-bath entanglement [34], provided that the maximality of intra-bath entanglement is preserved under the action of local bath Hamiltonian, one can in principle minimize the system-bath entanglement. As a result, decoherence can be suppressed.

It is noteworthy that the entanglement argument does not make a reference to the bath chaos. However, there is a connection between chaos and entanglement, which is discussed below. During a crossover from a regular to chaotic regime, uot only eigenstatistics but also the properties of eigenstates dramatically chauge. To see this, consider a chaotic bath Hamitonian written in a two compouent form, $\hat{H}_B = \hat{H}_0 + \hat{V}$ where $\hat{H}_0$ is the regular Hamitonian component (i.e. non-chaotic), e.g. representing one-body interactions (i.e. $\hat{H}_B$ for $J_x = 0$) and $\hat{V}$ is the chaos generatiug interactions component, e.g. representing two-body interactions (i.e. $\hat{H}_B$ for $J_x \neq 0$). Let $\hat{H}_0|i\rangle = E_i|i\rangle$ be eigenvalues and complete eigenvectors of $\hat{H}_0$. The eigenvectors, $|n\rangle$, of the chaotic bath Hamiltonian, $\hat{H}_B$ (with $J_x \neq 0$) can be written as a linear combination of eigenvectors of the regular Hamiltonian, i.e. $|n\rangle = \sum_i c_i|i\rangle$. Here, the effect of chaos generating interactions, V, is to mix the regular Hamiltoniaus' eigenstates. Hence, the eigenstates of the chaotic bath Hamiltonian show a high degree of quantum correlations in the eigenbasis of the corresponding regular Hamiltonian. Since the quantum entanglement is a special case of general superpositions, the multipartite entanglement in eigenstates of chaotic Hamiltoniaus is then quite natural. Indeed, it has been shown in a number of studies [93] that quantum chaos results in an entanglement generation.

While the chaos and entanglement arguments may seem equivalent this may not be

always the case. There is evidence [94] that chaos reduces entanglement generation in some cases. It has also been shown [35-38] that chaotic baths induce more decoherence than regular baths in some instances. This is an opposite effect to that reported in this thesis. It would be interesting to verify whether only intra-bath entanglement generating chaotic interactions reduces decoherence.

7.3 Unitary effects

All unitary effects observed in the CNOT and Rabi detector studies arise as a consequence of the coherent shift process. According to the CKD, the coherent shift emerges from a Hamiltonian of the form $\hat{H} = \hat{H}_S + \hat{S}\hat{B} + \hat{H}_B$ as

$$\hat{H}_n \rightarrow \hat{H}_S + \hat{S}\langle n|\hat{B}|n\rangle \tag{7.8}$$

where $\langle n|B|n\rangle$ are the diagonal matrix elements of bath coupling operator, $\hat{B}$. The coherent shift enters the approximate master equation (7.2) through the effective system Hamiltonian $\hat{H}_{\text{eff}}$, which is of the form,

$$\hat{H}_{\text{eff}} = \hat{H}_S + \hat{S}\bar{B}, \tag{7.9}$$

where $\bar{B}$ is the canonical average of the bath coupling operator, $\hat{B}$. Note that the shift predicted by the CKD and the approximate master equation is equivalent at absolute zero temperature, provided that the only populated bath state at absolute zero is the ground state of the bath. At very low bath temperatures, where the quantum technologies are expected to operate, the number of populated bath states will be quite low and thus the bath dynamics will be dominated by the ground state of the bath Hamiltonian. As a result, the CKD and the approximate master equation should give equivalent results for the coherent shift process at very low temperatures.

The form of the coherent shift Hamitonian suggests that a non-negligible contribution from the coherent shift should always be expected whenever the canonical average of the

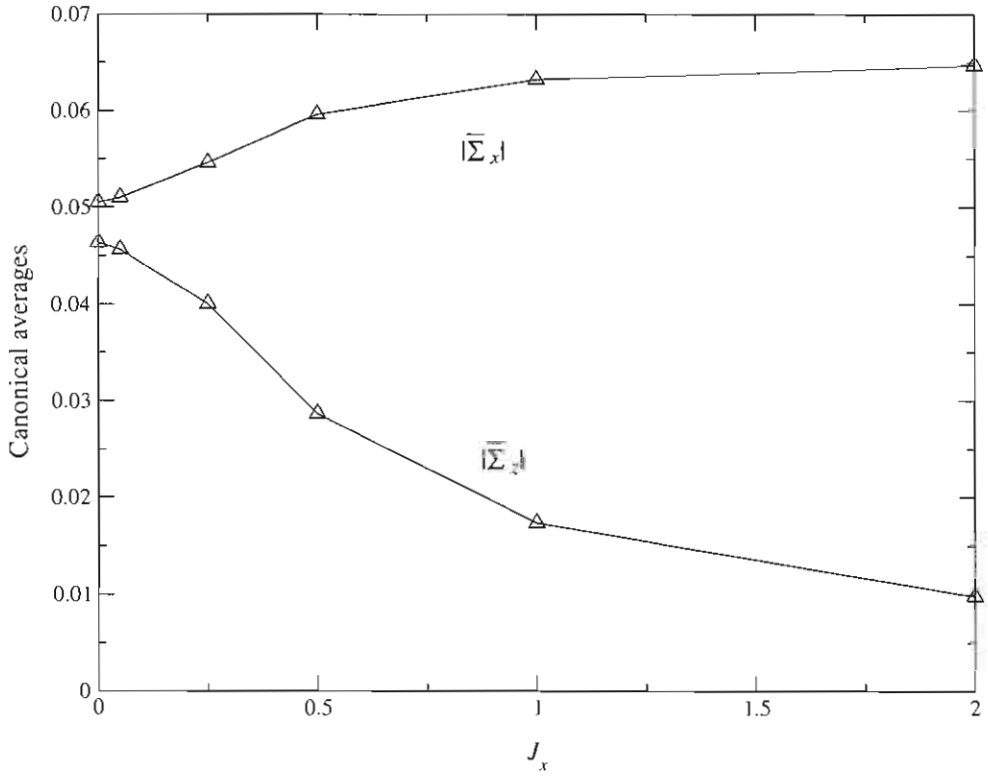

Figure 7.6: Absolute values of canonical averages, $|\bar{\Sigma}_x|$ and $|\bar{\Sigma}_z|$, are plotted for increasing values of J_x. Data points are connected by lines to guide to the eye.

subsystem-bath coupling operator has a non-vanishing value (i.e., $\bar{B} \neq 0$). In some of the older spin-boson and boson-boson studies, the existence of coherent shift was not discussed since the coupling operators are of Jaynes-Cummings or coordinate type for which $\bar{B} = 0$, and the shift therefore vanishes. The coherent shift has important consequences when the native subsystem Hamiltonian does not commute with the shift Hamiltonian, i.e. $[\hat{H}_S, \hat{S}] \neq 0$. In this case, the effect of the shift is a distortion of the subsystem dynamics which can cause large unitary errors. In cases where the subsystem and shift Hamiltonians commute, the coherent shift, more or less, corresponds to an energy shift similar to Lamb shift–like contributions. In this case, generation of unitary errors may be more easily avoided.

Figure 7.6 shows the absolute values of the canonical averages of the bath-coupling operators, i.e. $|\bar{\Sigma}_x| = |\mathrm{Tr}[\hat{\Sigma}_x \hat{\rho}_B(0)]|$ and $|\Sigma_z| = |\mathrm{Tr}[\hat{\Sigma}_z \hat{\rho}_B(0)]|$, versus increasing values of J_x.

In the case of zz-type coupling, an overall decrease in the average is seen with increasing magnitude of J_x. In the case of xx-type coupling, however, the increasing magnitude of J_x results in a small increase in the average. This is clearly consistent with the observed improvement in fidelity with increasing J_x for zz–type coupling (seen in figures 4.11 and 4.12) and the slight decline of fidelity for xx–type coupling (seen in figures 4.9 and 4.10).

The unitary effects observed in the CNOT study are not of Lamb shift type and thus are quite worrying. The magnitude of the fidelity decay for the span of a single CNOT gate is much larger than one would have expected based on the results of the Rabi study. The bath Hamiltonian, and xx-type coupling operator and its strength, employed in the Rabi study, were identical to those used in the CNOT study, so that the magnitude of the shift is not altered, but somehow the shift is dramatically more harmful. Moreover, this has nothing to do with the small subsystem dimension.

To show this, calcnlations were carried out for a two-qubit subsystem (two-qubit Rabi detector) which has the subsystem Hamiltonian,

$$\hat{H}_S = -\frac{1}{2}(B_z\hat{\sigma}_z^{(1)} + B_z\hat{\sigma}_z^{(2)}), \tag{7.10}$$

where $B_z = 1\ \epsilon$ and the dynamics evolve from an initial state of the form, $|\psi_0\rangle = (|0\rangle + |1\rangle) \otimes (|0\rangle + |1\rangle)/\sqrt{2}$. The fidelity for the two-qubit Rabi detector is plotted in figure 7.7, which shows that the two-qubit Rabi detector shows a similar fidelity decay behavior to the single–qubit Rabi detector seen in figure 5.5.

The only remaining possibility for the large fidelity decay observed for the CNOT gate is the state dependency of fidelity. That is, the rapidly changing nature of the state on which the CNOT gate operates should be responsible for the large fidelity decay. In what follows, a direct analogy between the CNOT subsystem and a kicked-top [95] can readily be established by viewing the fidelity (in the absence of thc weak non-nnitary effects) as being similar to the Loschmidt echo of a kicked-top [96]. A kicked-top is a simple system displaying irreversible and chaotic behavior, which can be considered as a single spin (e.g.

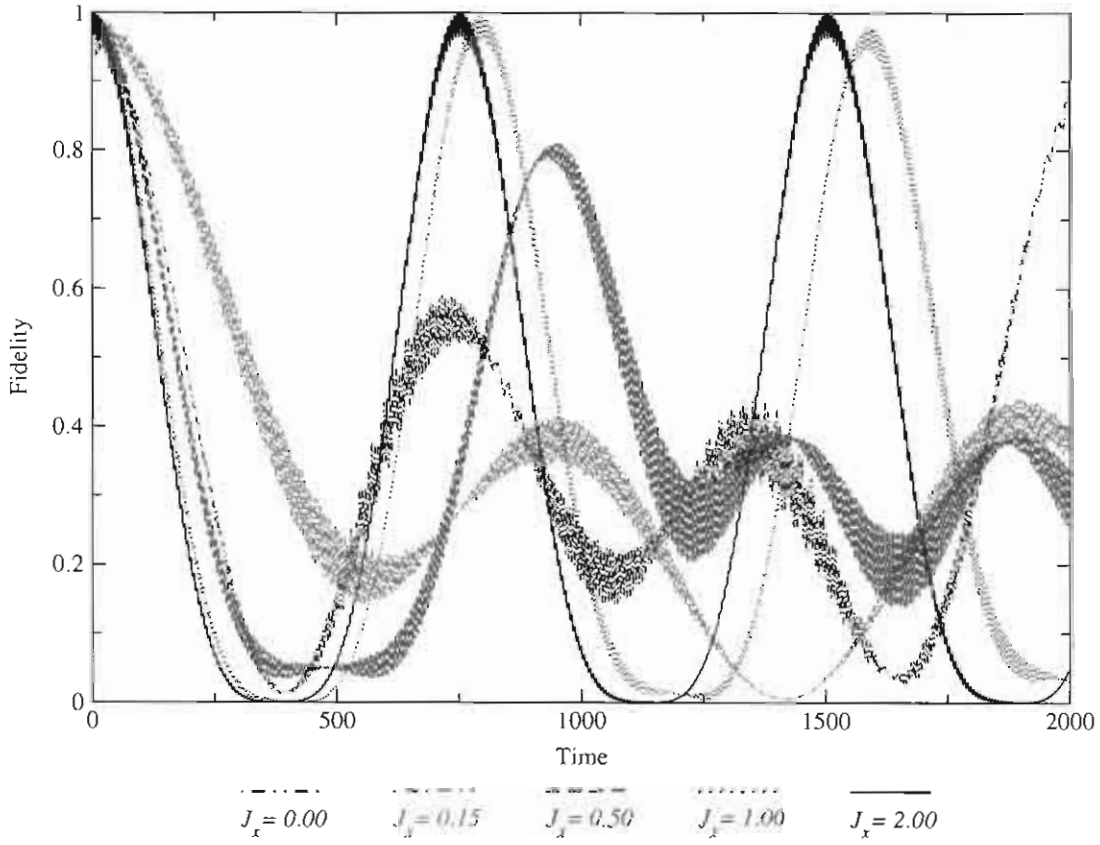

Figure 7.7: Time evolution of fidelity, $\mathcal{F}(t)$, for two-qubit Rabi detector.

a qubit) subject to periodic perturbations. Thc detailed discussion of the kicked-top can be found in [95, 96]. Here, only an analogy between dynamical behaviors of a kicked-top and the CNOT gate is made.

A second unexpected effect is that the fidelity decay seems to be almost independent of $\bar{B}$, which itself changes with J_x as shown in fignre 7.6. In the single qnbit Rabi detector stndy [18], the fidelity decay time was highly sensitive to J_x, and the same is true of the two-qubit Rabi detector (see figure 7.7). Here, the period of the decay increases snbstantially by 10 ns when J_x increases from zero to 0.15 ϵ, then declines from $J_x = 0.15\ \epsilon$ to $J_x = 0.50\ \epsilon$, and finally moves toward some saturated value after $J_x = 1.00\ \epsilon$. Fidelity decay times for the CNOT with xx-type coupling vary by less than 0.1 ns. This is thus a major effect. It

seems quite likely that these two unusual effects are somehow related, and that the CNOT dynamics have a phenomenology similar to that of the Loschmidt echo of a kicked-top [96].

It is well-known that there are two regimes of Loschmidt echo of a kicked-top [96]: the fast exponential decay regime which is insensitive to the pertnrbation strength, and the Golden Rule regime where decays are slower and decay rates depend on the perturbation strength [96]. The results for the CNOT gate and Rabi detectors also fit into this picture, and the origin of the two unexpected unitary effects can be explained as arising from the rapidly changing nature of the CNOT gate.

The two-qubit Rabi detector would correspond to vanishingly weak kicking which would be expected to lie in the Golden Rnle regime, where decays are slower and decay rates depend on the perturbation strength [96]. However, note also that the sensitivity of fidelity to J_x disappears in the strongly chaotic bath regime (i.e. $J_x = 1\ \epsilon$ and $J_x = 2\ \epsilon$) where the period of decay saturates toward a certain value.

On the other hand, it appears that the CNOT gate for the xx-type coupling case lies in the exponential decay regime where the fidelity does not show any sensitivity to perturbation strength. However, the CNOT gate for the zz-type coupling case lies in the Golden Rule regime where the dominant effect is the high sensitivity of fidelity to the perturbation strength. The kicked-top or rapidly changing nature of the CNOT gate suggests that removing the effects of the decay after completion of the gate may not be possible, which means that error correction strategies for the shift must be performed during each snbcomponent of the gate.

Chapter 8

Conclusion

The central theme of this thesis is the open system dynamics of a small quantum system coupled to self-interacting chaotic environments. Many physical and chemical phenomena occur in condensed phase media where dynamics is chaotic. Condensed phase environments also offer a wide range of controllable interactions for new quantum technologies. Hence, the prediction of open system dynamics of quantum systems embedded in chaotic environments can have many important applications. Standard models of decoherence represent an environment degree of freedom as a collection of non-interacting harmonic oscillators or spins. These representations are not valid when environmental dynamics is chaotic.

In the first part of this thesis a Kraus decomposition governing the dynamics of a quantum system interacting with large chaotic environments was derived. The extension of the decomposition to a time-dependent system Hamiltonian was also achieved so that the decomposition has wider applications. In the second part of this thesis two self-interacting – and chaotic – spin bath models were studied by exact numerical calculations. These models represent an isolated QC with static internal imperfections. In the first model, internal decoherence dynamics of a CNOT gate was investigated for a large number of QC configurations: two sets of eight initial subsystem states (i.e. standard basis states and Bell states),

two different types of error generators (i.e. phase and bit-flip errors), and five different values of intra-bath interactions. For these QC configurations, potential sources of errors were identified. The results showed that while internal decoherence can be a matter of concern, the primary source of error is unitary, induced by the coherent shift process. It was shown that chaotic interactions in the environment degree of freedom can suppress the error due to the decoherence. Hence, deliberately induced chaotic bath interactions may prove an efficient error correction strategy when such strong interactions can readily be implemented. The fact that alarming sources of internal errors are unitary, induced by coherent shifting rather than decoherence or dissipation, is not expected from previous studies. Since these errors are unitary and thus deterministic in nature, they may be correctable by existing or specifically tailored new methods. The second model reported in this thesis is a detector set-up configured to probe internal bath dynamics. While coherent shift was identified as a serious source of error, the detector set-up showed that the shift can also be used for a good purpose, and by using the detector valuable information on environmental self-interactions can be obtained. In the third part of this thesis the performance of the Kraus decomposition was tested against exact numerical results of QC models and very good agreements were obtained. The promising results suggest that the Kraus decomposition can be used as a practical computational tool for low temperature applications of open system dynamics induced by chaotic euvironments.

Bibliography

[1] L.E. Ballentine, *Quantum Mechanics: A Modern Development*, (World Scientific, Singapore, 2000).

[2] E. Joos, H.D. Zeh, C. Kiefer, D. Giulini, J. Kupsch, and I.-O. Stamatescu, *Decoherence and the Appearance of a Classical World in Quantum Theory*, (Springer, Berlin, 1996).

[3] H.-P. Breuer and F. Petruccione, *The Theory of Open Quantum Systems*, (Oxford University Press, New York, 2003).

[4] M. Ratner and D. Ratner, *Nanotechnology*, (Prentice Hall, Upper Saddle River, NJ, 2003).

[5] M. Shapiro and P. Brumer, *Principles of the Quantum Control of Molecular Processes*, (Wiley-Interscience, Hoboken, 2003).

[6] G.J. Milburn, *The Feynman Processor: Quantum Entanglement and the Computing Revolution*, (Perseus Books, Reading, Massachusetts, 1998).

[7] M.A. Nielsen and I.L. Chuang, *Quantum Computation and Quantum Information*, (Cambridge University Press, Cambridge, 2000).

[8] H.-K. Lo, S. Popescu and T. Spiller, *Introduction to Quantum Computation and Information*, (World Scientific, Singapore, 1998).

[9] G. Lindblad, Commun. Math. Phys. **48**, 119 (1976); V. Gorini, A. Kossakowski, and E.C.G. Sudarshan, J. Math. Phys. **17**, 821 (1976); R. Alicki and K. Lendi, *Quantum Dynamical Semigroups and Applications*, (Springer, Berlin, 1987).

[10] C.W. Gardiner and P. Zoller, *Quantum Noise, 3rd Ed.*, (Springer, Berlin, 2004).

[11] See for example: C. Anastopoulos and B.L. Hu, Phys. Rev. A **62**, 033821 (2000); A.O. Caldeira and A.J. Leggett, Ann. Phys. **149**, 374 (1983); R.P. Feynman and F.L. Vernon, Jr., Ann. Phys. **24**, 118 (1963); F. Haake and R. Reibold, Phys. Rev. A **32**, 2462 (1985); A.O. Caldeira and A.J. Leggett, Physica A **121**, 587 (1983).

[12] N.V. Prokof'ev and P.C.E. Stamp, Rep. Prog. Phys. **63**, 669 (2000).

[13] V. S. Batista and P. Brumer, Phys. Rev. Lett. **89**, 143201 (2002); J.B. Gong and P. Brumer, Phys. Rev. A **68**, 022101 (2003).

[14] M. Çetinbaş and J. Wilkie, Phys. Lett. A **372**, 990 (2008).

[15] M. Çetinbaş and J. Wilkie, Phys. Lett. A **372**, 1194 (2008).

[16] M. Çetinbaş and J. Wilkie, Phys. Lett. A **370**, 207 (2007).

[17] M. Çetinbaş and J. Wilkie, J. Phys. A **41**, 065302 (2008).

[18] M. Çetinbaş and J. Wilkie, Phys. Lett. A **370**,194 (2007).

[19] M.H. Vos, F. Rappaport, J.-C. Lambry, J. Breton and J.-L. Martin, Nature **363**, 320 (1993).

[20] H.-H. Limbach and J. Manz, Ber. Bunsenges. Phys. Chem. **102**, 3 (1998).

[21] P. Hamm P, M. Lim and R.M. Hochstrasser, Phys. Rev. Lett. **81**, 5326 (1998).

[22] A. Würger, *From Coherent Tunneling to Relaxation*, (Springer-Verlag, Berlin, 1997).

[23] F. Haake, *Quantum Signatures of Chaos*, (Springer, Berlin, 2001).

[24] *Chaos and Quantum Physics*, edited by M.–J. Giannoni, A. Voros, and J. Zinn–Justin, Les Houches Lecture Series Vol. 52, (North–Holland, Amsterdam, 1991).

[25] P. Gaspard, M.E. Briggs, M.K. Francis, J.V. Sengers, R.W. Gammon, J.R. Dorfmann and R.V. Calabrese, Nature **394**, 865 (1998).

[26] T. Miyano, S. Munetoh, K. Moriguchi and A. Shintani, Phys. Rev. E **64**, 016202 (2001).

[27] E. R. Mucciolo, R. B. Capaz, B. L. Altshuler and J. D. Joannopoulos, Phys. Rev. B **50**, 8245 (1994).

[28] J.A. Shields, M.E. Msall, M.S. Carroll and J.P. Wolfe, Phys. Rev. B **47**, 12510 (1993).

[29] L. Tessieri and J. Wilkie, J. Phys. A **36**, 12305 (2003).

[30] See for example: X.-Z. Yuan and K.-D. Zhu, Europhys. Lett. **69**, 868 (2005); X.S. Ma, A.M. Wang, X.D. Yang and H. You, J. Phys. A **38**, 2761 (2005); X.-Z. Yuan, K.-D. Zhu, Eur. Phys. J. D **33**, 129 (2005); X.S. Ma, A.M. Wang, X.D. Yang and H. You, J. Phys. A **38**, 2761 (2005); M. Lucamarini, S. Paganelli, and S. Mancini, Phys. Rev. A **69**, 062308 (2004); S. Paganelli, F. de Pasquale and S.M. Giampaolo, Phys. Rev. A **66**, 052317 (2002).

[31] J. Wilkie and P. Brumer, Phys. Rev. A **55**, 43 (1997).

[32] T. Prosen, Ann. Phys. **235**, 115 (1994); M. Feingold and A. Peres, Phys. Rev. A **34**, 591 (1986); P. Pechukas, Phys. Rev. Lett. **51**, 943 (1983).

[33] R. Alicki, Open Systems & Information Dynamics **11**, 53 (2004).

[34] C.M Dawson, A.P. Hines, R.H. McKenzie, and G.J. Milburn, Phys. Rev. A **71**, 052321 (2005).

[35] A.S. Sanz Ortiz, Y. Elran, P. Brumer, J. Wilkie, and M. Çetinbaş, manuscript in preparation.

[36] J. Lages, V.V. Dobrovitski, M.I. Katsnelson, H.A. De Raedt and B.N. Harmon, Phys. Rev. E **72**, 026225 (2005).

[37] R. Blume-Kohout and W.H. Zurek, Phys. Rev. A **68**, 032104 (2003).

[38] Ph. Jacquod, Phys. Rev. Lett. **92**, 150403 (2004).

[39] A.G. Redfield, IBM J. Res. Dev. **1**, 19 (1957); A.G. Redfield, Adv. Magn. Reson. **1**, 1 (1965).

[40] P. Gaspard and M. Nagaoka, J. Chem. Phys. **111**, 5668 (1999); A. Suárez, R. Silbey and I. Oppenheim, J. Chem. Phys. **97**, 5101 (1992); V. Romero-Rochin and I. Oppenheim, J. Stat. Phys. **53**, 307 (1988); Physica A **155**, 52 (1989); V. Romero-Rochin, A. Orsky and I. Oppenheim, Physica A **156**, 244 (1989).

[41] R.D. Coalson and D.G. Evans, Chem. Phys. **296**, 117 (2004).

[42] A.A. Neufeld, J. Chem. Phys. **119**, 2488 (2003).

[43] E. Geva, E. Rosenman and D. Tannor, J. Chem. Phys. **113**, 1380 (2000); V. Romero-Rochin and I. Oppenheim, Physica **155**, 52 (1989).

[44] A. Bulgac A, G.D. Dang and D. Kusnezov, Phys. Rev. **58**, 196 (1998).

[45] F. Intravaia, S. Maniscalco and A. Messina, Phy. Rev. A **67**, 042108 (2003).

[46] J.B. Gong and P. Brumer, Phys. Rev. Lett. **90**, 050402 (2003); J.B. Gong and P. Brumer, J. Mod. Opt. **50**, 2411 (2003).

[47] J. Wilkie, Phys. Rev. E **62**, 8808 (2000).

[48] J. Wilkie, J. Chem. Phys. **114**, 7736 (2001).

[49] J. Wilkie, J. Chem. Phys. **115**, 10335 (2001).

[50] J. Wilkie, ArXiv:quant-ph/0306087.

[51] J. Wilkie and M. Çetinbaş, ArXiv:quant-ph/0306089.

[52] S. Nakajima, Prog. Theor. Phys. **20**, 948 (1958); R. Zwanzig, J. Chem. Phys. **33**, 1338 (1960); R. Zwanzig, in *Lectures in Theoretical Physics*, Vol. 3 (Interscience, New York, 1961).

[53] K. Kraus, Ann. Phys. (N.Y.), **64**, 311 (1971); K. Kraus, *States, Effects and Operations: Fundamental Notions of Quantum Theory*, (Springer-Verlag, Berlin,1983).

[54] D. A. Lidar, Z. Bihary and K. B. Whaley, Chem. Phys. **268**, 35 (2001).

[55] D. Deutsch, Proc. R. Soc. Lond. A **425**, 73 (1989); A. Barenco, Proc. R. Soc. Lond. A **449**, 676 (1995); D. P. DiVincenzo, Phys. Rev. A **51**, 1015 (1995).

[56] S. Loyd, Phys. Rev. Lett. **75**, 346 (1995); D. Deutsch, A. Barenco and A. Ekert, Proc. R. Soc. Lond. A **449**, 669 (1995).

[57] A. Barenco, Ch. H. Bennet, R. Cleve, D.P. DiVincenzo, N. Margolus, P. Shor, T. Sleator, J. A. Smolin and H. Weinfurter, Phys. Rev. A **52**, 3457 (1995).

[58] L. Shor, in *Proceedings of the 35th Annual Symposium on Foundations of Computer Science*, p. 124, (1994); also in arXiv:quant-ph/9508027v2.

[59] L.K. Grover, in *Proceedings of the 28th Annual ACM Symposium on Theory of Computing*, p. 212, (STOC 1996); L.K. Grover, Phys. Rev. Lett. **79**, 328 (1997); L.K. Grover, American Journal of Physics **69**, 769, (2001).

[60] N. Gisin, G. Ribordy, W. Tittel, and H. Zbinden, Rev. Mod. Phys. **74**, 145 (2002).

[61] A. Aspuru-Guzik, A. D. Dutoi, P.J. Love and M. Head-Gordon, Science **309**, 1704, (2005).

[62] See for example: J.L. Cirac and P. Zoller, Phys. Rev. Lett. **74**, 4091 (1995); J. Chiaverini, J. Britton, D. Leibfried, E. Knill, M.D. Barrett, R.B. Blakestad, W.M. Itano, J.D. Jost, C. Langer, R. Ozeri, T. Schaetz, and D. J. Wineland, Science **308**, 997 (2005).

[63] See for example: D.G. Cory, M.D. Price, and T.F. Havel, Physica D, **120**, 82 (1998); C. Ramanathan, N. Boulant, Z. Chen, D.G. Cory, I. Chuang, and M. Steffen, Quantum Information Processing, **3**, 15 (2004).

[64] A. Steane, Rep. Prog. Phys. **61**, 117 (1998).

[65] B.E. Kane, Nature (London) **393**, 133 (1998); B.E. Kane, Fortschr. Phys. **48**, 1023 (2000).

[66] W. Harneit, Phys. Rev. A **65**, 032322 (2002).

[67] See for example: D. Loss and D.P. DiVincenzo, Phys. Rev. A **57**, 120 (1998); İmamoğlu, D.D. Awschalom, G. Burkard, D.P. DiVincenzo, D. Loss, M. Sherwin, and A. Small, Phys. Rev. Lett. **83**, 4204 (1999).

[68] Y. Makhlin, G. Schön, and A. Shnirman, Rev. Mod. Phys., **73**, 357 (2001) and references therein.

[69] J. Q. You, J. S. Tsai and F. Nori, Phys. Rev. Lett. **89**, 197902 (2002).

[70] see for example: D.V. Averin, Solid State Commun. **105** , 659 (1998); Y. Makhlin, G. Schön, and A. Shnirman, Nature (London) **398**, 305 (1999); D.V. Averin, Nature (London) **398**, 748 (1999); Y. Nakamura, Y.V. Pashkin, and J.S. Tsai, Nature (London) **398**, 786 (1999).

[71] see for example: J.E. Mooij, T.P. Orlando, L. Levitov, L. Tian, C.H. van der Wal, and S. Loyd, Science **285**, 1036 (1999); C.H. van der Wal, A.C.J. ter Haar, F.K Wilhelm, R.N Schouten, C.J.P.M. Harmans, T.P. Orlando, S. Loyd, and J.E. Mooij, Science **290**, 773 (2000); J.R. Friedman, V. Patel, W. Chen, S.K. Tolpygo, and J.E. Lukens, Nature (London) **406**, 43 (2000); G. Blatter, Nature (London) **406**, 25 (2000); L.B. Ioffe, V.B. Geshkenbein, M.V. Feigel'man, A.L. Fauchére, and G. Blatter, Nature (London) **398**, 679 (1999).

[72] B. Georgeot and D.L. Shepelyansky, Phys. Rev. E **62**, 3504 (2000).

[73] B. Georgeot and D.L. Shepelyansky, Phys. Rev. E **62**, 6366 (2000).

[74] G. Benenti, G. Casati, and D.L. Shepelyansky, Eur. Phys. J. D **17**, 265 (2001).

[75] C.M. Monasterio, G. Benenti, G.G. Carlo, and G. Casati, Phys. Rev. A **71**, 062324 (2005).

[76] T. Prosen, and M. Znidaric, J. Phys. A **34**, L681 (2001).

[77] K.M. Frahm, R. Fleckinger, and D.L. Shepelyansky Eur. Phys. J. D **29**, 139 (2004).

[78] T. Gorin, T. Prosen, T. H. Seligman, and M. Žnidarič, Phys. Rep. **435**, 33 (2006).

[79] K.R. Brown, A.W. Harrow and I.L. Chuang, Phys. Rev. A **70**, 052318 (2004).

[80] S.R. De Groot and L.G. Suttorp, *Foundations of Electrodynamics*, (North-Holland, Amsterdam, 1972).

[81] M.V. Berry, Proc. R. Soc. London Ser. A **423**, 219 (1989); A. O. Bolivar, *Quantum-classical correspondence*, (Springer, Berlin, New York, 2004).

[82] W. Magnus, Commun. Pure Appl. Math. **7**, 649 (1954).

[83] M. Thorwart and P. Hänggi, Phys. Rev. A **65**, 012309 (2001).

[84] A. Mizel and D.A Lidar, Phys. Rev. Lett. **92**, 077903 (2004).

[85] R.B. Lehoncq, D.C. Sorensen, and C. Yang, *ARPACK Users' Guide: Solution of Large-Scale Eigenvalue Problems with Implicitly Restarted Arnoldi Methods*, (SIAM, Philadelphia, 1998).

[86] E. Hairer, S.P. Norsett, and G. Wanner, *Solving Ordinary Differential Equations I. Nonstiff Problems, 2nd Ed., Springer Series in Computational Mathematics, Vol. 8*, (Springer-Verlag, Berlin; New York, 1993).

[87] D. Loss and D.P. DiVincenzo, Phys. Rev. A **57**, 120 (1998).

[88] X.-Z. Yuan, K.D. Zhu, and H.S. Goan, Enr. Phys. J. D **46**, 375 (2008); F.F. Olsen, A. Olaya-Castro, and N.F. Johnson, J. Phys. Conf. Ser. **84**, 012006 (2007).

[89] A. Peres, Phys. Rev. A **30**, 1610 (1984).

[90] see for example: J. Emerson, Y.S. Weinstein, S. Lloyd and D.G. Cory, Phys. Rev. Lett. **89**, 284102 (2002) and references therein.

[91] Y.C. Cheng and R.J. Silbey, J. Phys. Chem. B **109**, 21399 (2005).

[92] see for example: M. Koashi and A. Winter, Phys. Rev. A **69**, 022309 (2004); T. J. Osborne and F. Verstraete, Phys. Rev. Lett. **96**, 220503 (2006).

[93] see for example: S. Montangero, G. Benenti, and R. Fazio, Phys. Rev. Lett. **91**, 187901 (2003); X. Wang, S. Ghose, B.C. Sanders and B. Hu, Phys. Rev. E **70**, 016217 (2004); C. Mejía-Monasterio, G. Benenti, G. G. Carlo, and G Casati, Phys. Rev. A **71**, 062324 (2005); J. N. Bandyopadhyay and A. Lakshminarayan, Phys. Rev. Lett. **89**, 060402 (2002).

[94] see for example: L. F. Santos, G. Rigolin and C.O. Escobar, Phys. Rev. A **69** 042304 (2004).

[95] F Haake, M Ku and R Scharf, Z. fur Physik B **65**, 381 (1987).

[96] W. Wang and B. Li, Phys. Rev. E **66**, 056208 (2002); Ph. Jacquod, P.G. Silvestrov, and C.W.J. Beenakker, Phys. Rev. E **64**, 055203 (2001); R.A. Jalabert and H. M. Pastawski, Phys. Rev. Lett. **86**, 2490 (2001).